Experimental Tests of QCD: Deep inelastic scattering, e^+e^- annihilation and hard hadron-hadron scattering

T. Hansl–Kozanecka *
Massachusetts Institute of Technology
Cambridge, Massachusetts 02139

Lectures given at the SLAC Summer Institute
August 5-16, 1991, Stanford, California

*Supported by the Department of Energy, contract DE-AC02-76ER03069 and by CNRS, France, as visitor of LPNHE at University Paris 6

1 Introduction

In this set of lectures we will examine the phenomenological aspects of QCD which are relevant for lepton-hadron, electron-positron and hadron-hadron collisions. In the past two decades the Standard Model has reached a certain maturity, on both the experimental and theoretical side. The Standard Model has two essential parts: the one pillar on which it rests is the electroweak theory of leptons and quarks with the photon and weak bosons as force field quanta; the other pillar is Quantum Chromodynamics (QCD), where the building blocks are quarks as matter particles and gluons as force field quanta.

The picture underlying the Standard Model and specifically QCD is the following. Quarks are the fundamental constituents of the strongly interacting particles. They have much in common with the leptons, being spin-1/2 particles that appear pointlike at the current limits of resolution of $\sim 1 \times 10^{-16}$ cm. Quarks exist in several flavours, grouped into three families or weak-isospin doublets. Whereas flavours play a specific part in weak interactions, they appear to have no role within the strong interactions: the strong coupling constant is flavour independent. Quarks also carry fractional electric charge, $\pm\, \frac{1}{3}e$ or $\pm\, \frac{2}{3}e$ and weak charge $v^2 + a^2$. The characteristics of quarks (spin, flavour, baryon number, electric charge) are directly indicated by the experimental observations that originally motivated the quark model.

Quarks have still another property known as colour, which is of central importance for the strong interactions. Colour distinguishes quarks from leptons and plays the role of a strong-interaction charge. Experiment decisively favours the colour triplet hypothesis. The three quark colours, traditionally called Red, Blue, Green, are the basis of the colour symmetry group $SU(3)_C$. The interaction between all coloured objects is mediated by an $SU(3)_C$ octet of vector gluons, where the coloured objects are the quarks and the gluons themselves.

The fundamental interaction vertices are quark-gluon couplings and self couplings of the colour charged gluons. The quark-gluon vertex (Fig. 1a) has a QED analogue in the quark-gamma vertex. The remaining two vertices (Fig. 1b) reflect the fact that gluons carry colour charge themselves. These vertices have no analogue in QED and arise on account of the non-abelian character of the gauge group. Vertices of the type shown in Fig. 1b occur also for weak interactions which are mediated by the weak gauge bosons $W^{\pm}$, Z° . There the theory is complicated by the fact that the weak bosons acquire masses. Contrary, the field quanta of QCD are *massless* gluons.

Complications in QCD arise for a different reason. As strong interactions are *strong*, their coupling α_s is large, and the power expressions for measurable quantities derived with pertubative techniques familiar from QED converge only slowly, if at all. To confront theoretical predictions with experimental data it is therefore necessary to carry the theoretical calculations beyond leading order. Given the larger number of vertices this becomes quickly a formidable task. Calculations

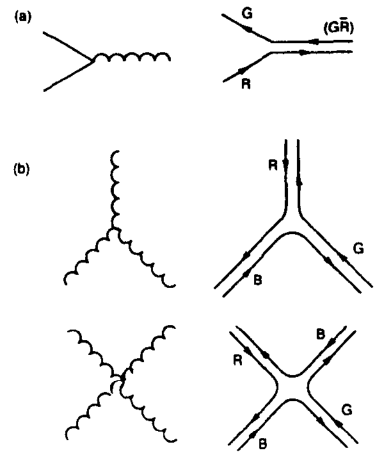

Figure 1: Fundamental interaction vertices in QCD and the corresponding colour flow: a) Quark-gluon coupling, b) Gluon-self couplings.

exist (mostly) to second order in α_s. The error due to the missing higher orders has to be carefully estimated when interpreting experimental results.

1.1 The Running Coupling Constant

With experiments being performed at increasingly higher energies, we have become accustomed to the fact that 'constants' of a theory are not constant in the strict sense but evolve with the characteristic energy Q of the process. Observables such as scattering amplitudes may be sensitive to higher order corrections. The modifications to lowest order contributions are in general sensitive to the kinematical variables. A convenient way of representing these modifications is to introduce an effective coupling strength, a so-called 'running coupling constant'.

The coupling strength α in QED, for example, evolves from its low energy Thomson scattering value of 1/137 to a value of 1/128.8 at the energy of the Z°. The photon propagator is depicted schematically in Fig. 2. There e_0 is the bare coupling, not measurable by the experimentalist. In the large Q^2 limit the sum of the terms in Fig. 2 results in [1]

$$e^2(Q^2) = e_0^2 \frac{1}{1 - \frac{\alpha_0}{3\pi} \ln \frac{Q^2}{M^2}}, \qquad \alpha_0 = \frac{e_0^2}{4\pi}, \tag{1}$$

where the ultraviolet cut-off M^2 replaces ∞ as upper limit of integration. To eliminate the explicit dependence on e_0, we reparametrize ('renormalize') $e^2(Q^2)$, or equivalently $\alpha = e^2/4\pi$, in terms of the experimentally measurable $\alpha(\mu^2)$, that is α as measured in an experiment with $Q^2 = \mu^2$,

$$\frac{1}{\alpha(Q^2)} - \frac{1}{\alpha(\mu^2)} = -\frac{1}{3\pi} \ln \frac{Q^2}{\mu^2}. \tag{2}$$

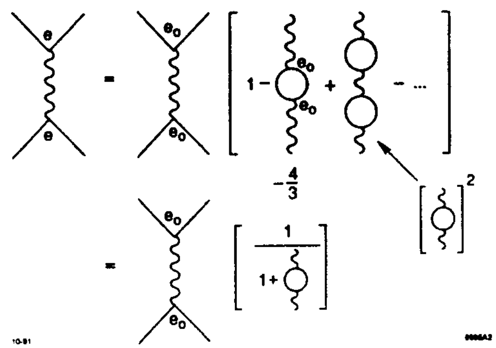

Figure 2: Running coupling constant in QED.

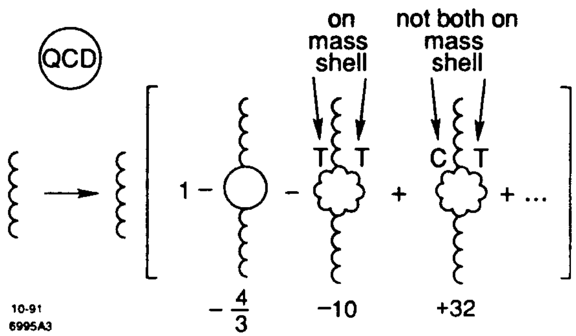

Figure 3: Running coupling constant in QCD.

A typical choice of the reference scale μ could be the mass of the electron. As Q^2 increases, α becomes stronger or equivalently the photon 'sees' more and more of the charge e_0.

The Q^2 behaviour of the QCD coupling $\alpha_s(Q^2)$ turns out to be very different. This is due to extra terms that arise from the gluon self-coupling as shown in Fig. 3. It can be shown that these QCD diagrams yield the following coefficient of $\ln(Q^2/\mu^2)$ (see *e.g.*, [2])

$$\frac{1}{2}\frac{\alpha_s(\mu^2)}{4\pi}\left(-\frac{4}{3}n_f + 22\right), \qquad n_f = \text{ number of active flavours,} \tag{3}$$

in contrast to the QED coefficient in (2)

$$\frac{\alpha(\mu^2)}{4\pi}\left(-\frac{4}{3}\right). \tag{4}$$

In (3) there is one loop for each quark flavour in contrast to just the e^+e^- loop in (4) [1]. The sign of the third loop is positive and sufficiently large to reverse the overall sign of $\ln(Q^2/\mu^2)$. This is related to the fact that there are eight gluons but only three colours of quarks.

The QCD 'running coupling constant' is then

$$\frac{1}{\alpha_s(Q^2)} - \frac{1}{\alpha_s(\mu^2)} = \frac{1}{4\pi}\left(11 - \frac{2}{3}n_f\right)\ln\frac{Q^2}{\mu^2} = b\ln\frac{Q^2}{\mu^2} \tag{5}$$
$$\text{with} \quad b = \frac{1}{4\pi}\left(11 - \frac{2}{3}n_f\right).$$

α_s decreases with increasing Q^2 and therefore becomes small for short distance interactions; QCD is 'asymptotically free'. Perturbative QCD tells us how the coupling constant varies with the scale, not the absolute value itself. The latter has to be obtained from experiment. Thus we can choose as the fundamental parameter of the theory the value of the coupling constant at a convenient reference scale which is large enough to be in the perturbative domain, $\mu = M_Z$ for example.

Including next to leading order yields [4]

$$\frac{1}{\alpha_s(Q^2)} - \frac{1}{\alpha_s(\mu^2)} + b'\ln\left(\frac{\alpha_s(Q^2)}{1 + b'\alpha_s(Q^2)}\right) - b'\ln\left(\frac{\alpha_s(\mu^2)}{1 + b'\alpha_s(\mu^2)}\right) = b\ln\frac{Q^2}{\mu^2}$$
$$\text{with} \quad b' = \frac{153 - 19n_f}{2\pi(33 - 2n_f)}. \tag{6}$$

This is now an implict equation for $\alpha_s(Q^2)$ as function of $\ln(Q^2/\mu^2)$ and $\alpha_s(\mu^2)$. Given the values for these parameters $\alpha_s(Q^2)$ can be determined numerically.

Physical observables X must be independent of the choice of μ. This requirement can be formulated as follows: the dependence of the observable $X(Q^2/\mu^2, \alpha_s)$ on μ must be cancelled by the μ-dependence of the coupling α_s,

$$\frac{dX}{d\ln\mu^2} = \left.\frac{\partial X}{\partial\ln\mu^2}\right|_{\alpha_s} + \frac{\partial\alpha_s}{\partial\ln\mu^2}\frac{\partial X}{\partial\alpha_s} = 0$$

or

$$\left(\left.\frac{\partial}{\partial\ln\mu^2}\right|_{\alpha_s} + \beta(\alpha_s)\frac{\partial}{\partial\alpha_s}\right)X = 0. \tag{7}$$

Here the β-function has been introduced,

$$\frac{\partial\alpha_s}{\partial\ln\mu^2} = \beta(\alpha_s). \tag{8}$$

Equation (7) is the 'renormalization group equation'. The perturbative expansion of the β-function is

$$\beta(\alpha_s) = -b\alpha_s^2\left(1 + b'\alpha_s + \mathcal{O}(\alpha_s^2)\right) \tag{9}$$

[1] The factor 1/2 is due to a mismatch in the definition of α and α_s.

sometimes also written as

$$\beta(\alpha_s) = -\alpha_s\left(\beta_0\frac{\alpha_s}{4\pi} + \beta_1(\frac{\alpha_s}{4\pi})^2 + \mathcal{O}((\frac{\alpha_s}{4\pi})^3)\right) \tag{10}$$
$$\text{with} \quad \beta_0 = 11 - \frac{2}{3}n_f, \qquad \beta_1 = 102 - \frac{38}{3}n_f.$$

Historically the dimensional parameter Λ has been introduced for specifying the strength of the strong interaction. Λ is the limiting Q scale at which the effective coupling will become large,

$$b\ln\frac{Q^2}{\Lambda^2} = \frac{1}{\alpha_s(Q^2)}. \tag{11}$$

The next-to-leading expression (6) becomes

$$b\ln\frac{Q^2}{\Lambda^2} = \frac{1}{\alpha_s(Q^2)} + b'\ln\left(\frac{b'\alpha_s(Q^2)\oplus}{1+b'\alpha_s(Q^2)}\right). \tag{12}$$

This equation (12) has been 'semi-universally' adopted as the definition of α_s in terms of Λ [10]. But it is not unique. Adding a constant at the right-hand-side at location $\oplus$ still gives a solution of the differential equation (8). Other approximations have been used for Λ. Since in practice it is usually α_s which is measured experimentally, it is important when comparing Λ values to check that the same equation has been used to define Λ from the coupling constant. Differences between the results obtained using different conventions can be comparable to present day measurement errors.

The use of Λ presents more traps. Λ depends on the number of active flavours. Values of Λ for different numbers of flavours are defined by imposing the continuity of α_s at the scale of $\mu = m$, where m is the mass of the heavy quark [11]. In practice it is sufficient to assume that β_0,β_1,... change discretely at $Q \sim m_Q$. To ensure the continuity of α_s, Λ must change on crossing a threshold. For $Q \geq m_b$ for example at LEP/SLC energies, we have

$$\frac{1}{\alpha_s^{(5)}(Q^2)} = \frac{b^{(5)}\ln\left(Q^2/\Lambda^{(5)2}\right)}{[1-\ldots]}.$$

For $m_c \leq Q \leq m_b$, the typical energy range for deep inelastic scattering, the coupling evolves with four active flavours and the correct form to use is

$$\frac{1}{\alpha_s^{(4)}(Q^2)} = \frac{b^{(4)}\ln\left(Q^2/\Lambda^{(5)2}\right)}{[1-\ldots]} + \text{constant}.$$

The constant is fixed by the continuity condition

$$\alpha_s^{(4)}(m_b^2) = \alpha_s^{(5)}(m_b^2).$$

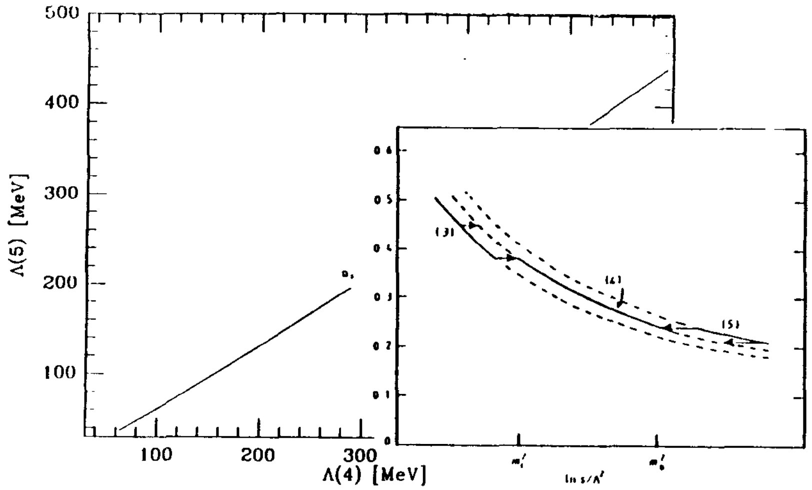

Figure 4: Comparison of $\Lambda_{\overline{MS}}$ for 4 and 5 flavours. The insert shows α_s as function of $\ln s/\Lambda^2$ and illustrates the discontinuity of $\Lambda_{\overline{MS}}$ at flavour thresholds.

Fig. 4 shows the relation between $\Lambda^{(4)}$ and $\Lambda^{(5)}$; the insert depicts the relation between Λ and α_s when crossing flavour thresholds. We mention only in passing another troubling property of Λ, namely its dependence on the renormalization scheme. Nowadays most calculations in fixed order QCD perturbation theory are performed in the 'modified minimal substraction' renormalization scheme, $\overline{MS}$, which is explained in appendix A. We always refer to this $\overline{MS}$ definition of α_s in the following sections.

Lastly, the expression of the experimentally measured coupling α_s in terms of Λ leads to asymmetric errors, an unpleasant property of any measured quantity for which errors have to be propagated. Because of these troubling properties experimentalists should be encouraged to report their QCD tests in terms of α_s rather than Λ.

1.2 Overview

Our three lectures will lead us through three different regimes in which QCD can be tested. Out of the wealth of tests that were accumulated over the years, we will have to restrict ourself to the latest results. For the high precision experiments that are performed nowadays, calculations in leading order are no longer sufficient. Going beyond leading order means that the tedious discussion of renormalization schemes can not be avoided. The aim of these lectures is to convey how QCD manifests itself. Theoretical ideas are outlined, but for precise derivations we refer the reader to Refs. [1] to [10] and references therein.

The most stringent tests of QCD can be performed in deep inelastic lepton scattering (DIS) and in e^+e^- annihilation. In deep inelastic scattering the virtual γ or W/Z is used as a probe of the nucleon structure, Fig. 5a. The exchanged γ or W/Z couples only to the quarks. Gluons are tested indirectly by measuring the momentum distributions of the quarks and the dependence of these distributions on the wavelength of the probe. Tests are complicated through the presence of other quarks in the nucleon. The size of the probed region is directly related to the wavelength of the probe which is proportional to the inverse momentum 1/Q carried by the probe. Only the incoming and outgoing lepton have to be measured, the hadronic final state has not to be analysed and the complications involved in hadronization can be avoided. Deep inelastic scattering data provide one of the precision tests of QCD and provided for many years the most precise measurement of α_s .

With the higher energies and the high statistics data available at the e^+e^- colliders, the new generation of e^+e^- annihilation experiments result in α_s measurements of comparable precision. The initially produced virtual γ or Z° decays to lepton and quark pairs, Fig. 5b. The branching ratio into quarks is a counter for the number of colours available, the detailed structure of the final state reflects the radiation of gluons as the initial quark-antiquark separate from each other. QCD tests consist in measuring the rate at which gluon radiation occurs and in measuring its angular and energy distribution. Quarks and gluons are observed 'in action', though through the 'veil' of hadronization. The typical scale for α_s is of the order of the center-of-mass energy $\sqrt{s}$.

The third regime for QCD tests are hard parton-parton collisions, e.g., hard hadron-hadron collisions, Fig. 5c. There the parton distributions probed in DIS are combined with the parton shower of radiating quarks and gluons probed in e^+e^- annihilation. The incoming partons provide broadband beams of partons with varying fractions of the momenta of their parent hadrons as measured in DIS. Gluons are the main actor: The cross sections are dominated by the gluon component, which is only indirectly measured in DIS. Predictions for hard hadron-hadron collisions have therefore in the past been less precise; experiments at hadron colliders give less precise but still important tests of QCD. The characteristic scale of the hard scattering is, for example, the transverse momentum of a jet or the mass of the produced weak boson.

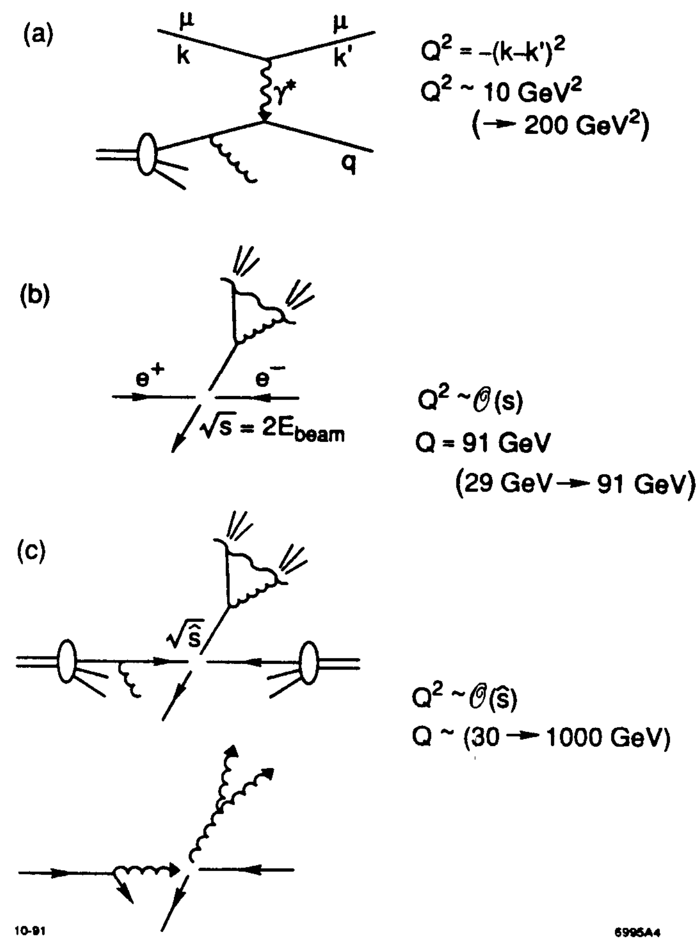

Figure 5: Three regimes for testing QCD: a) Deep inelastic scattering, b) e^+e^- annihilation, c) hard hadron-hadron scattering.

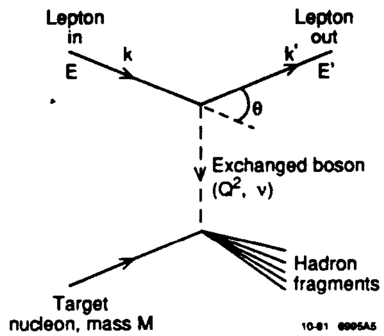

Figure 6: The lowest order diagram and the kinematical variables for deep inelastic lepton scattering.

2 Scaling Violations in Deep Inelastic Scattering

The original and still very powerful test of QCD is the breaking of Bjorken scaling in deep-inelastic lepton-hadron scattering. The analyses of structure functions provide one of the precise tests of QCD and determine the momentum distributions of partons in hadrons. The latter are the necessary input to predict cross sections in high energy hadron collisions.

2.1 The Parton Model

The 'naive' parton model has already been presented in a previous lecture [12]. Here follows a short summary. If we label the four-momenta for incoming and outgoing leptons, the target hadron and the momentum transfer by k, k', p, q = k-k' respectively (Fig. 6) then the standard deep inelastic variables are defined by

$$\begin{aligned} p^2 &= M^2 && && (13)\\ Q^2 &= -q^2 && \text{Virtuality of the probe} \\ x &= \frac{Q^2}{2p\cdot q} = \frac{Q^2}{2M(E-E')} && \text{Scaling variable} \\ y &= \frac{q\cdot p}{k\cdot p} = \frac{E-E'}{E} && \text{Relative momentum transfer.} \end{aligned}$$

The scattering is mediated by the exchange of a virtual photon (scattered lepton is μ or e) or gauge boson $W^{\pm}$ (scattered lepton is ν or $\bar{\nu}$), Fig. 7. The structure of the target as 'seen' by this probe is parametrised by the structure functions $F_i(x, Q^2)$.

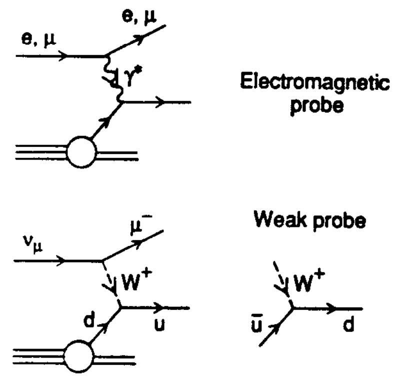

Figure 7: Deep inelastic scattering in the quark parton model.

The cross sections are for charged lepton scattering on protons

$$\frac{d^2\sigma^{em}}{dx dy} = \tag{14}$$
$$\frac{8\pi\alpha^2}{Q^4} M E \left[\frac{1+(1-y)^2}{2} 2x\, F_1^{em} + (1-y)(F_2^{em} - 2x\, F_1^{em}) - \frac{M}{2E} xy\, F_2^{em} \right]$$

and for neutrino (anti-neutrino) scattering

$$\frac{d^2\sigma^{\nu(\bar{\nu})}}{dx dy} = \tag{15}$$
$$\frac{G_F^2}{\pi} M E \left[(1 - y - \frac{M}{2E} xy)\, F_2^{\nu(\bar{\nu})} + \frac{y^2}{2} \cdot 2x\, F_1^{\nu(\bar{\nu})} +(-)\ (y - \frac{y^2}{2})\, x\, F_3^{\nu(\bar{\nu})} \right].$$

The structure functions are approximately independent of Q^2. This 'Bjorken scaling' implies that the virtual photon is scattered off *pointlike* constituents, otherwise the dimensionless functions would have to depend on Q/Q_0, introducing a length scale $1/Q_0$.

In the parton model, the structure functions can be interpreted in terms of 'parton distributions'. If q(x)dx represents the probability that a quark q carries momentum fraction between x and x+dx and the virtual photon scatters incoherently off the quark constituents then (Fig. 7)

$$\begin{aligned} F_2^{em} &= x\left[(\frac{2}{3})^2(u+\bar{u}+c+\bar{c}) + (\frac{1}{3})^2(d+\bar{d}+s+\bar{s}) \right] && \text{Probe: } \gamma^* \\ F_2^{\nu} &= 2x\,[d+s+\bar{u}+\bar{c}] && \text{Probe: } W^+ \\ xF_3^{\nu} &= 2x\,[d+s-\bar{u}-\bar{c}] \\ F_2^{\bar{\nu}} &= 2x\,[u+c+\bar{d}+\bar{s}] && \text{Probe: } W^- \\ xF_3^{\bar{\nu}} &= 2x\,[u+c-\bar{d}-\bar{s}] \\ 2xF_1 &= F_2. && && (16) \end{aligned}$$

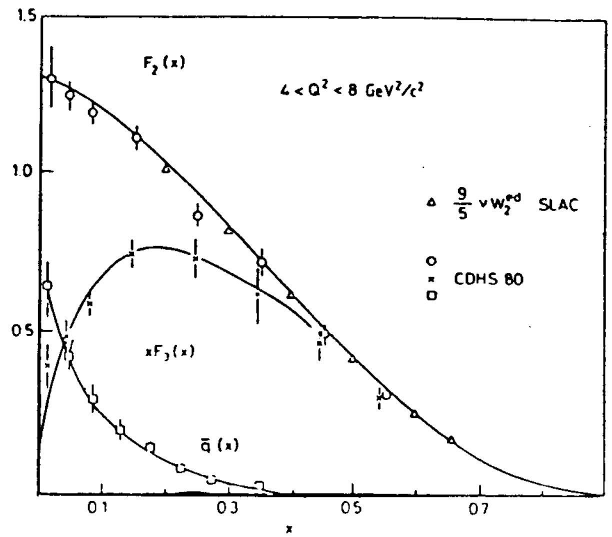

Figure 8: The structure functions $F_2^{\nu}(x)$ and $F_2^{em}(x) \times \frac{18}{5}$, and the structure function $xF_3(x)$.

The last result follows from the spin 1/2 property of the quarks. The quark distributions are weighted by their charges e_q^2 or their weak charges, respectively. Neutrino and anti-neutrino scattering distinguish between quarks and anti-quarks whereas in charged lepton scattering this distinction is not possible. The sum of ν and $\bar{\nu}$ cross sections has the same structure function dependence as the cross section for charged leptons.

Experimentally the good agreement of F_2^{ν} and F_2^{em} (scaled by the charge factor $\frac{18}{5}$) was a strong confirmation of the simple quark model, Fig. 8. The integral of the difference of the cross sections, $\sigma^{\nu} - \sigma^{\bar{\nu}} \sim xF_3$,

$$\int xF_3(x) \cdot dx = \int (q(x) - \bar{q}(x))\, dx = 3$$

measures the number of valence quarks. The experiments find consistently a value close to 3, with typical uncertainties of 10%. The sum of the cross sections $\sigma^{\nu} + \sigma^{\bar{\nu}} \sim F_2(x)$ measures the fraction of momentum carried by the quarks and anti-quarks in the proton. The value is experimentally found to be

$$\sum_{q,\bar{q}} \int_0^1 dx\, xq(x) \approx 0.45 \text{ to } 0.50 \qquad at\quad Q^2 \sim 10\ GeV^2.$$

This means that the quarks carry only about 50% of the proton's momentum, a fraction that is nearly constant for $q^2 \geq 10\ GeV^2$ [13]. The remaining fraction of momentum is attributed to gluon constituents. This is a first indirect measurement of gluons. Deep inelastic scattering experiments are normally not designed to measure details of the final hadronic state and are therefore not suited to show direct evidence of gluons in their manifestation as jets [14].

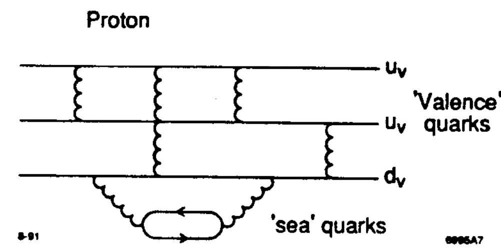

Figure 9: The quark picture of the proton.

From the data, the following picture emerges (Fig. 9): The proton consists of three *valence* quarks (u u d) which carry electric charge and baryon quantum numbers of the proton, and an infinite *sea* of light $q\bar{q}$ pairs. When probed at scale Q, the sea contains all quark flavours with $m_q \ll Q$,

$$\begin{aligned} u(x) &= u_V(x) + u_S(x) \\ d(x) &= d_V(x) + d_S(x) \\ \bar{u}(x) &= \bar{d}(x) = u_S(x) = d_S(x) = S(x) \\ \bar{s} &\approx 0.4\bar{u} \quad (at \quad Q^2 = 5\ GeV^2)[15]. \end{aligned}$$

2.2 QCD Improved Parton Model and Scaling Violations

In the naive parton model, the structure functions scale, $F(x, Q^2) \rightarrow F(x)$. In fact, this Bjorken scaling is only approximate. This is illustrated in Fig. 10 which shows a representative sample of data from SLAC and BCDMS measurements [4]. To a good approximation the data lie on a universal curve, but the curve shrinks with increasing Q^2. This becomes even more evident in Fig. 11. Scaling violations are predicted by QCD and are logarithmic in Q^2. The one-gluon corrections to the lowest order quark scattering are shown in Fig. 12. The quarks can radiate gluons before or after being struck by the virtual photon γ^*.

The modifications due to QCD can be described by Q^2 dependent quark distributions

$$F_2(x, Q^2) = \sum_q e_q^2\, x\, q(x, Q^2) \tag{17}$$

which are predicted in $\mathcal{O}(\alpha_s)$ to be

$$q(x, Q^2) = q(x) + \frac{\alpha_s(\mu^2)}{2\pi} \int_x^1 \frac{dy}{y} q(y) \left\{ P(\frac{x}{y}) \ln \frac{Q^2}{k^2} + f(\frac{x}{y}) \right\} + \ldots$$

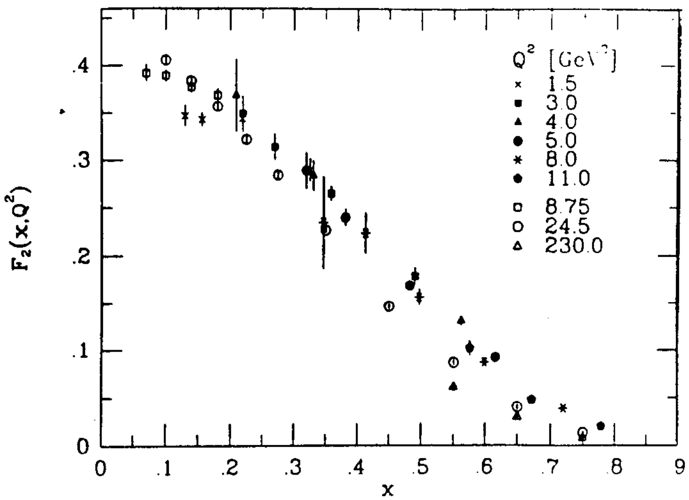

Figure 10: The $F_2(x)$ structure function measured by the SLAC and BCDMS experiments.

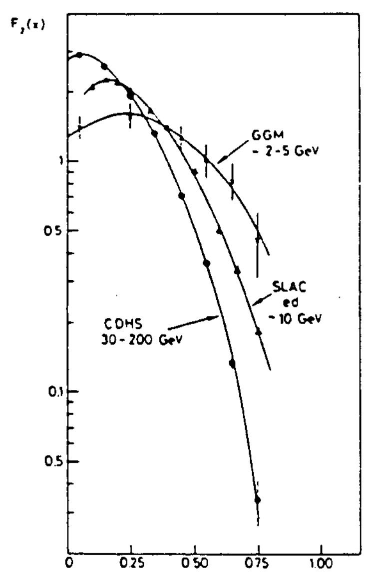

Figure 11: The $F_2(x)$ structure function measured by the CDHS, SLAC and Gargamelle experiments.

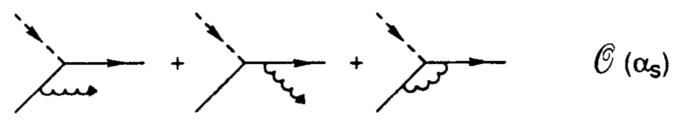

Figure 12: Lowest order QCD correction to deep inelastic scattering.

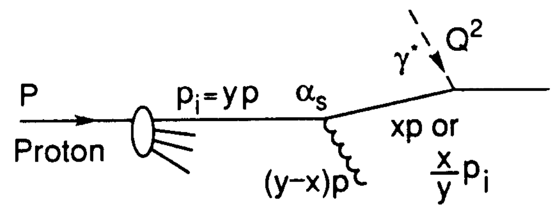

Figure 13: Kinematical variables for one gluon radiation.

The kinematical variables are explained in Fig. 13. The correction is proportional to α_s; only the quarks with momentum fraction $y > x$ contribute. P and f are calculable functions and k is a cutoff that is introduced to control collinear divergence (gluon emitted parallel to incoming quark). Similar as for the bare coupling constant α_s, $q(x)$ is a bare distribution, not accessible to the experiment. Similar to $\alpha_s(Q^2)$ there is no absolute prediction of the renormalized distribution $q(x,Q^2)$. What QCD does predict, however, is the evolution with Q^2,

$$\begin{aligned}\frac{dq(x,Q^2)}{d\ln Q^2} &= \frac{\alpha_s(\mu^2)}{2\pi}\int_x^1 \frac{dy}{y}\, q(y,Q^2)\, P(\frac{x}{y}) \\ &= \frac{\alpha_s(\mu^2)}{2\pi}\int_x^1 \frac{dz}{z}\, q(\frac{x}{z},Q^2)\, P(z). \qquad (18)\end{aligned}$$

This equation is the analogue of the β-function equation which describes the variation of $\alpha_s(Q^2)$ with $\ln Q^2$. P(z) can be interpreted as the probability of finding a quark with a fraction z of the parent quarks momentum. Note that the strength of the scaling violations depends on α_s, and hence provides a measurement of α_s.

Eq. (18) is a special case of the Altarelli-Parisi (AP) equation, which is in general a matrix equation. The gluon constituent in the target can contribute to deep inelastic scattering as well via $\gamma^* g \to \bar{q}q$, Fig. 14. There are therefore four different functions $P_{ij}(z)$, the AP kernels, for finding a parton of type i in a parton of type j with a fraction z of the longitudinal momentum of the parent parton.

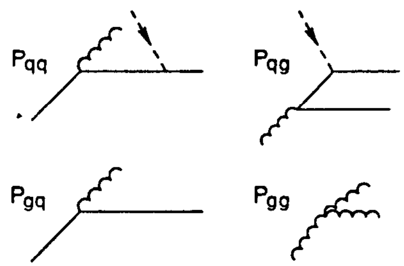

Figure 14: $\mathcal{O}(\alpha_s)$ gluon-initiated hard scattering contributions to deep inelastic scattering: Diagrams corresponding to the Altarelli-Parisi kernels.

The general AP equation is

$$\begin{aligned}\frac{\partial q_i(x,Q^2)}{\partial \ln Q^2} &= \frac{\alpha_s(\mu^2)}{2\pi}\int_x^1 \frac{dz}{z}\left\{ P_{qq}(z)\, q_i(\frac{x}{z},Q^2) + P_{qg}(z)\, G(\frac{x}{z},Q^2)\right\} \\ \frac{\partial G(x,Q^2)}{\partial \ln Q^2} &= \frac{\alpha_s(\mu^2)}{2\pi}\int_x^1 \frac{dz}{z}\left\{ P_{gq}(z)\sum_j q_j(\frac{x}{z},Q^2) + P_{gg}(z)\, G(\frac{x}{z},Q^2)\right\}. \quad (19)\end{aligned}$$

The AP kernels are in general a perturbative expansion in the running coupling; the lowest order terms [16] and the first correction [17] have been calculated. This amounts to

$$\begin{aligned} P_{qq}(z,\alpha_s) &= P^{[0]}_{qq}(z) + \alpha_s(\mu^2)P^{[1]}_{qq}(z) + \ldots, \\ \text{and}\quad P^{[1]}(z,\frac{Q^2}{\mu^2}) &= P^{[1]}(z) + \frac{\beta_0}{4\pi}P^{[0]}(z)\ln\frac{\mu^2}{Q^2}\end{aligned}$$

and the replacement of eqn. (17) by

$$\frac{1}{x}F_2(x,Q^2) = \sum_q e_q^2 \int_x^1 \frac{dy}{y}\, q(\frac{x}{y},Q^2)\left[\delta(1-y) + \frac{\alpha_s}{2\pi}f(y) + \ldots\right].$$

How much of the finite $\mathcal{O}(\alpha_s)$ correction is included in q (and G) and how much in F_2 is a matter of convention ('factorization scheme', related to a 'factorization scale'). For more details see *e.g.*, Ref. [18].

2.3 Measurement of α_s

Fits to the data are performed by parametrizing the parton distributions at a reference value Q_0, *e.g.*,

$$q(x,Q_0^2) = A_q\, x^{a_q}(1-x)^{b_q}(1-c_q x).$$

The AP equations are then solved numerically to get $q_i(x,Q^2), G(x,Q^2)$ and hence $F(x,Q^2)$. The best values of the parameters $(A_u, a_u, \ldots, b_G, c_G, \alpha_s)$ are determined in a global fit [2]. There are two major complications in this analysis.

[2] The available sets of parton density functions and corresponding α_s values are summarized in Ref. [19].

- The value of α_s and the gluon density function G are correlated. From the AP equation it follows that, for example, an increase in the value of α_s can be compensated by a decrease of the gluon function G. The problem is less severe at large x, where the gluon contribution is small.
- At small Q^2, forces between quarks are no longer negligible. The structure functions have 'higher twist' power corrections [20], which are due to *e.g.*, interactions with diquarks and are difficult to estimate quantitatively:

$$F(x,Q^2) = F^{LT}(x,Q^2) + \frac{F^{HT}(x,Q^2)}{Q^2} + \ldots$$

To avoid these complications the analysis must be performed at large $Q^2(1-\frac{1}{x})$, where the power-suppressed terms are negligible. Three main classes of analyses have been performed.

Nonsinglet analysis. It is useful to define combinations of structure functions that are free of the gluon function. This simplifies the solution of the AP equation. Such combinations are $q_i - q_j$ or $q_i - \bar{q}_i$, which are non-singlet (in flavour space),

$$q^{NS} = q_i - q_j \qquad \text{or} \qquad q^{NS} = q_i - \bar{q}_i.$$

Examples are

$$\begin{aligned} xF_3^{\nu N} = xF_3^{\bar{\nu}N} &= x(q-\bar{q}), \qquad \text{and} \\ F_2^{\mu p} - F_2^{\mu n} &= \frac{1}{3}x\,(u+\bar{u}-d-\bar{d}).\end{aligned}$$

Unfortunately these distributions are only well measured in regions where scaling violations are small. The differences of the cross sections vanish as $x \to 0$ where the statistical accuracy is high. Thus the results have inevitably large systematic and statistical errors.

Singlet analysis. The singlet combination

$$q^S = \bar{q}_i + q_i$$

is sensitive to α_s and the gluon distribution. Pure singlet structure functions are measured in scattering from isoscalar targets such as deuterium, carbon (C_6^{12}) or iron (Fe_{26}^{56}, approximately isoscalar). Except at large x, where the gluon contribution is negligible, there is a strong $\alpha_s \leftrightarrow$ gluon correlation.

Hydrogen. The scattering from free protons contains singlet and non-singlet parts with a different evolution for each, *e.g.*,

$$\begin{aligned}
F_2^{\mu p} &= F_2^{NS} + F_2^S + \frac{1}{6}x\,[(c+\bar{c}) - (s+\bar{s})], \\
\text{where } F_2^{NS}(H_2) &= \frac{1}{2}(F_2^p - F_2^n) = \frac{1}{6}x[u - \bar{u} + d - \bar{d}] = \frac{1}{6}x[u_V - d_V] \\
F_2^S(H_2) &= \frac{1}{2}(F_2^p + F_2^n) - \frac{1}{6}x\,[c + \bar{c} - (s+\bar{s})] = \frac{5}{18}x\sum_1^{n_f}(q_i + \bar{q}_i)
\end{aligned}$$

and the evolution of F_2^S is coupled to the gluon evolution. The evolution is treated taking both components into account and combining the deuterium and hydrogen data for F_2^p and F_2^n.

Our lecture will be restricted to the most recent analyses and mostly to the SLAC and BCDMS data. Other lectures in this Summer School cover structure functions more generally [12, 18, 21, 22].

2.4 High statistics measurements of α_s

Over the last years an imposing experimental effort has been devoted to the measurement of scaling violations in deep inelastic scattering with electron or muon, neutrino or anti-neutrino beams on hydrogen, deuterium and heavy nuclei. A new generation of high precision experiments has been completed. The existence of scaling violations is definitely established at Q^2 values large enough to support the prediction that their asymptotic decrease is only logarithmic.

The reanalysis [23] of the electron scattering experiments performed at SLAC between 1970 and 1985 has been very useful in resolving most of the experimental discrepancy between the data taken by the EM collaboration [24, 25] and the BCDMS collaboration [26]. A smooth extrapolation of the SLAC data (taken arbitrarily as reference) is possible after renormalization of the hydrogen (deuterium) data of BCDMS by -2% (-1%) and the EMC data by +8% [27], Fig. 15. The heuristic renormalization factors are in acceptable agreement with the quoted normalization uncertainties of 2%, 5% and 3% for SLAC, EMC and BCDMS data, respectively.

In the following the fits to the BCDMS data and the combined fit of BCDMS and SLAC data will be discussed, allowing for more and more detailed tests. The fits to the data are either non-singlet fits (without gluon function G) or singlet fits of α_s and the gluon function. Data points are fitted in the (x,Q^2) plane or the x-dependence of the logarithmic derivatives $d\ln F_2/d\ln Q^2$ is compared to QCD.

Fig. 15 shows the structure function F_2 measured in muon-hydrogen and muon-deuterium scattering. The data extend up to $x = 0.75$ and Q^2 values of $\sim 200\ GeV^2$. For the fit data points are selected applying x-dependent Q^2 cuts to suppress higher twist effects. Systematic errors are dominated by the uncertainty on the relative normalization between data taken at (three) different beam ener-

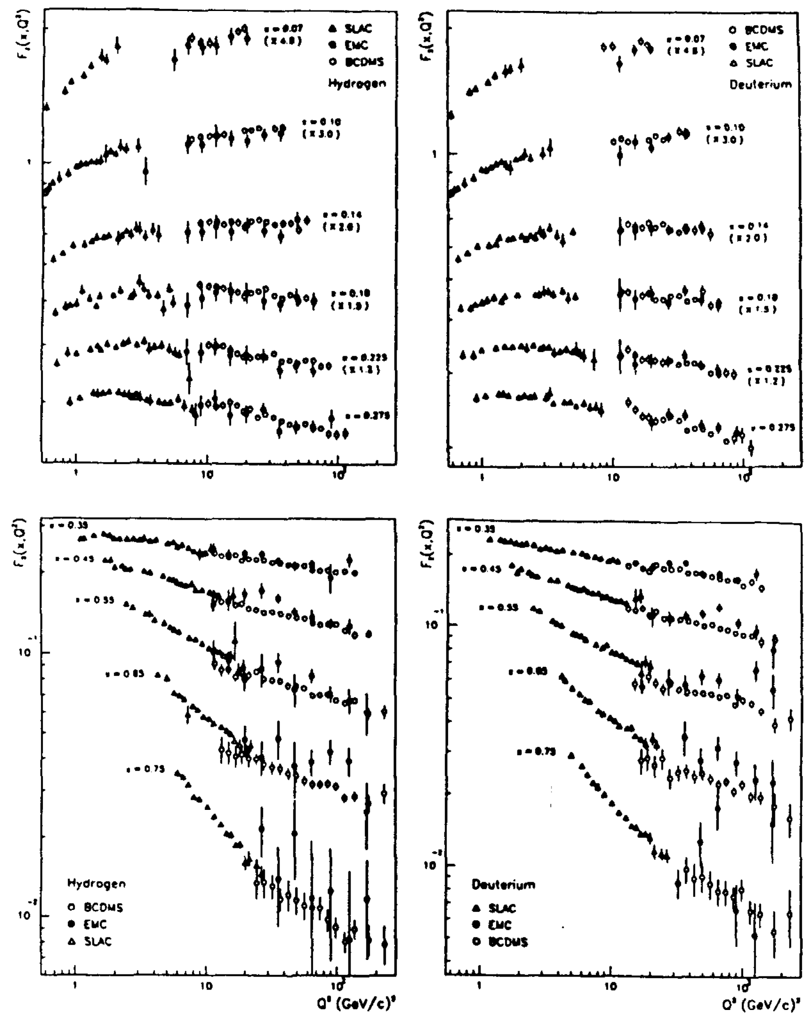

Figure 15: Comparison of the high statistics measurements of the hydrogen (left) and deuterium (right) structure functions $F_2(x,Q^2)$ from SLAC, EMC, BCDMS. The normalizations are adjusted as explained in the text [27].

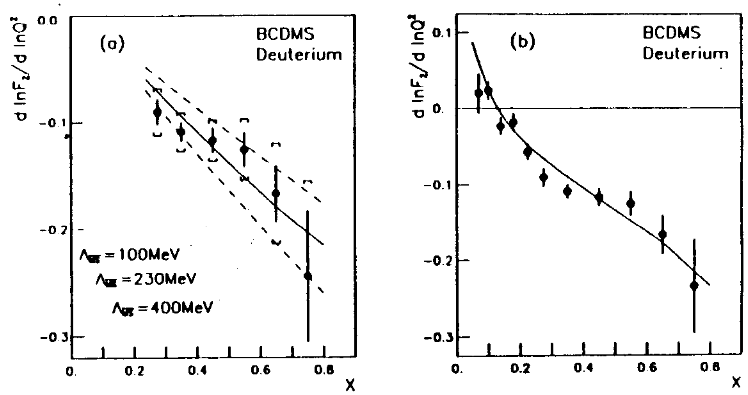

Figure 16: (a) Logarithmic derivatives of F_2, for $Q^2 > 20\ GeV^2$ and $x > 0.275$. The lines show non-singlet QCD predictions. (b) As (a) but for the full x range. The solid line shows the singlet prediction ($\Lambda_{\overline{MS}} = 250\ GeV$) [26].

gies (120, 200, 280 GeV) and are strongly correlated. The fit result is insensitive to the choice of the Q_0^2 value at which the evolution is started.

The agreement between data and QCD is best verified by comparing the x dependence (averaged over Q^2) of measured and predicted scaling violations. This is shown for deuterium data and $x > 0.275$ in Fig. 16a. In the non-singlet approximation this comparison depends on Λ as sole free parameter, whereas in a singlet analysis over the full x-range it is also sensitive to the gluon distribution. The logarithmic derivatives of F_2 are negative, consistent with a structure function that decreases in this x region with increasing Q^2. The logarithmic derivatives for the hydrogen data are shown in Fig. 17a and compared to the carbon data in Fig. 17b. The good agreement allows a combined fit resulting in a very accurate α_s measurement. The fits are summarized in Table 1.

Dependence on the gluon structure function. To perform the fits over the full x-range, assumptions have to be made on the gluon distribution at small x. Fig. 18c demonstrates that the fits are not very dependent on the exponent η of the gluon distribution that was assumed to $x\,G(x,Q_0^2) = A(\eta+1)(1-x)^\eta$ at $Q_0^2 = 5\ GeV^2$. But η is strongly dependent whether the fit is performed in lowest or next-to-leading order, see Fig. 18a. It is remarkable that the correlation between Λ and η decreases substantially when higher orders are used, Fig. 18b.

Influence of higher twist terms. The BCDMS data combined with the SLAC data cover a wide kinematical range ($0.07 < x < 0.85$, $0.5 < Q^2 < 260\ GeV^2$) and are well suited to test the influence of higher twist effects on the measurement

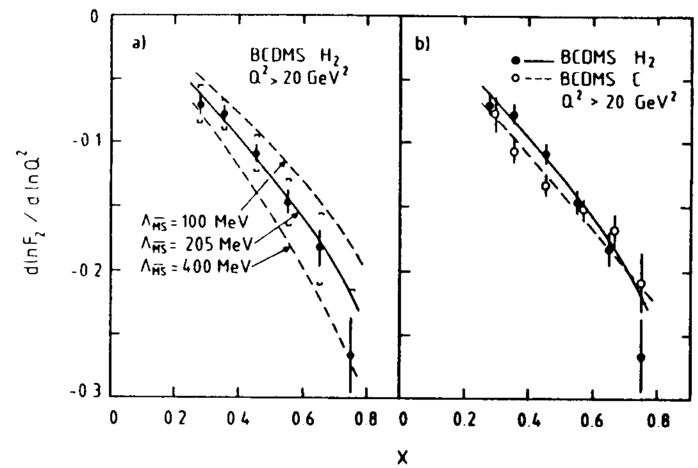

Figure 17: (a) As Fig. 16 but for hydrogen target. (b) As (a), but comparing hydrogen data to the carbon target results [26].

of α_s. The common fit [29] includes coefficients C_x (one per x-bin and target material) describing the higher twist effect

$$F_2^{HT}(x,Q^2) = F_2^{QCD}(x,Q^2)\,(1+\frac{C_x}{Q^2}).$$

The small normalization shift between BCDMS and SLAC data is -1% (0.4%) for the H_2 (D_2) targets. Fig. 19 shows the H_2 and D_2 data together with the NLO QCD fit. The effect of higher twist terms is also shown; it is small or negligible above $Q^2 \sim 4\ GeV^2$ at low x (x< 0.5) and above $Q^2 \sim 10\ GeV^2$ at higher x. The higher twist coefficients, are very similar for H_2 and D_2, Fig. 20, and they increase with x. At lower x, $x < 0.4$, they are compatible with zero but are strongly correlated with the gluon distribution; the uncertainty on this distribution accounts for the larger errors. The logarthmic derivatives of F_2 agree very well for H_2 and D_2 (Fig. 21a) which justifies the combined fit (Fig. 21b).The result is a very accurate measurement of α_s ,

$$\begin{aligned} \alpha_s(50\ GeV^2) &= 0.180 \pm 0.008(stat \oplus syst), \\ \text{or}\quad \alpha_s(M_Z^2) &= 0.113 \pm 0.003(stat \oplus syst), \end{aligned}$$

where the value at $Q^2 = M_Z^2$ is obtained from the evolution equation for α_s.

Dependence on the renormalization and factorization scale. When the data are sufficiently precise to be sensitive to next-to-leading order terms then the fact that QCD calculations can not be carried out to all orders, introduces a

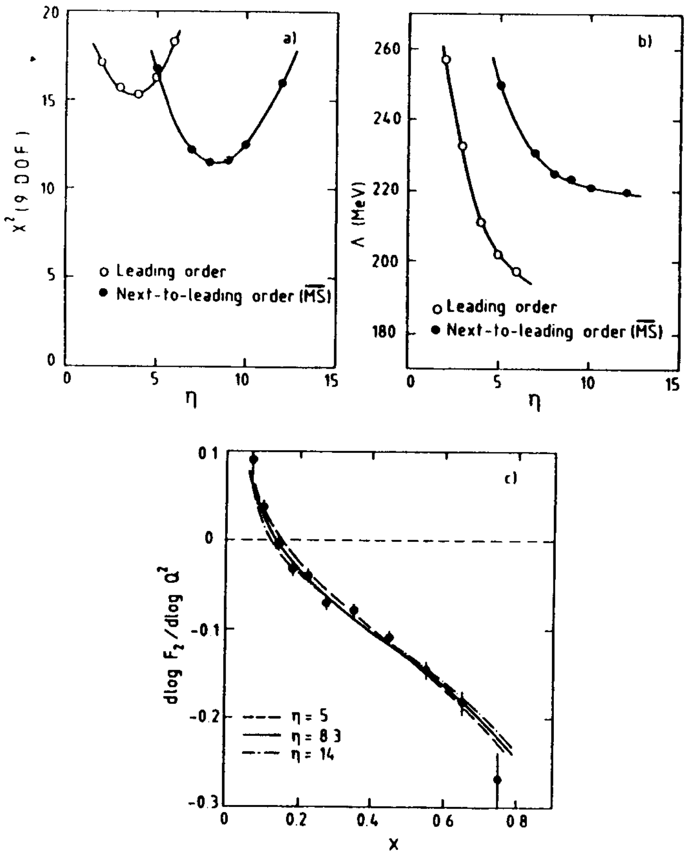

Figure 18: (a) The χ^2 from the singlet $\oplus$ nonsinglet LO and NLO fits. (b) The dependence of $\Lambda_{\overline{MS}}$ on the exponent of the gluon distribution $x\,G(x,Q_0^2) \propto (1-x)^\eta$ for LO and NLO QCD fits. (c) The logarithmic derivatives of F_2 and the NLO QCD fits for different exponents η [26].

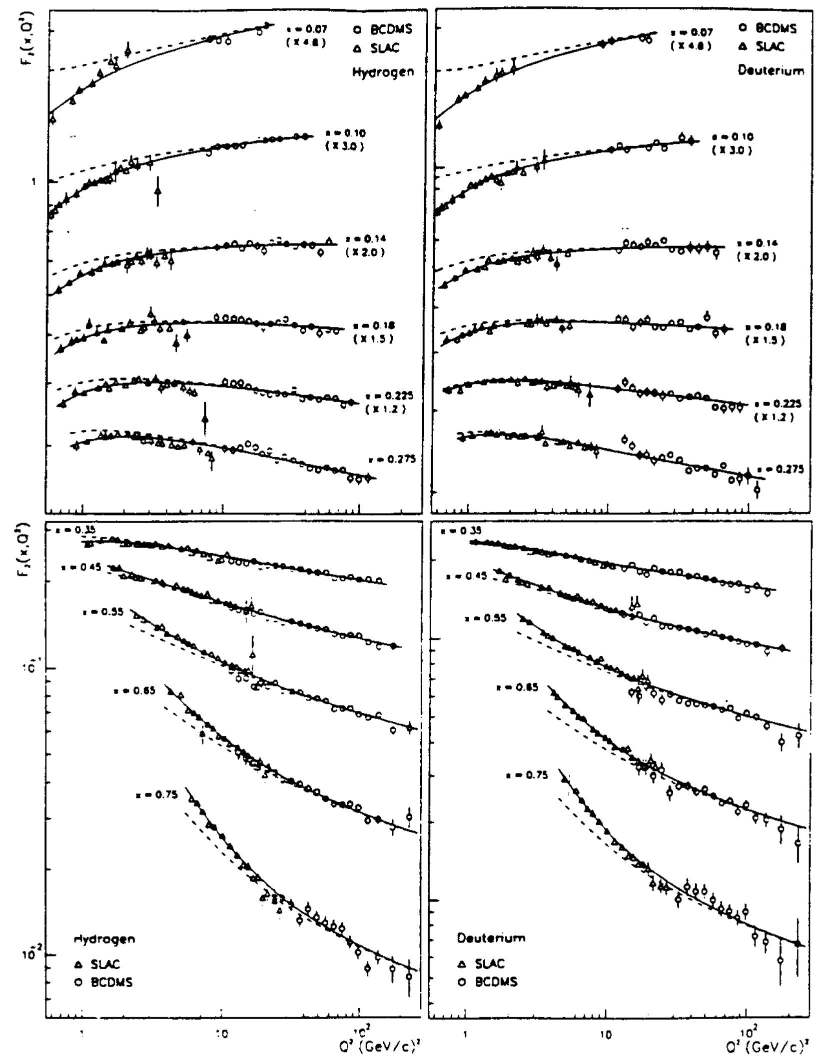

Figure 19: NLO QCD fit to SLAC and BCDMS H_2 and D_2 data. The solid line depicts the result of the fit, the dashed line visualizes the Q^2 evolution without higher twist effects [29].

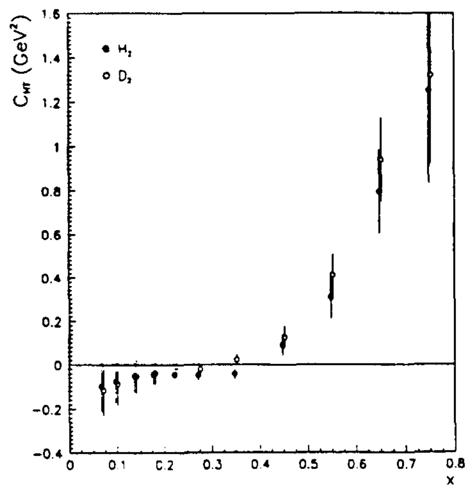

Figure 20: The higher twist coefficients C_x. Full (open) circles are for H_2 (D_2) data [29].

experiment	target	$\Lambda_{\overline{MS}}$	reference
CDHSW	$\nu, \bar{\nu}$ Fe	100^{+90}_{-60}	[31]
BCDMS	D_2	$230 \pm 40 \pm 70$	[26]
	$H_2 + C$	$220 \pm 15 \pm 50$	[26]
$F_2^p - F_2^n$	H_2, D_2	$250^{+130}_{-110} \pm 90$	[32]
SLAC+BCDMS	$H_2 + D_2$	$263 \pm 42 \pm 55$ $(theor)$	[29]
EMC (reanalysis)	H_2	$211^{+83}_{-73}{}^{+84}_{-11}$	[33]
CCFR (xF_3)	$\nu, \bar{\nu}$ Fe	$\Lambda_{\overline{MS}} \pm 40 \pm 45$	[34]
(xF_3, F_2)		$\Lambda_{\overline{MS}} \pm 20 \pm 38$	

Table 1: Selected list of recent α_s measurements in deep inelasic scattering.

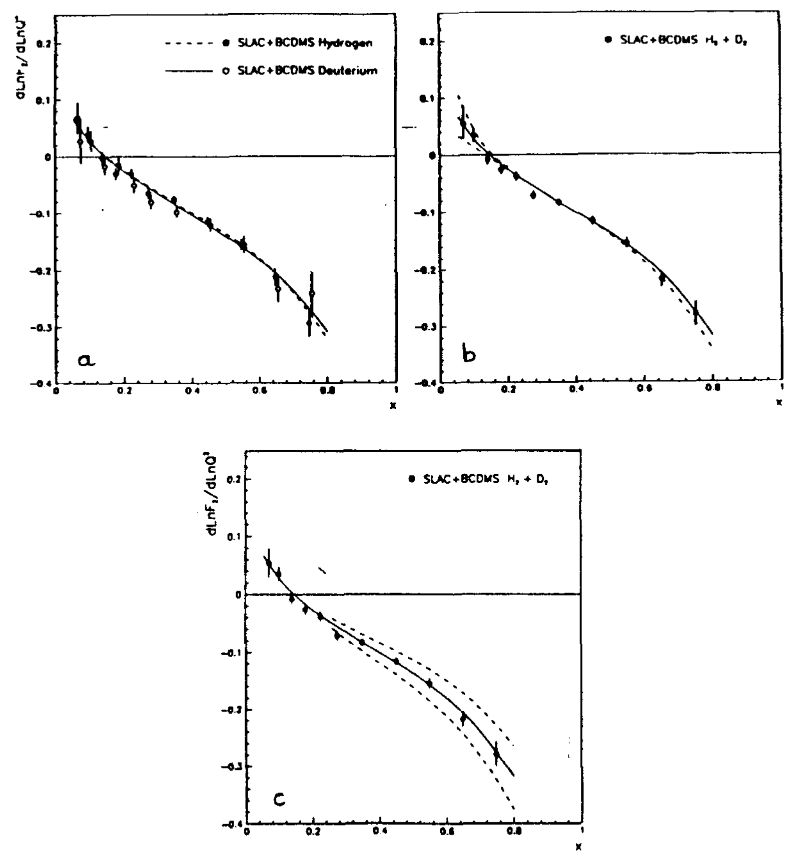

Figure 21: The logarithmic derivatives of F_2 for SLAC and BCDMS data. (a) NLO QCD fits for H_2 (D_2). (b) Averaged H_2 and D_2 logarithmic slopes: NLO QCD fit (solid line), variation if gluon distribution is varied within its errors (dashed line) and influence of higher order twist terms (dashed-dotted). (c) Sensitivity of data to α_s . The dashed lines correspond to $\Delta\alpha_s(M_Z^2) = \pm 0.010$ (twice the final error) [29].

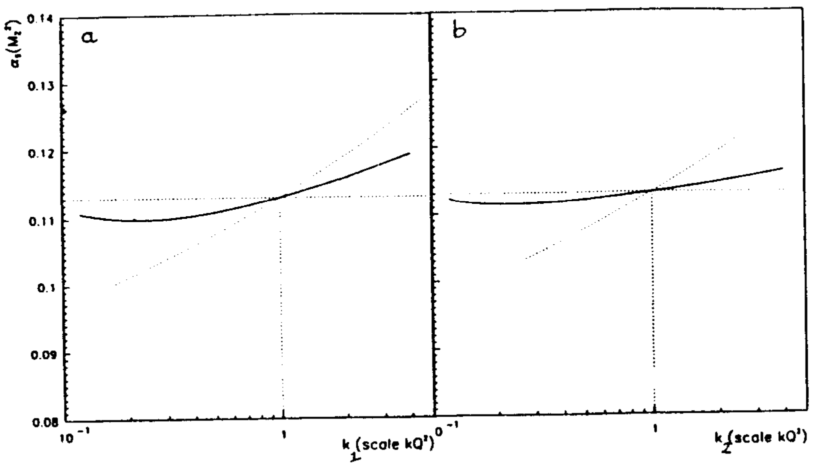

Figure 22: The variation of $\alpha_s(M_Z^2)$ from SLAC and BCDMS data as function of the factorization scale (k_1) and renormalization (k_2) scale [29].

dependence on the scale. Structure functions depend on the factorization scale $\mu_0^2 = k_1 Q^2$ and the renormalization scale $\mu^2 = k_2 Q^2$ (in the $\overline{MS}$ scheme $\mu = \mu_0 = Q$). This dependence introduces an uncertainty on α_s. To study this uncertainty, QCD fits were performed varying the parameters k_1 and k_2 [29]. The resulting values of α_s are shown in Fig. 22 as function of the scale factors k_1 and k_2. Varying the k_i coefficients within a range such that the χ^2 of the fit is not increased significantly, a theoretical uncertainty of $\Delta\alpha_s(M_Z^2) = 0.004$ is estimated. Thus

$$\alpha_s(M_Z^2) = 0.113 \pm 0.003\,(exp) \pm 0.004\,(theor).$$

An analysis by Martin *et al.* [30] using a somewhat different data set gives similar results.

Can the Running of α_s be detected in deep inelastic scattering? Given the precise data of DIS and the large range of Q^2 values available, one may ask whether the running of α_s can be detected. The deuterium data of BCDMS are shown in Fig. 23a where the overlayed fits use the *running* α_s. The Q^2-evolution without higher twist is indicated as in Fig. 19. The same fits, but now using a *constant* coupling α_s, are shown in Fig. 23b. The fits still describe the data well but much larger higher twist terms are needed. Thus the evolution of α_s and the size of higher twist terms are strongly correlated. Because of the lack of precise knowledge of higher twist terms, running of α_s can not be demonstrated at present in deep inelastic scattering [35].

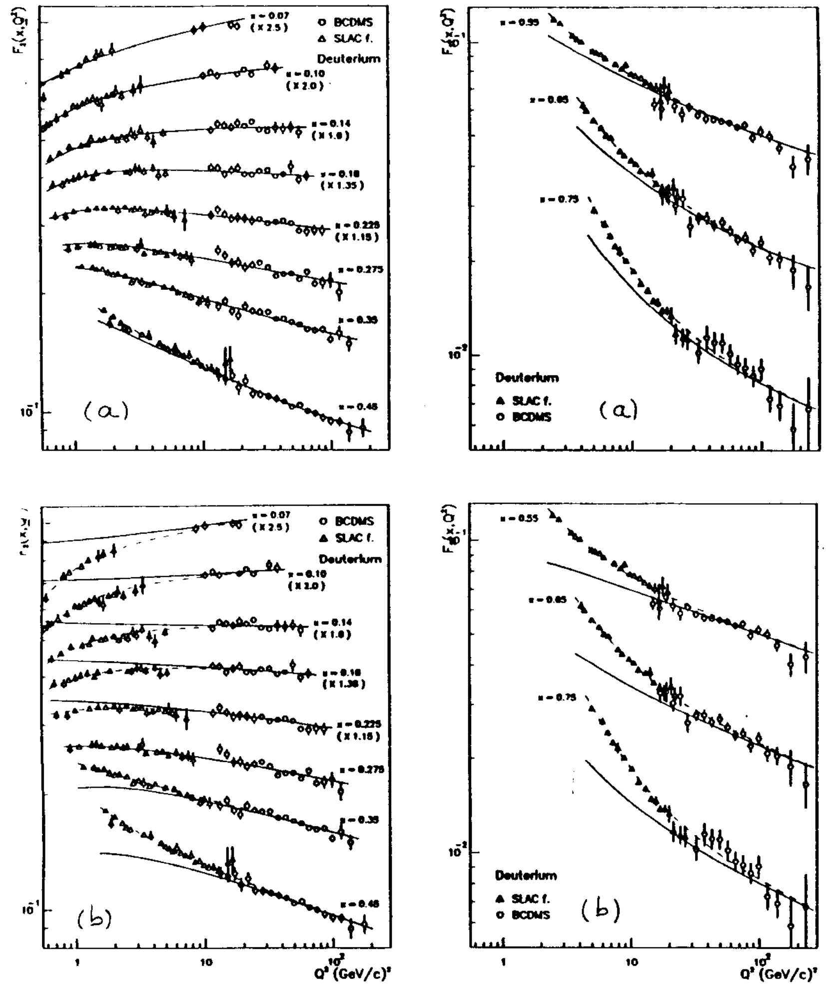

Figure 23: Deuterium data with NLO fit (dashed line). The solid line indicates the effect of higher twist terms: (a) NLO QCD fit with *running* α_s; (b) NLO QCD fit with *constant* α_s [35].

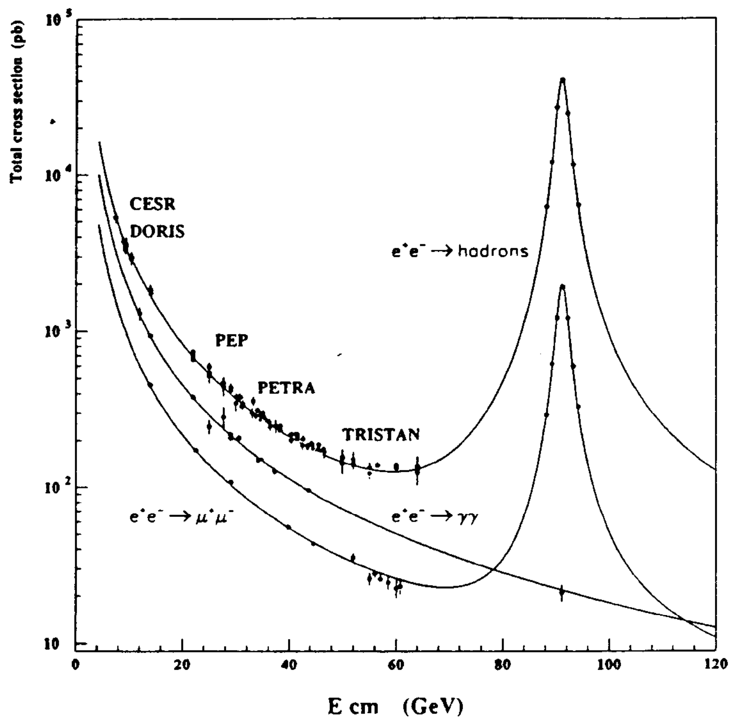

Figure 24: The total cross section for $e^+e^- \rightarrow$ *hadrons* , $e^+e^- \rightarrow \mu^+\mu^-$ and the background reaction $e^+e^- \rightarrow \gamma\gamma$.

3 QCD in $e^+e^- \rightarrow$ *hadrons*

One of the most fruitful testing grounds of QCD has been e^+e^- annihilation into hadrons at high energies. The pioneering work at PEP and PETRA is summarized in Refs. [36, 37]. The observation of 3-jet events, establishing the existence of gluons, was a breakthrough for the experimental foundation of QCD. The analysis methods developed by the PEP/PETRA experiments were readily applied to the new generation of experiments at LEP/SLC. We will restrict our lecture mainly to the more recent results of these later experiments, MarkII at SLC, ALEPH, DELPHI, OPAL and L3 at LEP [38].

Tests of QCD at the $Z°$ resonance have several advantages compared to PEP, PETRA, TRISTAN energies

1. For the production (Fig. 24):
   - The total cross section is very large $\sigma_{tot} \sim 41.4\ nb$;
   - hard initial state radiation is suppressed due to the small width of the $Z°$, $\Gamma_Z = 2.48$ GeV.
2. For the identification of the final hadronic state:
   - The fraction R of hadronic events relative to $e^+e^- \rightarrow \mu^+\mu^-$ is $R \sim 20$ compared to $R \sim 4$ at lower energies.
   - Background is easily rejected and becomes negligible (typically $\ll 1\%$).
   - Jets have higher energy and are therefore well collimated and well separated.
   - Hadronization effects are relatively small, non-perturbative contributions tend to decrease as $1/\sqrt{s}$.

In $e^+e^- \rightarrow$ *hadrons* , the initial state is completely known. There are a number of quantities, like the total cross section and various jet related quantities which can be calculated as a function of the single parameter α_s. This is a considerable advantage over deep inelastic scattering or hard hadronic collisions, where the structure functions are input as well. The disadvantage in e^+e^- is the ambiguity in the Q^2 scale for α_s: The standard value $Q^2 = s = E^2_{cm}$ is larger than the 'natural' physical scale of gluon emission in events, given that most gluons are soft.

3.1 Hadronization Models

To perform precision tests, reliable tools are needed to correct the data for acceptance and resolution. To perform tests of QCD, additional corrections are needed for hadronization: The detector measures hadrons, but the theory describes coloured quarks and gluons. One can distinguish several phases in the process $e^+e^- \rightarrow$ *hadrons* , corresponding to different time scales and governed by the electroweak theory (QFD) or by QCD (Fig. 25):

1. e^+e^-annihilation into a virtual $\gamma/Z°$ resonance, which decays into a primary $\bar{q}q$ pair ($\sim 10^{-17}$cm, QFD);
2. 'hard' gluon radiation leading to destinct jets ($\sim 10^{-15}$cm, QCD);
3. small angle radiation and gluon splitting ($\sim 10^{-14}$cm, QCD);
4. quarks and gluons combine to hadrons ($\sim 10^{-13}$cm, QCD);
5. unstable hadrons decay into experimentally observable particles (QFD and QCD).

Matrix element and parton shower models. Phase (2) is of primary interest for quantitative QCD tests: it can be calculated (approximately). There are two approaches which are shown schematically in Fig. 26.

- Matrix elements (exact 2^{nd} order calculation in α_s), and
- parton showers (leading log approximation).

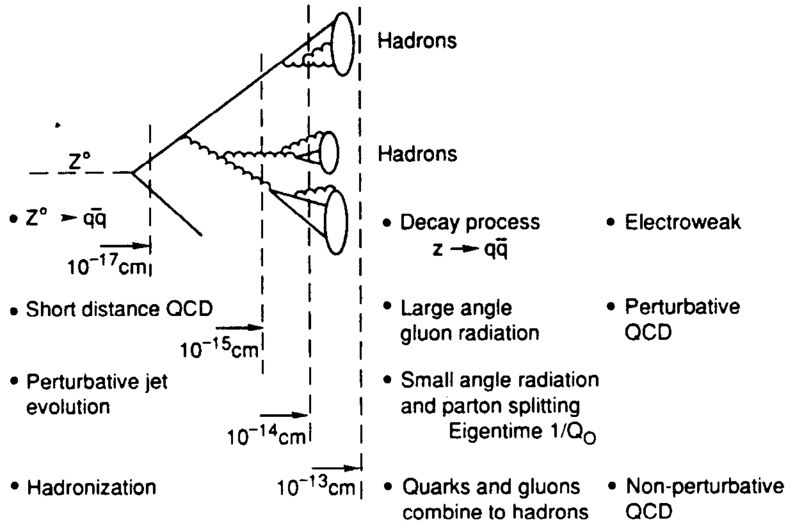

Figure 25: The stages and time scales in the evolution of a jet.

Event generators based on $\mathcal{O}(\alpha_s^2)$ matrix elements produce up to 4 partons. The parameters that control the generators are $\Lambda_{\overline{MS}}^{(5)}$, the parameter f which defines the renormalization scale $\mu^2 = f \cdot s$, and y_{min} which defines a finite jet resolution criterion by requiring that the invariant mass m of two partons obeys $m^2 \geq y_{min} s$. For two and three jets, the next-to-leading order calculation is completed [39, 40].

The parton shower picture is derived within the framework of the leading logarithm approximation (LLA), see *e.g.,* [7]. Only the leading terms in the perturbative expansion are kept. The algorithms are based on an iterative use of the basic branchings $q \to qg$, $g \to gg$ and $g \to \bar{q}q$. The probability that a branching $a \to bc$ will take place is described by the Altarelli-Parisi splitting kernels. A cutoff is introduced through an effective gluon mass usually denoted by Q_0 or $Q_0/2$, $Q_0 \sim 1\ GeV$. On the $Z°$ pole on average nine partons are generated.

The available generators are described in detail in [7]. The most popular matrix element based generators are JETSET [41] and ERT-EO [42]. JETSET can also be used in the parton shower mode. Other parton shower based generators are HERWIG [43] and ARIADNE [44].

Hadronization Models. The condensation of coloured quarks and gluons into colour neutral hadrons (phase 4 in Fig. 25), though governed by QCD, can (at present) at most be modeled. In case of $\mathcal{O}(\alpha_s^2)$ matrix element generators, at most four partons at an energy scale (invariant mass of two partons) exceeding 10 GeV are created at the $Z°$ pole. This implies that hadronization models have to bridge a

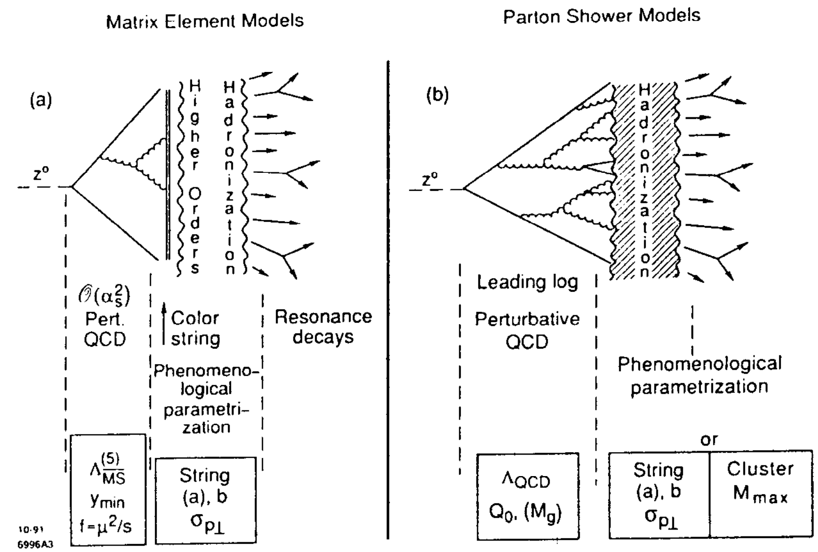

Figure 26: Schematic illustration of the parton generation and hadronization in Monte Carlo models, (a) matrix element models, (b) parton shower models. Indicated are also the parameters involved in the optimization of the models.

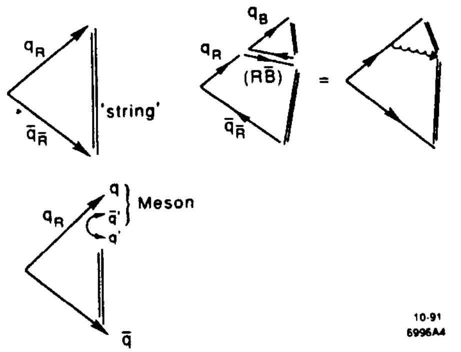

Figure 27: Schematic picture of string fragmentation.

big gap from parton to hadron level, where the latter is governed by multiplicities around 17 (before decays) and mass scales of 1 GeV and less. 'Hadronization' here describes both the condensation of partons into hadrons and the missing higher order terms in the perturbative calculation of the parton configuration. The situation is simpler for parton shower models where the parton energy scale is as low as 1 GeV and the average parton multiplicity of 9 is much closer to the final hadron multiplicity.

Two fragmentation schemes have been successful in describing the data: the string and the cluster fragmentation. The original 'independent' fragmentation scheme, though shown not to describe the data correctly, is still occasionally used to probe the dependence on fragmentation.

The string fragmentation model is based on the QCD-inspired concept of a 'colour flux tube' stretched between q and $\bar{q}$ as produced in e^+e^- annihilation. As the partons move apart the potential energy stored in the string increases and the string may break by producing a new $q'\bar{q}'$ pair, so that the system splits into two colour singlet systems $q\bar{q}'$ and $q'\bar{q}$, Fig. 27. The important parameters of the string fragmentation are a and b, influencing the longitudinal component of the hadron momenta, and $\sigma_\perp$ for the transverse component. The details of the fragmentation like flavour content can be adjusted by many more parameters.

The cluster fragmentation should be used only for developed parton configurations as obtained from parton shower generators. First, remaining gluons are split into $q\bar{q}$ pairs. Adjacent quarks and anti-quarks are then grouped into colourless clusters which decay into (two) hadrons or are split in a string-like fashion into two clusters. There is basically only one free parameter, the maximum cluster mass.

To tune the parameters of the models, global event shape variables like thrust and oblateness and inclusive distributions like particle momenta are suitable: The data corrected for detector effects are directly compared to the Monte Carlo predictions. After the models are tuned, they can be tested by comparing to the measurements the predictions for event shape variables that were not used in the

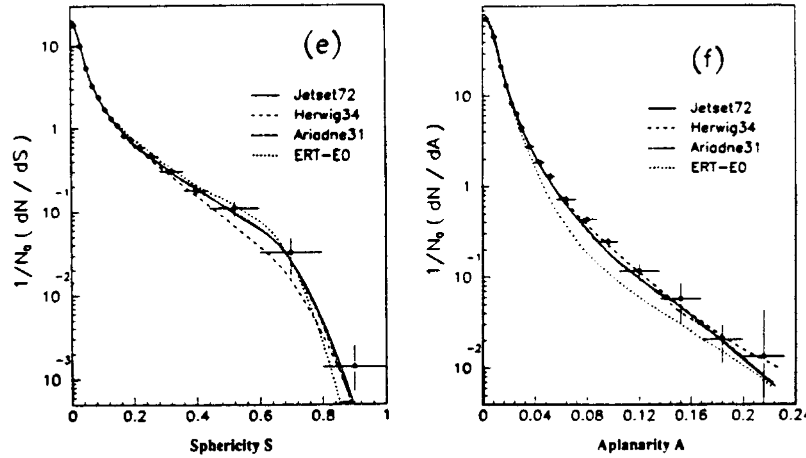

Figure 28: The unfolded event shape distributions at 91 GeV and the predictions of the QCD models with their optimized parameters [45]: Sphericity (left) and aplanarity (right).

parameter fit. Fig. 28 shows the OPAL sphericity and aplanarity distribution.

From the studies by ALEPH, OPAL and DELPHI [46, 45, 47] the following picture emerges:

1. All three Monte Carlo models considered, (JETSET matrix element, JETSET parton shower and HERWIG) reproduce the 91 GeV data.

2. Parton shower models describe the data best. The models tuned at 91 GeV can reproduce all measurements between 29 and 91 GeV, see for example, Figs. 29, 30. This means that the energy dependence is represented by the parton shower alone, the fragmentation can be treated as being *independent* of center of mass energy in the range $E_{cm} = 29 \ldots 91$ GeV.

3. Matrix element models reproduce the data in regions sensitive to 3-jets. They cannot well describe regions sensitive to higher orders, *e.g.*, the momentum out of the event plane. The parameters have to be retuned at each cm-energy. The agreement with data can be significantly improved if a much smaller optimized scale is used for α_s, $Q^2 \sim 0.002\ M_Z^2$. This is understood as higher orders being absorbed into a larger $q\bar{q}g$ rate [48]. Even then some distributions are not described as well as by parton shower generators. Despite these shortcomings matrix elements have to be used for a determination of α_s because only in the exact order by order calculation the coupling constant is well defined.

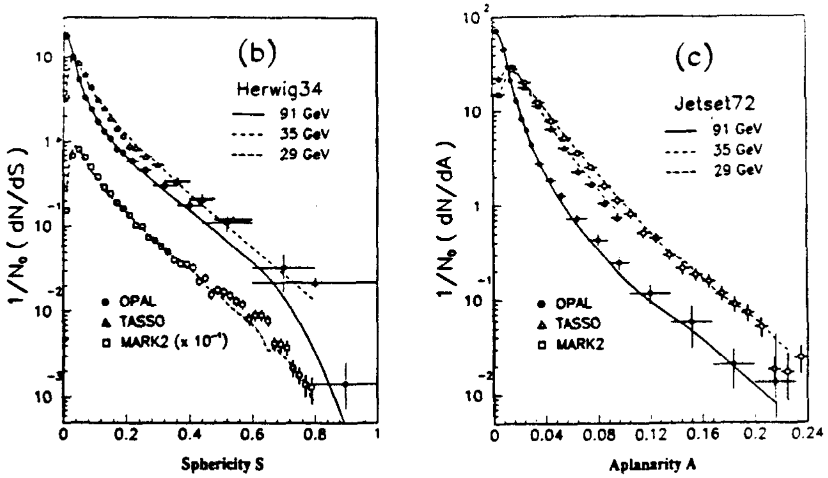

Figure 29: Unfolded distribution of the sphericity and aplanarity distribution at 91, 35 and 29 GeV, compared to the predictions of HERWIG with its parameters optimized at 91 GeV [45].

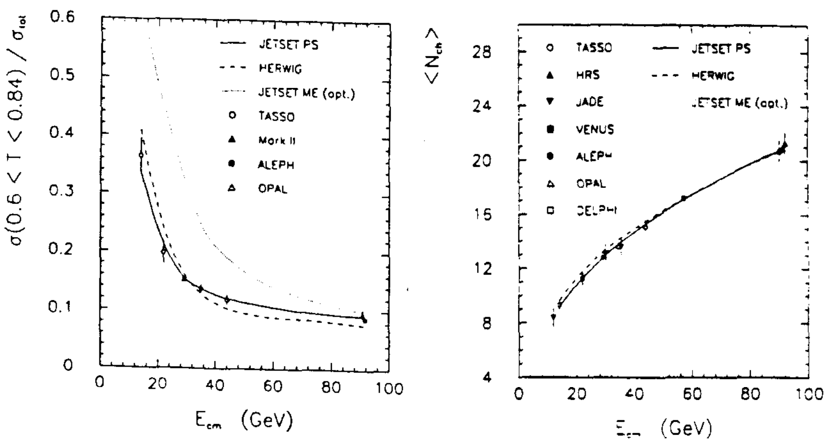

Figure 30: The average value of thrust and charged multiplicity measured at different energies compared to the prediction of parton shower and matrix element models tuned at 91 GeV [46].

The confidence in parton shower models has by now increased such that they are used to estimate the influence of missing higher orders in the matrix element approach. For any of the observables that will be discussed in the following sections, higher orders can be estimated as follows: increasing in the parton showers the cutoff from the usual value $Q_0 \sim 1\ GeV$ to $Q_0 \sim 13.5\ GeV$ reduces the average multiplicity of partons in the shower to four, thus roughly reproducing the $\mathcal{O}(\alpha_s^2)$ matrix elements. The difference in the distribution of an observable like thrust, for $Q_0 = 1\ GeV$ and $Q_0 = 13.5\ GeV$ is a rough estimate of the contribution due to higher orders.

3.2 Measurements of α_s

In e^+e^- annihilations two different methods have been applied to determine α_s:

- Measurement of the hadronic cross section or (equivalently) of the hadronic partial Z° width Γ_{had}. The total hadronic cross section is the only quantity that has been calculated in perturbation theory to $\mathcal{O}(\alpha_s^3)$ and there are no corrections due to hadronization. However the QCD correction $(1 + \frac{\alpha_s}{\pi})$ to the leading term $\Gamma^{(0)}_{had}$ is only about 4%. Very high experimental precision is therefore required: In order to reach $\delta\alpha_s = 0.005$ an accuracy of $\delta\Gamma_{had}/\Gamma_{had}$ of 0.2% is needed.
- Analysis of the event topology, in particular a study of events with hard gluon radiation. The fraction of these events is to lowest order proportional to α_s. Several observables exist that measure the hard gluon content [6]. These observables do depend on the quark and gluon hadronization. Unfortunately the matrix element calculations have been performed only to $\mathcal{O}(\alpha_s^2)$. The uncertainty due to missing higher orders is the dominant contribution to the error of α_s from this method. Few representative examples will be outlined in the following subsections.

3.2.1 The Total Hadronic Cross Section

In leading order the ratio between the total hadronic cross section and the cross section for $e^+e^- \to \mu^+\mu^-$ is obtained by summing over all kinematically accessible flavours and colours of quarks. At low energies where $\gamma-$ exchange dominates:

$$R_0^\gamma = \frac{\sum_q \sigma(e^+e^- \to \bar{q}q)}{\sigma(e^+e^- \to \mu^+\mu^-)} = N_C \sum_q Q_q^2. \tag{20}$$

With q = u, d, s, c, b one finds $R_0^\gamma = 11/3 = 3.67$. At $\sqrt{s} = 34\ GeV$ the measured value is 3.88 ± 0.06 [49]. The difference of these values is a measure for the QCD correction to the simple quark parton picture Fig. 31a. For the hadronic cross-section, in contrast to the leptonic cross section there are higher

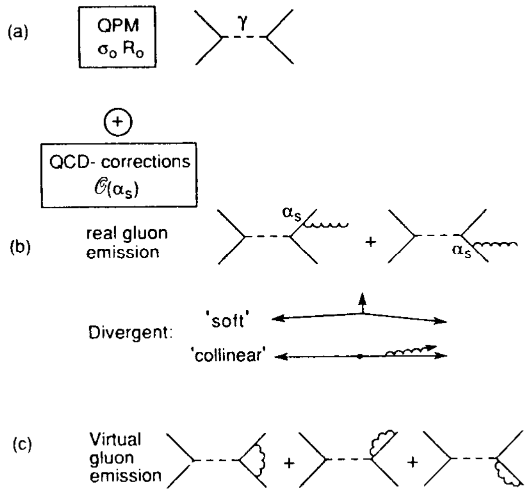

Figure 31: Diagrams contributing to the total hadronic cross section (a) quark parton model, (b) real gluon emission and (c) virtual corrections.

order strong interaction corrections from the emission of gluons in the final state. The diagrams are shown in Fig. 31b and are proportional to α_s,

$$\sigma^{q\bar{q}g} = \sigma_0 R_0 \int dx_1\, dx_2\, \frac{2\alpha_s}{3\pi} \frac{x_1^2 + x_2^2}{(1-x_1)(1-x_2)} \tag{21}$$

$$\text{with} \qquad x_i = \frac{2E_i}{\sqrt{s}} \qquad\qquad i = (1,2,3) = (q, \bar{q}, g).$$

The integral is divergent due to gluons that are collinear with either quark (collinear divergence), and gluons with small energies, $E_3 \to 0$ (infrared singularity). These divergencies are exactly cancelled by the virtual gluon corrections, Fig. 31c, and the total correction is finite. For a spin-zero gluon, the correction would be negative.

$$\sigma = \sigma^{q\bar{q}} + \sigma^{q\bar{q}g} = \sigma_0 R_0 (1 + \delta_{QCD}), \qquad\qquad \delta_{QCD} = \frac{\alpha_s}{\pi}.$$

This is the $\mathcal{O}(\alpha_s)$ correction to the hadronic cross section. δ_{QCD} has recently been calculated to $\mathcal{O}(\alpha_s^3)$ [50], for five flavours it is

$$\delta_{QCD}^{(5)} = \frac{\alpha_s}{\pi} + 1.409\,(\frac{\alpha_s}{\pi})^2 - 12.8\,(\frac{\alpha_s}{\pi})^3 + \mathcal{O}(\alpha_s^4).$$

Fig. 32 shows a global fit ($\mathcal{O}(\alpha_s^2)$) to PEP/PETRA/TRISTAN data which gives [49] $\alpha_s(\sqrt{s} = 34 GeV) = 0.135 \pm 0.012 \pm 0.010$.

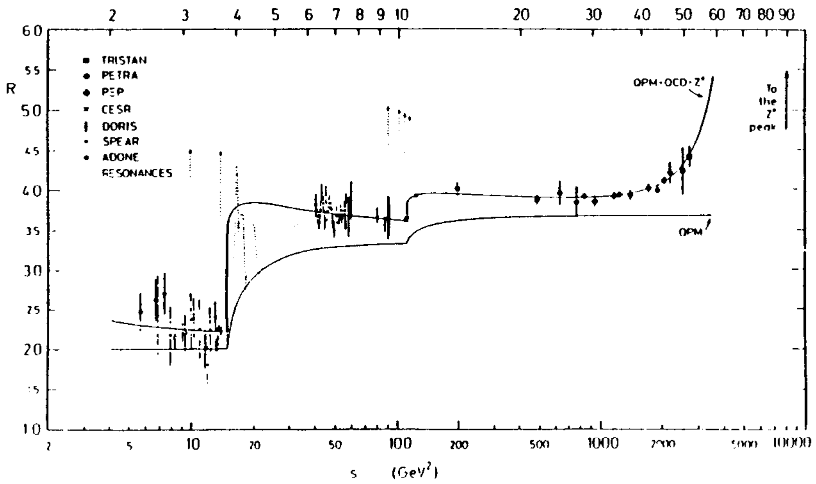

Figure 32: Compilation of R^γ values and QCD fit to e^+e^- annihilation data [49].

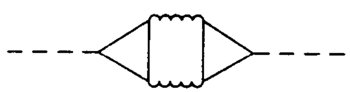

Figure 33: Diagram responsible for differences in the axial vector current contributions to the hadronic width of the Z° .

At the Z° the quark charges in eq. (20) have to be replaced by the weak charges,

$$R_0^Z = N_C \frac{\sum_q (v_q^2 + a_q^2)}{v_\mu^2 + a_\mu^2}. \tag{22}$$

Due to differences in the axial and vector current contributions to the hadronic width of the Z° , the QCD corrections to R_0^γ and R_0^Z are not identical [51, 6]. Corrections differ significantly already at order α_s. This correction and corrections due to quark masses result in [52]

$$\delta_{QCD}^Z = 1.05\,\frac{\alpha_s}{\pi} + (0.9 \pm 0.1)\,(\frac{\alpha_s}{\pi})^2 - 13\,(\frac{\alpha_s}{\pi})^3. \tag{23}$$

The error of the α_s^2 coefficient is due to the top mass uncertainty, $m_t = 129^{+32}_{-40} GeV$ [54], in the contribution from the partial width of the bottom quark.

δ_{QCD}^Z can be measured best from the ratio of the hadronic and leptonic partial

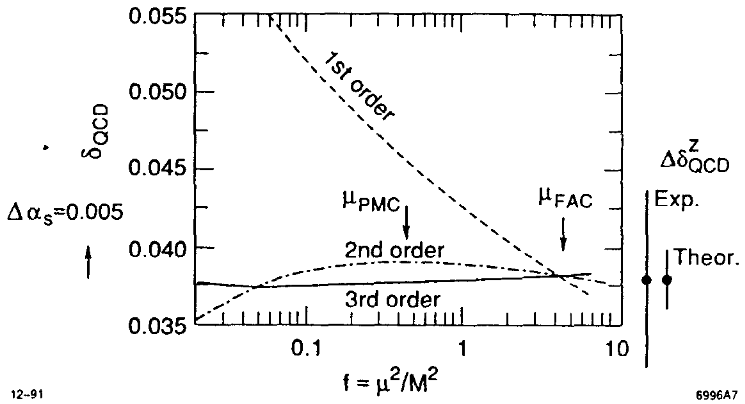

Figure 34: Dependence of the correction term δ_{QCD} on the renormalization scale μ for 1^{st}, 2^{nd} and 3^{rd} order calculations of δ_{QCD}. The optimized scales μ_{FAC} and μ_{PMS} are indicated. Shown are also the present experimental value of δ_{QCD} and its error (right) and the error that corresponds to $\Delta\alpha_s = 0.005$ (left).

Z° widths [1]:

$$1 + \delta^Z_{QCD} = \left(\frac{\Gamma_{had}}{\Gamma_{lep}}\right)_{meas} \left(\frac{\Gamma_{lep}}{\Gamma^0_{had}}\right)_{theor} = \frac{1}{19.97 \pm 0.03}\left(\frac{\Gamma_{had}}{\Gamma_{lep}}\right)_{meas}$$

Recent LEP measurements yield [54]

$$\begin{aligned} \Gamma_{had}/\Gamma_{lep} &= 20.92 \pm 0.11 \\ \text{and} \quad \delta^Z_{QCD} &= (4.7 \pm 0.6\,(exp) \pm 0.2\,(theor))\%, \\ \alpha_s &= 0.141 \pm 0.016\,(exp) \pm 0.005\,(theor). \end{aligned}$$

This result is one standard deviation higher but compatible with the measurements of α_s from shape variables that will be discussed in the following sections.

The optimized renormalization scale. δ_{QCD} is the only observable that was calculated to $\mathcal{O}(\alpha_s^3)$. It is instructive to examine the dependence on the renormalization scale μ. The cases of retaining only the first, second or third order term are shown in Fig. 34. As expected, the inclusion of higher orders leads to more stable predictions. In the absence of higher order corrections one can try to 'guess' the best choice of scale. In the literature three such choices have been advocated:

1. Fastest apparent convergence (FAC) [55]: The scale μ_{FAC} is chosen such that second and first order give the same result,
$$\delta^{[1]}_{QCD}(\mu_{FAC}) = \delta^{[2]}_{QCD}(\mu_{FAC}).$$

[1] Varying m_t between 90-200 GeV and m_H between 50-1000 GeV changes the factor at the right-hand side between 19.94 and 19.99 [53].

2. Principle of minimal sensitivity (PMS) [56]: The scale μ_{PMS} is chosen such that
$$\left.\frac{\partial \delta^{[2]}_{QCD}}{\partial \ln \mu}\right|_{\mu_{PMS}} = 0.$$

3. The Brodsky-Lepage-Mackenzie scheme [57] is based on the observation that the physical origin of the evolution of α_s is loop insertions as described in section 1.1. The scale μ_{BLM} is determined by the scale of the momenta in the loop and is hence of the order of the gluon virtuality. Similarly Kramer [58] recommends the scale $\mu = m_{qg}$, *i.e.*, the invariant mass of the quark-gluon system.

The special scales for cases (1) and (2) are indicated in Fig. 34. In general, the theoretical error on a quantity calculated to $\mathcal{O}(\alpha_s^n)$ is $\mathcal{O}(\alpha_s^{n+1})$.

3.2.2 Measurement of α_s from Event Topology

In section 3.3.1, eq. (21), we have seen that the 3-jet cross section is proportional to α_s. In leading order the differential cross section is

$$\frac{1}{\sigma}\frac{d\sigma}{dx_1 dx_2} = \frac{2\alpha_s}{3\pi}\frac{x_1^2 + x_2^2}{(1-x_1)(1-x_2)} \quad . \tag{24}$$

A variety of shape variables X (3-jet rate, thrust, oblateness, ...) has been calculated in $\mathcal{O}(\alpha_s^2)$ by integrating the second order matrix elements. The integration gives a finite result if the infrared and collinear singularities cancel. The generic result is [6]

$$\begin{aligned} \frac{1}{\sigma_0}\frac{d\sigma}{dX} &= \frac{\alpha_s(\mu)}{2\pi} A_X(X) \\ &+ (\frac{\alpha_s(\mu)}{2\pi})^2 \left[A_X(X)\cdot 2\pi b_0 \ln\frac{\mu^2}{s} + B_X(X)\right] + \mathcal{O}(\alpha_s^3), \end{aligned} \tag{25}$$

from which $\alpha_s(\mu^2)$ is to be determined for *any* renormalization scale μ. In practice μ is chosen between m_b and M_Z. The relative size of the $\mathcal{O}(\alpha_s^2)$ corrections varies from quantity to quantity. The larger the ratio r = B/A the stronger is the scale (μ) dependence. There is no optimized scale that could be used for all quantities. This is illustrated in Fig. 36 which shows the dependence of a hypothetical quantity X on the renormalization scale μ for different values of the $\mathcal{O}(\alpha_s^2)$ coefficient r [59]. However, a small B/A does not necessarily imply that also the third order coefficient is small. It is not justified to declare one variable better than another one on the basis of the numerical value of B/A.

The different LEP/SLC collaborations do not use the same renormalization scales to calculate the central value for $\alpha_s(M_Z^2)$. This has to be taken into account

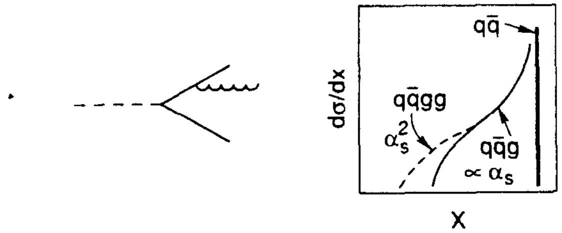

Figure 35: Schematical picture of the effet of higher orders on a shape variable, *e.g.*, thrust.

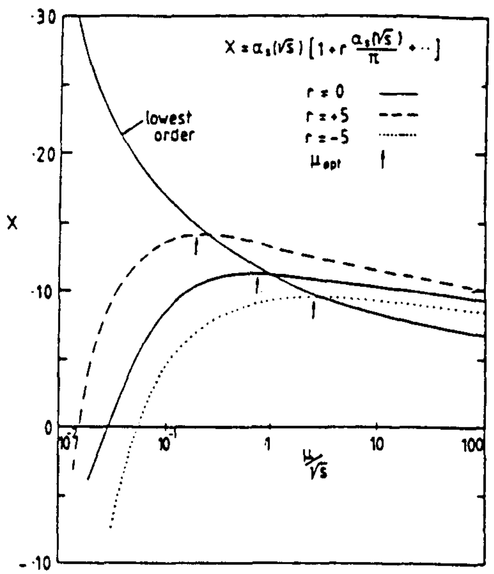

Figure 36: Dependence of a hypothetical shape variable X on the choice of scale [59].

when comparing the different results. The theoretical error $\Delta\alpha_s(theor)$ is usually estimated by a variation of the scale in a certain range, for example between m_b and $\sqrt{s}$.

Another uncertainty arises from the hadronization of the partons. The effects of hadronization decrease at least as fast as $1/\sqrt{s}$. The size of the effect can be gauged by calculating distributions such as $d\sigma/dX$ using a parton-shower Monte Carlo and switching off the final hadronization process. Different quantities have quantitatively different hadronization corrections, and the hadronization corrections may be much smaller in a restricted range of a distribution. For the price of losing statistics, the fit for α_s may then be performed in this restricted region only.

In summary the errors quoted by the experiments are of three types

$$\begin{array}{llll} \alpha_s(M_Z^2) = \alpha_s & \pm & \Delta\alpha_s(exp) & \text{statistical} \oplus \text{experimental systematic} \\ & \pm & \Delta\alpha_s(theor) & \text{higher orders} \oplus \text{fragmentation} \\ & \pm & \Delta\alpha_s(scale) & f = m_b^2/m_Z^2 \ldots 1\,. \end{array}$$

α_s from Jet Rates. In the previous section it was already shown that the cross section $e^+e^- \to q\bar{q}g$ becomes infinitely large when either the gluon momentum goes to zero or the gluon is collinear with either of the outgoing quarks. The regions of soft and collinear divergence are avoided when the invariant mass m_{ij} of two partons i, j is required to exceed a threshold $y_{cut} \cdot s$,

$$\frac{m_{ij}^2}{s} \geq y_{cut}. \tag{26}$$

In the Dalitz plot of the scaled energies x_1, x_2 the parameter y_{cut} determines the distance from the phase-space limits at which the 3-parton cross section diverges, Fig. 37. In terms of the energy fractions, eqn. (26) is equivalent to,

$$0 < x_1, x_2 < 1 - y_{cut}, \qquad x_1 + x_2 > 1 + y_{cut}.$$

With eqn. (26) we have introduced the concept of a jet measure, which is also needed for practical experiments which can not resolve soft and collinear gluons as jets. Jet algorithms are defined by the prescription for calculating the invariant mass m_{ij} ('metric') and by the prescription for combining the four momenta ('recombination'). One of the most widely used jet measures is the 'minimum invariant mass' algorithm E0. It is applied both to final state hadrons (experimental data) and partons (theoretical 'data'). For each pair of 'particles' i and j, the invariant mass squared is evaluated,

$$m_{ij}^2 = (p_i + p_j)^2 \equiv y_{ij} \cdot s.$$

The pair for which the scaled invariant mass squared y_{ij} is smallest is replaced by a pseudo-particle k with four momentum p_k,

$$p_k = p_i + p_j. \tag{27}$$

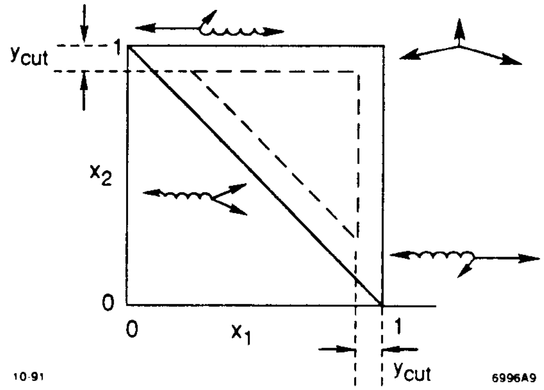

Figure 37: The 3-jet Dalitz plot of scaled energies x_1 and x_2. Depicted are the phase space bands corresponding to the cut variable y_{cut} and the divergent event configurations that lie in these bands.

This procedure is repeated until all y_{ij} exceed the jet resolution parameter y_{cut}.

Most frequently the JADE jet finder [60] is used. It replaces the center-of-mass energy $\sqrt{s}$ by the measured visible energy E_{vis}, thus 'correcting' on average for the missed energy. The experiments use as 'particles' either the calorimeter depositions or tracks measured in the tracking devices or both. The scaled invariant mass squared is evaluated as

$$y_{ij} = 2\frac{E_i E_j}{E_{vis}^2}(1 - cos\Theta_{ij}).$$

A conceptual problem arises from the fact that partons of the theory are massless. But particles have mass and when recombining particles or partons according to (27) the pseudo-particle acquires mass. Different recombination schemes (E0, E, p0, p, ...) have been studied [6, 61]. For jet counting the JADE algorithm is equivalent to the E0 scheme for 4 massless partons,

$$\begin{aligned} E0: \quad E_{ij} &= E_i + E_j \\ \vec{p}_{ij} &= (\vec{p}_i + \vec{p}_j)\frac{E_i + E_j}{\mid \vec{p}_i + \vec{p}_j \mid}. \end{aligned} \tag{28}$$

The E0 scheme is the algorithm prefered by experimentalists as it requires the smallest corrections for hadronization [61, 37].

Except for the analysis by L3 [62], where α_s is determined from jet rates measured at a fixed value of y_{cut}, the experiments apply a method that was first presented by MARKII [63] and OPAL [64, 65]: The QCD parameter α_s (and sometimes μ) are determined from the measured differential distribution $D_2(y)$,

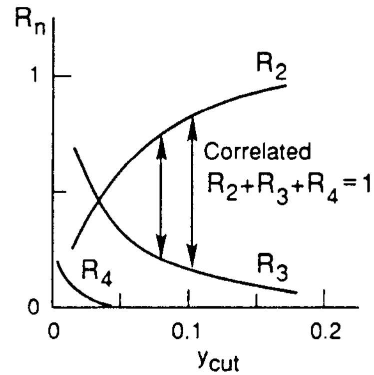

Figure 38: Schematic presentation of the n-jet rates. For $y_{cut} > 0.05$ $R_4 \sim 0$ and R_2 and R_3 are strongly correlated.

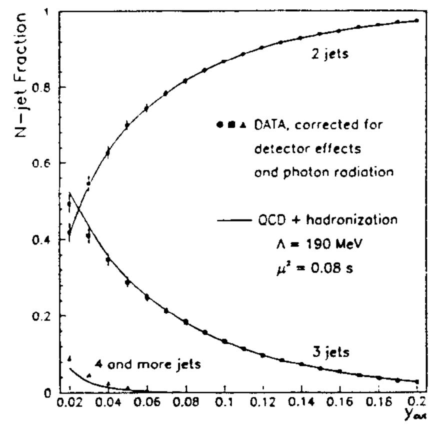

Figure 39: The jet rates measured by L3 [62].

which is defined by ($y \equiv y_{cut}$)

$$\frac{1}{\sigma}\frac{d\sigma}{dy_3} \equiv D_2(y) = \frac{d}{dy}R_2(y) = \frac{R_2(y) - R_2(y - \Delta y)}{\Delta y}. \tag{29}$$

It measures the distribution y_3 of y_{cut} values for which the classification of events changes from 3-jet to a 2-jet configuration. Fig. 39 shows the result of the direct fit to R_3 at $y_{cut} = 0.08$ for L3. Fig. 40 shows an example of the fit to $d\sigma/dy_3$ (ALEPH [66]). The fit is performed in the range $0.1 < y_3 < 0.2$, where corrections for hadronization are small. The resulting fit describes the data well beyond this range. A summary of measurements of $\alpha_s(M_Z^2)$ from jet production rates at $E_{cm} \sim 91.2\,GeV$ is given in Fig. 45 [54]. Note that each experiment quotes the central value of $\alpha_s(M_Z^2)$ for a different scale μ; however, with the exception of MARKII, scale uncertainties are considered in the respective error.

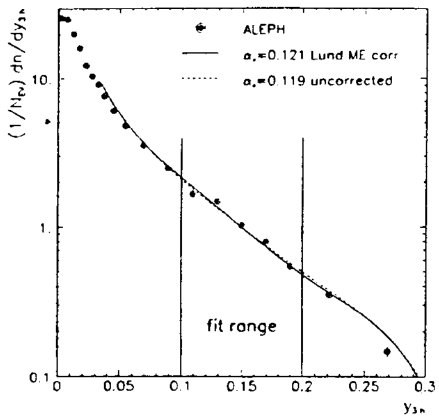

Figure 40: The differential 2-jet rate measured by ALEPH [66].

3.2.3 α_s From Energy Correlations

A quantity that is independent of the ambiguities of jet algorithms is the energy-energy-correlation (EEC) and its asymmetry (AEEC) [67]. For many years it was the most favoured observable used for α_s determinations at PEP/PETRA.

Energy-energy correlations can be defined as a histogram of all angles between particles i, j in hadronic events weighted with the product of their energies E_i, E_j:

$$EEC(\chi_{bin}) = \frac{1}{N\Delta_{bin}} \sum_{events}^{N} \sum_{i,j} \frac{E_i E_j}{E_{vis}^2} \delta(\chi_{bin} - \chi_{ij}), \qquad (30)$$

where $\delta(\chi_{bin} - \chi_{ij})$ is 1 for angles χ_{ij} inside the bin at χ_{bin} and zero otherwise; Δ_{bin} is the bin width. For 2-jet events most angles χ_{ij} are close to 0° or close to 180°, while events with hard gluon radiation contribute to the central region, Fig. 41, where the height of the 'valley' is proportional to α_s. They also contribute asymmetrically, *e.g.*, a $q\bar{q}g$ event contributes one small and two large angles, Fig. 42. Thus the asymmetry in the energy-energy correlation is positive (for $\chi > 30°$),

$$AEEC(\chi) = EEC(180° - \chi) - EEC(\chi).$$

In the AEEC hadronization effects are claimed to mostly cancel.

OPAL [68] and L3 [69] compare the integrals of both, EEC and AEEC in angular regions which are sensitive to hard gluon radiation, to several analytic calculations in $\mathcal{O}(\alpha_s^2)$ [70, 6]. They find that these different sets of calculations give different results, leading to a theoretical uncertainty of $\Delta\alpha_s(M_Z) \sim \pm 0.006$. Fig. 43 shows as an example the OPAL measurement. The uncertainty due to the scale μ is very large for the EEC (± 0.007), but is almost negligible for the AEEC. The error due to hadronization (± 0.007) has not decreased as expected.

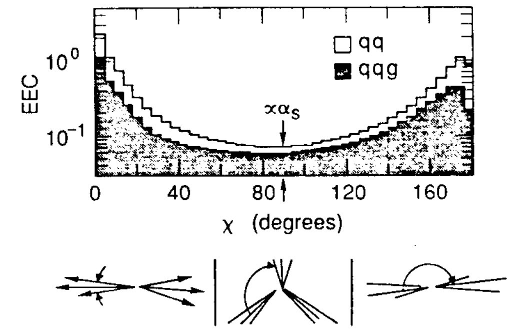

Figure 41: Schematic presentation of the EEC and the event configurations that correspond to different angular regions.

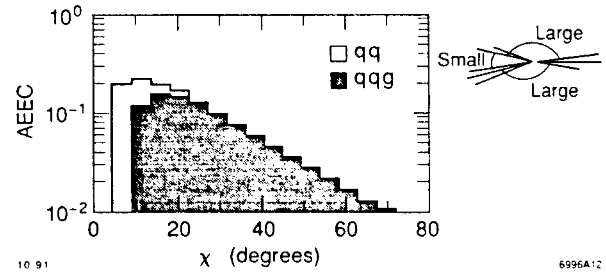

Figure 42: Schematic presentation of the AEEC and the 3-jet configuration that causes the asymmetry.

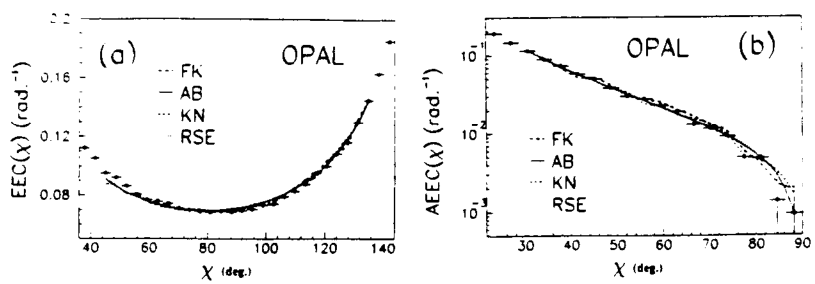

Figure 43: Data unfolded to the parton level and fits for the (a) EEC and (b) AEEC [68]. Also shown are the predictions of several theoretical calculations.

The overall average results for the LEP experiments are [54]:

$$\begin{aligned}\alpha_s(M_Z) &= 0.119 \pm 0.010 \qquad [EEC],\\ \alpha_s(M_Z) &= 0.113 \pm 0.008 \qquad [AEEC].\end{aligned}$$

3.2.4 α_s From Clustered Event Shapes

ALEPH has tried a new idea in their analysis of event shapes and of EEC [71]. Hadrons are first preclustered into jets using the JADE algorithm ($y_{cut} = 0.02$ to 0.03 typically). These jets are then treated like particles. The method compliments the previously discussed studies of jet multiplicities, since now α_s is not only determined from jet production *rates*, but also from their energies and angular distribution. ALEPH derives the theoretical distributions for clusters at the parton level from the ERT matrix elements [40] applying methods developed by Kunszt and Nason [72]. The distributions are then folded with the hadronization effects. Due to the preclustering the hadronization effects for the EEC (CEEC='cluster EEC') are reduced from $\geq 20\%$ to $\leq 5\%$.

However, the CEEC becomes more subject to the scale uncertainties known from the studies of jet production rates. The fit of α_s is independent of y_{cut} (for $y_{cut} \geq 0.0025$). The CEEC distributions, measured for two different jet resolutions y_{cut}, together with the corresponding corrections for hadronization are shown in Fig. 44.

The same method of preclustering the data can be applied to other shape parameters. The analyses have to be restricted to infrared safe quantities, *e.g.*, thrust T, oblateness O or C-parameter C [6], which can be reliably calculated in $\mathcal{O}(\alpha_s^2)$ perturbation theory. The different shape variables describe different aspects of the *same* data sample. Consequently the results are strongly correlated. Similarly, the theoretical uncertainties are strongly correlated. Covariance matrices for both the experimental and theoretical errors were derived and a weighted average for α_s calculated. The combined result is [71]

$$\alpha_s(M_Z^2) = 0.117 \pm 0.005 \qquad (\mu = M_Z/2)$$

where the error contains both experimental and theoretical errors. The combined scale dependence is given as function of the factor f, $\mu^2 = f \cdot s$,

$$\alpha_s(M_Z^2, f) - \alpha_s(M_Z^2, f = \frac{1}{4}) = 0.00356 \ln(4f) + 0.00035 \ln^2(4f),$$

which leads to a variation of $\pm^{0.006}_{0.009}$ for scales ranging from the b-quark mass up to M_Z .

The α_s measurements from shape variables are summarized for all LEP/SLC measurements in Fig. 45. The combination of these values into one value is difficult because of the correlation of the experimental errors for values from the same experiment and because of the correlation of the large theoretical errors that are

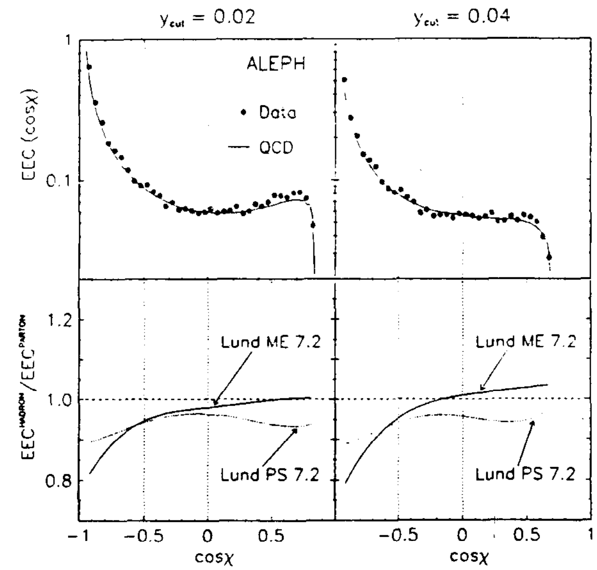

Figure 44: Measured CEEC distribution together with the ratio of the CEEC distribution on hadron and parton level for two values of y_{cut}. Also shown are $\mathcal{O}(\alpha_s^2)$ QCD predictions [71].

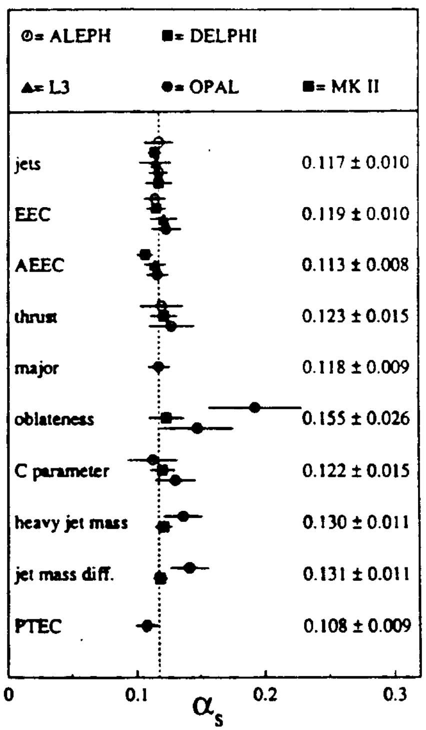

Figure 45: Summary of α_s measurements from event topology at the Z° [54].

experiment	α_s
MarkII (D2)	0.123 ± 0.010
ALEPH	$0.117^{+0.008}_{-0.010}$
DELPHI	$0.111^{+0.007}_{-0.006}$
L3	0.115 ± 0.009
OPAL	0.118 ± 0.008
LEP (topology)	0.115 ± 0.008
LEP (hadronic width)	0.141 ± 0.017

Table 2: Summary of α_s values measured at LEP/SLC [54, 63].

common to all values. The procedure of averaging chosen for the summary in [54] is: The experiments form the average of all their α_s measurements, Table 2; these values, one per experiment, are then averaged taking the theoretical error into account. The final result for the α_s value measured from the event topology at LEP becomes [54]

$$\alpha_s = 0.115 \pm 0.008$$

and is completely dominated by the theoretical error.

3.2.5 Evidence for running of α_s

The rate R_3 of 3-jet events is approximately proportional to α_s, thus the running of R_3 is a measure of the running of α_s. The latter is, however, only true if hadronization effects do not produce an energy dependence of jet rates, too. Hadronization effects are indeed within $\pm 2\%$ if jets are defined in the E0 scheme and if y_{cut} is kept constant [37]. A compilation of experimental results of R_3 is shown in Fig. 46. The data are compared with analytic $\mathcal{O}(\alpha_s^2)$ calculations [73] using two different renormalization scale factors. Similarly Fig. 47 compares the α_s values derived from measurements of AEEC at different center-of-mass energies [69, 74].

MARKII is the only experiment which covers data taken with the same detector at two different center-of-mass energies (29 GeV and 91 GeV). The results of $\alpha_s(29GeV) = 0.149 \pm 0.002 \pm 0.007$ and $\alpha_s(91GeV) = 0.123 \pm 0.007 \pm 0.007$ are consistent with the QCD prediction of a running α_s. Note that in this comparison the error due to the scale μ has not been taken into account.

Magnoli *et al.* [75] have published a detailed analysis of the event shape distributions of OPAL. They find that next-to-leading order corrections are larger then hadronization effects. This is demonstrated in Fig. 48. The narrowing of the

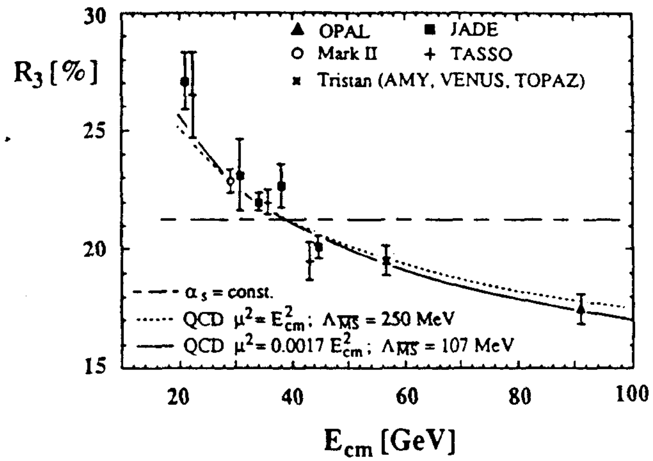

Figure 46: The energy dependence of the 3-jet rate R_3 at $y_{cut} = 0.08$, compared with several assumptions for the energy dependence of α_s [64].

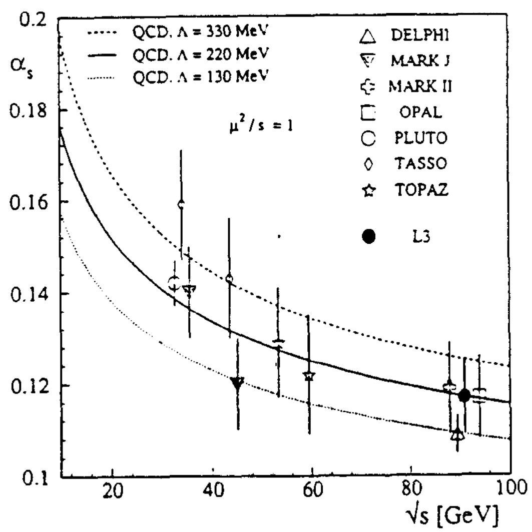

Figure 47: Energy dependence of α_s from AEEC in comparison with $\mathcal{O}(\alpha_s^2)$ QCD using the α_s value measured at 91 GeV [69].

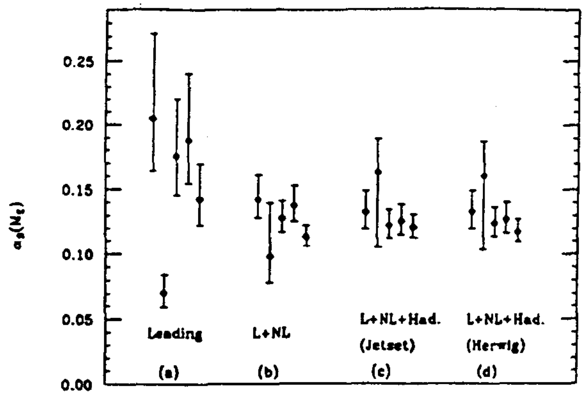

Figure 48: Various determinations of α_s. Each determination in each group corresponds to the value of $\alpha_s(M_Z^2)$ extracted (in the order) from thrust, oblateness, F-major, C-parameter, and R_3 for $y_{cut} = 0.08$ [75].

spread of values from LO to NLO is interpreted as indication for the convergence of the perturbative series.

3.3 Test of QCD Matrix Elements

With the good jet resolution and the high statistics available at LEP it is possible to perform detailed tests of the QCD matrix elements rather than extracting information from integrated quantities like the shape variables:

- From 3-jet events a clear discrimination between spin-1 vector gluons and an alternative model with scalar gluons is feasible.
- The triple gluon vertex contributes to events of type $e^+e^- \to q\bar{q}gg$. These 4-jet events can be used to distinquish between QCD and an abelian theory without boson self coupling.

These tests will become even more powerful when quark jets can be distinguished from gluon jets, for example by tagging b-quarks. At present, energy ordering is used, $x_1 > x_2 > x_3$, which assigns correctly the gluon jet to the third jet in $\sim 50\%$ of the cases. In the discussion below x_1, x_2 will be associated with the quarks and x_3 with the gluon. For 3-jet events the QCD matrix elements are available in next-to-leading order while the distributions for 4-jet final states have been calculated so far in $\mathcal{O}(\alpha_s)$ only.

3.3.1 3-Jet Events and Gluon Spin

3-jet events are described by five independent variables,

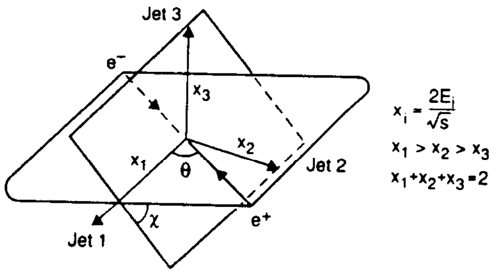

x_1, x_2	sharing of energy between the final state partons,
Θ, χ	orientation of the three-jet system,
ϕ	overall orientation.

The cross section in $\mathcal{O}(\alpha_s)$ for a vector gluon was already presented in section 3.2.1, eqn. (24)

$$\frac{d^2\sigma^V}{dx_1 dx_2} \propto \frac{x_1^2 + x_2^2}{(1-x_1)(1-x_2)}. \tag{31}$$

The cross section for scalar gluons receives different contributions from vector and axial couplings to the Z° [76]

$$\frac{d^2\sigma_v^S}{dx_1 dx_2} \propto \frac{[(1-x_1)+(1-x_2)]^2}{(1-x_1)(1-x_2)}, \tag{32}$$

$$\frac{d^2\sigma_a^S}{dx_1 dx_2} \propto \frac{[(1-x_1)+(1-x_2)]^2}{(1-x_1)(1-x_2)} - 2(1+x_3).$$

The cross section for vector gluons develops a pole for $x_1 > x_2 \to 1$, whereas the cross section for scalar gluons remains finite. This very different behaviour is the basis for the demonstration of the gluon spin. Since x_1 and x_2 close to 1 corresponds to the regions of phase-space most sensitive to the gluon spin, a y_{cut} value as small as possible is desirable. The distribution of x_2, the scaled energy of the 'radiating quark', is especially sensitive. A quantity that is sensitive to the orientation of the jets is the Ellis-Karliner angle Θ_{EK}, $\cos\Theta_{EK} = \frac{x_2 - x_3}{x_1}$ [77] .

The distribution of the scaled energies and the angles as measured by L3 [78] are shown in Fig. 49 for a small value of y_{cut}. Fig. 50 shows the average values as function of y_{cut}. As expected the rejective power of the data is largest at small values of y_{cut}. These distributions fully support the vector nature of the gluon.

3.3.2 Four Jet Events and the Triple Gluon Vertex

A key property of QCD is the self-interaction of gluons, a consequence of the non-zero colour charges of the gluons. The confinement of the quarks is hardly

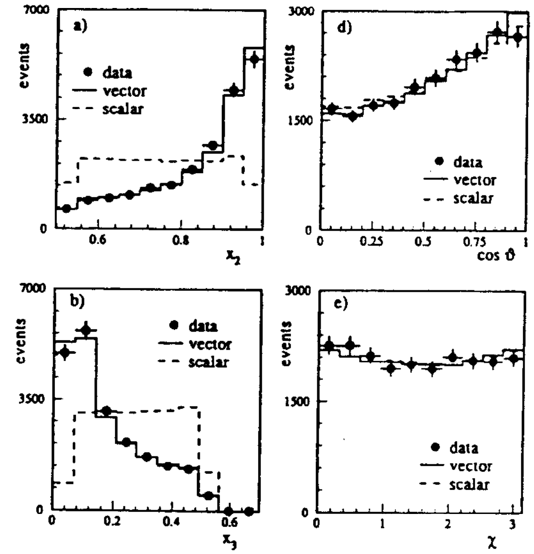

Figure 49: Comparison of measured and predicted distributions of 3-jet events for $0.02 < y_{cut} < 0.05$. The solid and dashed lines show the prediction for vector and scalar gluons, respectively [78].

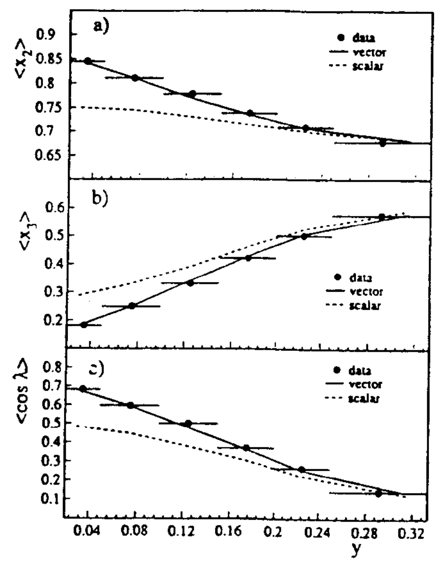

Figure 50: As Fig. 49 but the variables are shown as function of y_{cut} [78].

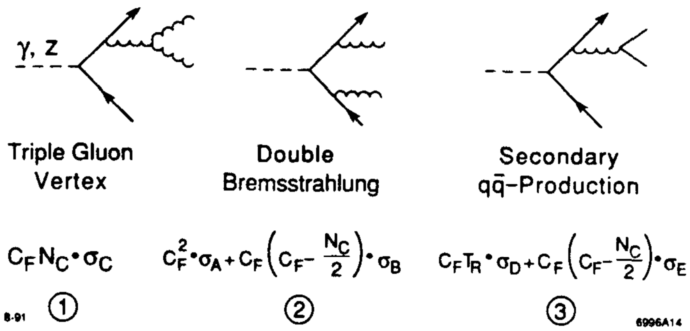

Figure 51: The diagrams contributing to 4-jet events and their colour factors.

understandable without the existence of the self-coupling of the gluons and a colourless gluon would lead to the decay $\Upsilon \to 2\ jets$ which is not observed. The large two-jet rate for medium jet energies at hadron colliders cannot be explained without the gluon-gluon scattering.

The triple-gluon vertex in $e^+e^- \to hadrons$ enters in second and higher orders of α_s. The principal $\mathcal{O}(\alpha_s^2)$ contributions, double-bremsstrahlung, triple gluon vertex and secondary $q\bar{q}$-production, yield four-parton final states and are shown in Fig. 51. In an abelian theory the triple-gluon vertex is absent. Adjusting in an abelian toy-model the quark-'gluon' coupling as $\alpha_s^A = \frac{4}{3}\alpha_s^{QCD}$, the total hadronic e^+e^- annihilation cross section, the three jet rate and their distributions can be described. Large discrepancies between QCD and this toy-model however occur in 4-jet events. Whereas the dominant contribution in QCD is due to the triple gluon diagram and the 4-quark final state is highly suppressed, in the abelian model the $q\bar{q}q'\bar{q}'$ contribution rises to the same level as the $q\bar{q}g_A g_A$ bremsstrahl cross section [79]. This induces characteristic differences in the 4-jet distributions.

Gluons radiated from quarks and antiquarks in $e^+e^- \to q\bar{q}g$ are linearly polarized to a high degree *in* the $q\bar{q}g$ final state plane [80]. Denoting the cross sections for polarizations in and perpendicular to this plane by $d\sigma_\parallel$ and $d\sigma_\perp$, respectively, QCD predicts a polarization

$$\mathcal{P}(x_3) = \frac{d\sigma_\parallel - d\sigma_\perp}{d\sigma_\parallel + d\sigma_\perp} = 2\frac{1 - x_3}{x_1^2 + x_2^2}. \tag{33}$$

The fragmentation of a linearly polarized gluon into partons depends on the azimuthal angle χ between the final state plane and the polarization vector. The asymmetric term is just opposite in sign for gg and $q\bar{q}$ decays [81],

$$\begin{aligned} D_{g\to gg}(z,\chi) &= \frac{6}{2\pi}\left[\frac{(1-z+z^2)^2}{z(1-z)} + z(1-z)\cos 2\chi\right], \\ D_{g\to qq}(z,\chi) &= \frac{1}{2\pi}\left[\frac{z^2+(1-z)^2}{2} - z(1-z)\cos 2\chi\right]. \end{aligned} \tag{34}$$

Theory	N_C	T_R	C_F
QCD	3	$\frac{n_f}{2}$	$\frac{4}{3}$
SU(N)	N	$\frac{n_f}{2}$	$\frac{1}{2}(N - \frac{1}{N})$
abelian model	0	$3n_f$	1
QED	0	1	1

Table 3: Group constants for different models.

Quark jets accumulate perpendicular to the polarization vector with a maximal asymmetry $\propto [1 - \cos 2\chi]$ for $z = \frac{1}{2}$. The asymmetry for gluon jets is less pronounced, $\propto [1 + \frac{1}{9}\cos 2\chi]$, even for $z = \frac{1}{2}$, so that the angular distribution in QCD is quite distinct from abelian theories.

Several angular distributions have been proposed to distinguish QCD from a QED-like abelian theory [82, 79] and have been successfully applied by experiments [83]. They allow to discriminate against specific abelian toy models. Given the precise data available at LEP, it has become possible to test the $\mathcal{O}(\alpha_s^2)$ matrix elements more directly, which allows to discriminate against abelian models in general. The differential cross section for the production of 4-parton final states can be written as linear combination of gauge invariant terms [40]

$$\begin{aligned} d^5\sigma = \left(\frac{\alpha_s(Q^2)}{\pi}\right)^2 \Big\{ &\left[C_F^2\,\sigma_A + C_F(C_F - \frac{N_C}{2})\,\sigma_B\right] \\ &+ \left[C_F T_R\,\sigma_D + C_F(C_F - \frac{N_C}{2})\,\sigma_E\right] \\ &+ C_F N_C\,\sigma_C \Big\}. \end{aligned} \tag{35}$$

The cross sections $\sigma_A, \ldots, \sigma_E$ depend only on phase space, i.e., on the scaled invariant mass of the parton pairs

$$y_{ij} = \frac{(p_i + p_j)^2}{s}, \qquad i \neq j,$$

which are five independent variables. For abelian theories $N_C = 0$. Table 3 summarizes the values of the coulour factors for different theories.

From the shape of the normalized differential cross section the ratio of the coefficients N_C/C_F and T_R/C_F (or T_F/C_F, $T_F = T_R/n_f$) can be determined. ALEPH [84] selects out of 70 000 hadronic Z° decays 4000 4-jet events with a JADE-jet resolution parameter $y_{cut} = 0.03$. The colour factor ratios are determined by a maximum likelihood fit to the measured five-fold differential cross section in the variables y_{ij}. The DELPHI analysis [85] uses the angular distributions of the

	N_C/C_F	T_F/C_F
QCD	2.25	0.375
abelian model	0	3
ALEPH	$2.20 \pm 0.25 \pm 0.3$	$.65 \pm 0.2 \pm 0.4$
DELPHI	$1.87 \pm 0.38 \pm 0.15$	0.20 ± 0.45
LEP	2.0 ± 0.3	0.3 ± 0.2

Table 4: Expected and measured values for the group constants; the first error is statistical and the second due to systematics of the detector simulation [84, 85].

jets. Table 4 summarizes the theoretical expectations and the values measured by DELPHI and ALEPH. The results exclude any abelian model with a significance of more than 5 standard deviations.

3.4 Leading Log QCD

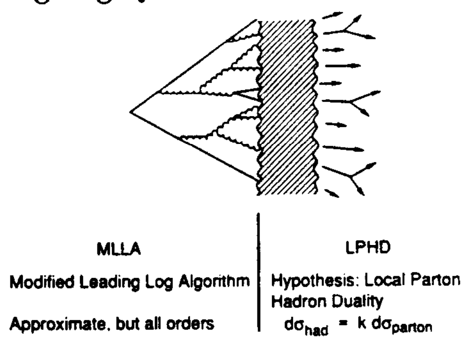

In the previous section we discussed hard processes with large Q^2 for which α_s is small and perturbative calculations are possible. Down to small Q^2 , parton shower models have proven to describe the data very successfully. They are based on the leading log approximation (LLA) of QCD, which predicts both the gluon multiplicity and the shape of the energy spectrum with only a scale Λ as free parameter. The LLA takes into account interference effects between soft gluons, as prescribed by Quantum Mechanics, with the result that not only the energies decrease in successive splittings, as described by the Altarelli-Parisi equations, but also the angles. This angular ordering is explained in appendix B. Predictions for the multiparton distributions must be related to the final state hadron distributions. The 'Local Parton Hadron Duality' (LPHD) model [86] suggests that the

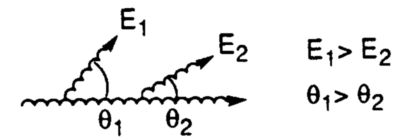

Figure 52: Schematic illustration of the energy and angular ordering in a parton shower.

calculated parton distribution is directly proportional to the hadron distribution,

$$d\sigma_{had} = K\, d\sigma_{parton}.$$

3.4.1 Particle spectra

As a consequence of angular ordering less phase space is available for low energy gluon radiation and the particle yield at low momenta decreases. A sensitive test variable is $\xi = \ln \frac{1}{x_p}$, where $x_p = \frac{2p}{\sqrt{s}}$ denotes the ratio of the particle momentum p to the beam energy $\sqrt{s}/2$. The modified leading log approximation (MLLA)

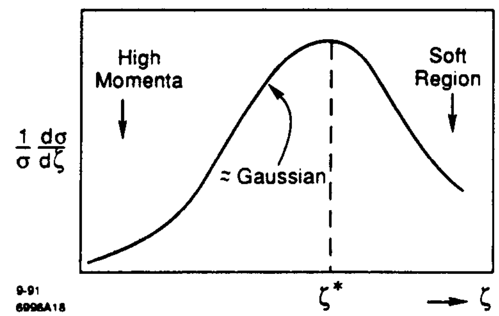

Figure 53: Schematic illustration of the logarithmic inverse momentum spectrum $\xi = \ln \frac{1}{x_p}$ as predicted by MLLA and LPHD.

[87], which takes into account all leading and next-to-leading logarithmic terms predicts the scaled distribution of ξ,

$$\frac{1}{\sigma_0}\frac{d\sigma}{d\xi} = K_{LPHD}(Y) \cdot f_{MLLA}(\xi, Y, \lambda) \qquad (36)$$

$$\text{where} \qquad Y = \ln \frac{\sqrt{s}}{2\Lambda_{eff}}, \qquad \lambda = \ln \frac{Q_0}{\Lambda_{eff}}.$$

The theoretical predictions involve three parameters: an effective scale Λ_{eff} (not directly related to $\Lambda_{\overline{MS}}$), a cut-off parameter Q_0 in the quark-gluon cascade, and the overall normalization factor K that depends on the particle type and is expected to be independent of the center-of-mass energy. The predicted spectrum shows a maximum that is shifted to lower values with increasing Λ_{eff}.

The spectrum becomes insensitive to Q_0 for large $\sqrt{s}$. The 'limiting spectrum' is $Q_0 = \Lambda_{eff}$.

In the case of charged particles [88, 89] and π^0 mesons [90] good agreement with the limiting spectrum has been observed. The data exhibit the expected peak ('hump-back') and follow a gaussian distribution in the vicinity of the peak $| \xi - \xi_{max} | \leq 1$. The value of Λ_{eff} fitted at $\sqrt{s} = 91\ GeV$ describes well also the data at lower energy, Fig. 54a.

The energy dependence of the peak is well reproduced. Fig. 55 shows the evolution of the maximum compared to the MLLA prediction. The peak position moves from ~ 4 for light mesons (π^0) [90] to ~ 3 for the heavy K^0 [91]. The same value of Λ_{eff} is supposed to describe the spectra of the light and the heavy hadrons, whereas Q_0 should be related to the particle mass. OPAL has demonstrated that the parameter choice $Q_0 = 300\ MeV$, $\Lambda_{eff} = 150\ MeV$ describes their K^0 data better than the limiting spectrum that is too narrow and gives a high value $\Lambda_{eff} = 827 \pm 30\ MeV$, Fig. 54c [91].

Unfortunately this good agreement between QCD formulae and measured hadron distributions does not yet prove colour coherence. The OPAL collaboration has compared the measured ξ distribution also to the prediction of the parton shower models with and without coherence effects [88]. They find best agreement of the low energy data with models based on coherent gluon emission. Choosing incoherent parton branchings and string fragmentation the description of the energy dependence of the maximum becomes somewhat worse (2.8σ) but is still acceptable, Fig 54b.

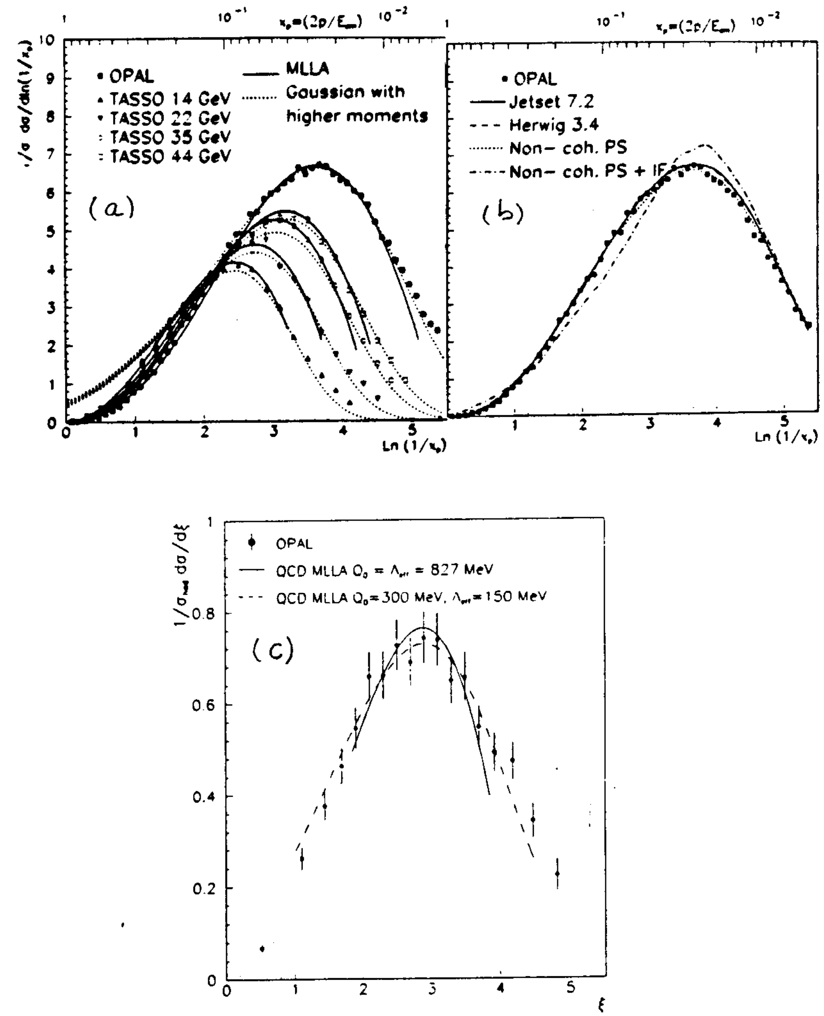

Figure 54: (a) $\xi = \ln 1/x_p$ distributions at several different cm energies compared with the analytic prediction of MLLA using parameters fitted at 91 GeV. (b) $\ln 1/x_p$ distribution at 91 GeV compared with QCD Monte Carlos [88]. (c) $\ln 1/x_p$ distribution for K^0's. The curves show the MLLA predictions for the limiting spectrum (solid) and for $\Lambda_{eff} \neq Q_0$ (dashed) [91].

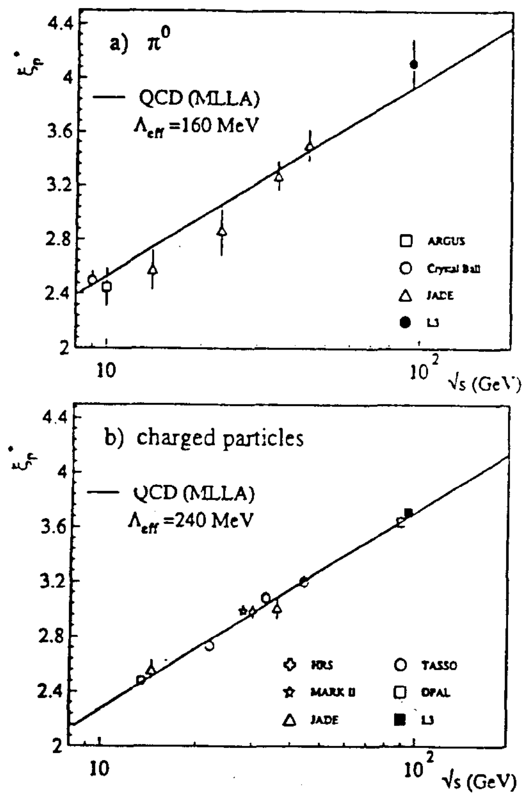

Figure 55: Evolution with cm energy of the peak positions in the $\xi = \ln 1/x_p$ distributions: (a) for π^0's, (b) for all charged particles [90].

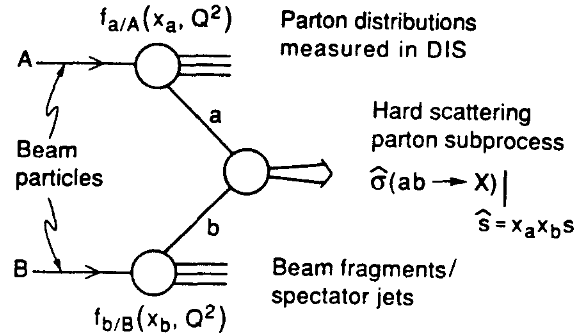

Figure 56: Schematic presentation of hard hadron-hadron scattering via a hard parton-parton subprocess.

4 QCD in hard hadron-hadron collisions

In this chapter the parton model will be applied to processes involving two hadrons in the initial state. After the general discussion of hard scattering processes the tests of perturbative QCD will be demonstrated for three processes: jet production, direct photon production and high $p_\perp$ W/Z boson production.

4.1 General structure of hard scattering processes

The hard scattering between two hadrons is the result of an interaction between the quarks and gluons which are the constituents of the incoming hadrons. The parton model for hard scattering events is depicted in Fig. 56. Since quarks carry only a fraction x_a, x_b of their parent hadron's momentum the available center-of-mass-energy $\sqrt{\hat{s}}$ is less than the overall hadron-hadron collision energy $\sqrt{s}$, $\hat{s} = x_a x_b s$. The parton density of a in A is denoted by $f_{a/A}(x_a, Q^2)$. The characteristic scale of the hard scattering is Q. The short distance cross section for the scattering of partons of type a and b is denoted by $\hat{\sigma}(ab \to X)$.

Improved parton model: Example of W production. Consider as a specific example W production in $\bar{p}p$ collisions. The parton model cross section for this process can be written [1]

$$\begin{aligned} \sigma(\bar{p}p \to W + \ldots) &= \int_0^1 dx_a \int_0^1 dx_b\, q(x_a)\, \bar{q}(x_b) \hat{\sigma}^{[0]}(\bar{q}q \to W) \qquad (37) \\ \text{with} \quad \hat{\sigma}^{[0]} &= \frac{4\pi\alpha^2}{3} \frac{1}{\sin^2\Theta_W}\, \delta(\hat{s} - M_W^2) \equiv \hat{\sigma}_W\, \delta(x_a x_b - \tau), \end{aligned}$$

[1] Summation over quark-antiquark pairs and initial and final colours has been omitted.

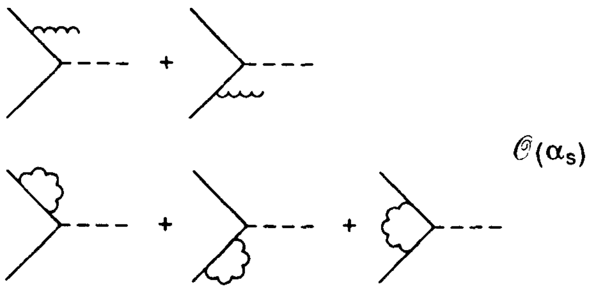

Figure 57: The $\mathcal{O}(\alpha_s)$ diagrams for heavy boson production.

where $\tau = \hat{s}/s = M_W^2/s$ has been introduced. $\hat{\sigma}^{[0]}$ and $\hat{\sigma}_W$ are the parton model cross sections that in the leading approximation can be calculated in the same way as the cross section for a QED process.

The next-to-leading corrections are shown in Fig. 57. The corresponding cross section is

$$\hat{\sigma} = \hat{\sigma}_W \Big[\delta(x_a x_b - \tau) + \frac{\alpha_s(\mu)}{2\pi} \frac{1}{x_a x_b} \Big\{ f(z) + 2P(z) \ln \frac{M_W^2}{k^2} \Big\} + \ldots \Big], \tag{38}$$

where $z = \tau/(x_a x_b)$. P(z) is, as in deep inelastic scattering, the probability to radiate a gluon. The new terms consist of a finite correction f(z) and a logarithmically divergent contribution due to gluons that are collinear with either of the initial quarks. This divergent term can be split into two terms

$$\ln \frac{M_W^2}{k^2} = \ln \frac{M_W^2}{Q^2} + \ln \frac{Q^2}{k^2} \,.$$

The term $\ln M_W^2/Q^2$ is finite and can be added to the finite correction f(z). The divergence of the second term can be absorbed in Q^2-dependent structure functions $q(x, Q^2)$,

$$\begin{aligned} \sigma(\bar{p}p \to W + \ldots) = & \int_0^1 dx_a \int_0^1 dx_b \, q(x_a, Q^2) \, \bar{q}(x_b, Q^2) \, \hat{\sigma} \\ & \cdot \Big[\delta(x_a x_b - \tau) + \\ & \frac{\alpha_s(\mu)}{2\pi} \Big\{ \frac{1}{x_a x_b} f(z) + \frac{2}{x_a x_b} (P(z) \ln \frac{M_W^2}{Q^2} - C(z) \Big\} + \ldots \Big] . \end{aligned} \tag{39}$$

The leading order term is the parton model result with $q(x) \to q(x, Q^2)$. The term $\{\ldots\}$ is a finite next-to-leading order correction. The term $[1 + \frac{\alpha_s}{2\pi}\{\ldots\}]$ is called the K-factor. The size of this $\mathcal{O}(\alpha_s)$ correction depends on the W-mass and on the overall center-of-mass energy. For W, Z° production the $\mathcal{O}(\alpha_s)$ correction increases the lowest order cross section by about 25% [2],

$$K_W \simeq 1 + \frac{8\pi}{9} \alpha_s(M_W^2) \sim 1.25.$$

For the similar Drell-Yan process, where the masses are smaller ($m_{\mu\mu}^2 \sim 10 \; GeV^2$) we find typically $K_{DY} \simeq 1.8$, showing a considerable correction [2],

$$K = 1 + \frac{\alpha_s}{2\pi} \frac{4}{3} (1 + \frac{4}{3} \pi^2) \sim 1.8.$$

The overall structure of the expression (39) is completely general,

$$\begin{aligned} \sigma(AB \to X + \ldots) = & \int_0^1 dx_a \int_0^1 dx_b \, q_{a/A}(x_a, Q^2) \, q_{b/B}(x_b, Q^2) \\ & \cdot \hat{\sigma} \Big(s, \frac{M^2}{s}, \frac{M^2}{Q^2}, \frac{M^2}{\mu^2}, \alpha_s \Big) \end{aligned} \tag{40}$$

with M an appropriate kinematic variable for the final state X, *e.g.* $M = M_W$, $M_{\mu\mu}$(Drell-Yan), $M_{jet,jet}$.

In (39) an arbitrary scale ('factorization scale') was introduced to separate off a 'QCD-improved' quark distribution. Just as for the renormalization scheme there is now a factorization scheme. It has two ingredients: the choice of factorization scale Q^2 and the choice of $C(x)$ in the definition of $q(x, Q^2)$. If the subprocess cross section is only known to lowest order then a sensible guess must be made for the scale, usually $Q^2 \sim \mu^2 \sim M^2$. Cross sections calculated to all orders should be independent of the choice of the factorization scheme and renormalization scheme.

4.2 Parton luminosities

A useful concept to estimate cross sections at hadron colliders are 'parton luminosities' [4, 2]. In the example of W production, eqn. (37) can be written

$$\begin{aligned} \sigma(\bar{p}p \to W + \ldots) &= \frac{\pi \alpha^2}{3 \sin^2 \Theta_W} \frac{1}{s} \int dx_a dx_b \, q(x_a) \, \bar{q}(x_b) \delta(x_a x_b - \tau) \\ &= c_W \cdot \frac{1}{s} \cdot \frac{d\mathcal{L}_{q\bar{q}}}{d\tau}. \end{aligned}$$

$d\mathcal{L}_{q\bar{q}}/d\tau$ is called the parton luminosity since multiplying the parton cross section $\hat{\sigma} \sim c_W/\hat{s} = c_W/\tau s$ by $d\mathcal{L}/d\tau$ gives the particle cross section $d\sigma/d\tau$ in $\bar{p}p$ collisions.

Likewise for any hard scattering processes $ij \to X$, where the final state has a mass of order $\sqrt{\hat{s}} = \sqrt{\tau}\sqrt{s}$, we have

$$\sigma_X = c_X \cdot \frac{1}{s} \cdot \frac{d\mathcal{L}_{ij}}{d\tau}.$$

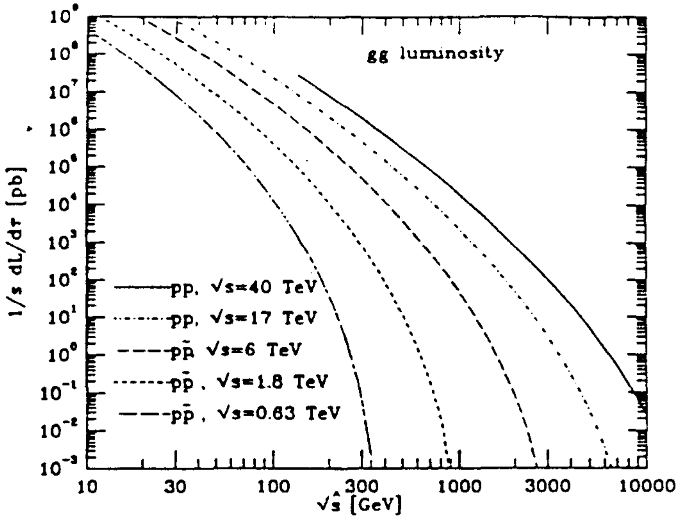

Figure 58: Luminosity for the gluon-gluon subprocess at the cm energy of several existing and projected hadron-hadron colliders [4].

In the approximation of scaling parton distributions and a parton cross section that depends only on τ, c_X is dimensionless and depends only on the coupling of (ij) to X. To estimate the cross section in hadron collisions it is sufficient to know the luminosity functions $\frac{1}{s}\frac{d\mathcal{L}_{ij}}{d\tau}$ for the parton pairs (i,j) as function of s and $\hat{s}$. An example for gg-luminosities at hadron colliders is shown in Fig. 58 [4].

We have now the ingredients available to calculate cross sections. Fig. 59 shows the predicted W/Z cross sections [4], which agree well with the measurements from the $\bar{p}p$ collider experiments [92]. Cross sections for the production of direct photons and virtual photons (Drell-Yan process) are shown in Fig. 60. These are data that are sensitive to the gluon distribution and the sea quark distribution, respectively. They provide complementary information to the deep inelastic data and are used to supply additional constraints to the structure function fits [93]. The three processes that will be discussed in more detail in the following sections are summarized in Fig. 61, which is representative for the quality of the leading order (LO) QCD predictions: Cross sections are fairly well described over about 10 orders of magnitude of change in cross section and over a range of $Q \sim p_\perp$ of $\mathcal{O}(100\ GeV)$. Hadron-hadron collisions provide the highest center-of-mass energies where new heavy particles may be discovered. At several stages along this lecture we will look beyond QCD to probe for signs of new physics.

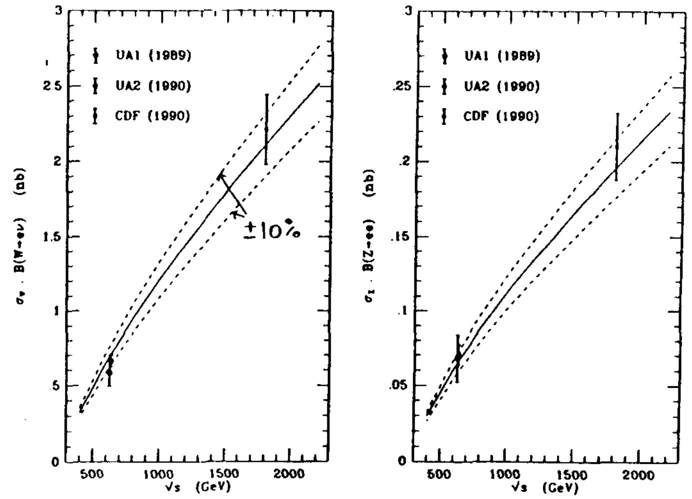

Figure 59: Predictions of W and Z° cross sections compared with measurements [4].

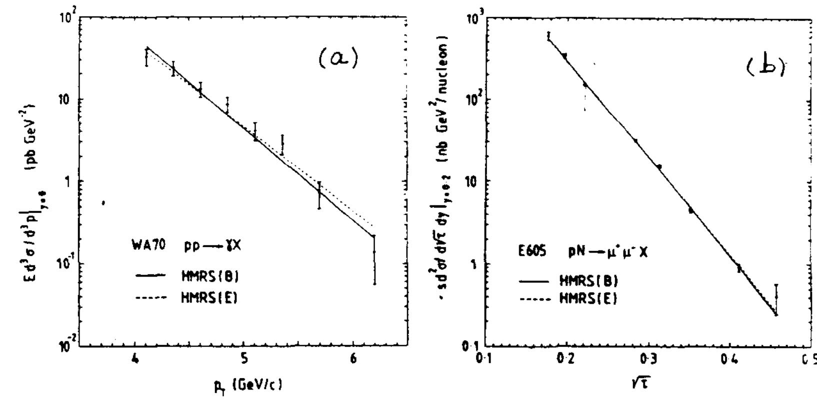

Figure 60: (a) NLO QCD predictions for direct photon production. (b) NLO QCD prediction for virtual photon production (Drell-Yan process). These data are used to constrain the sea-quark distribution in structure function fits [4, 94, 95].

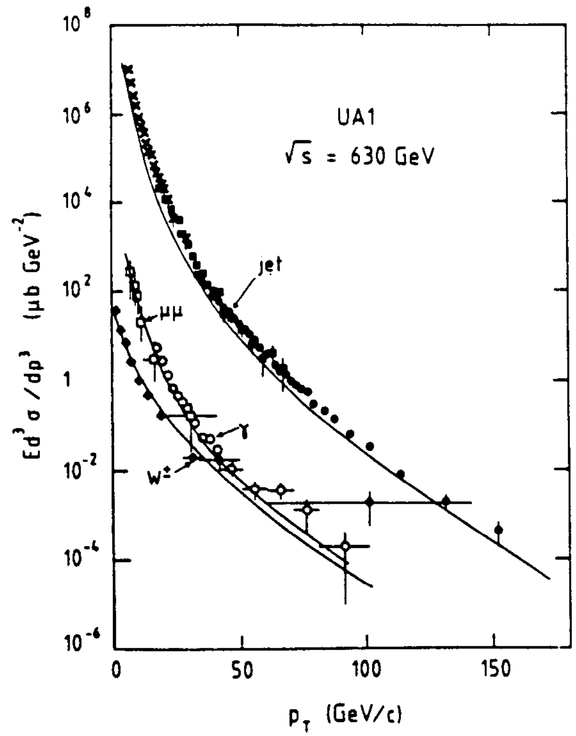

Figure 61: The processes used for QCD tests at the $\bar{p}p$ collider: jet production, direct photon production and heavy boson production.

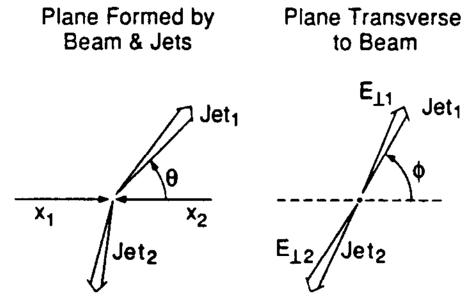

Figure 62: Schematic presentation of the two event planes of 2-jet events: the plane containing the jets and the incoming beams (left) and the plane perpendicular to the beam direction (right).

4.3 Large $p_\perp$ jet production

4.3.1 Kinematics and jet algorithm

In hadron-hadron collisions the center of mass of the parton-parton scattering is boosted with respect to the center of mass of the incoming hadrons. It is useful to describe the final state in variables that transform simply under longitudinal boost. Such variables are (Fig. 62)

$$\begin{array}{ll} \text{transverse momentum } p_\perp, & \\ \text{rapidity } y = \dfrac{1}{2}\ln\dfrac{E+p_{\|}}{E-p_{\|}}, & (p_{\|} \text{ momentum } \| \text{ to beam}) \\ \text{azimuthal angle } \phi. & \end{array}$$

$p_\perp$, Δy and ϕ are constant under boost along the beam. If only two partons (jets) are produced then these partons will be back-to-back in azimuth and balanced in transverse momentum[2]. There are simple relations between the variables in the laboratory system and the cm system.

$$\begin{array}{rclrcl} y_0 & = & \dfrac{y_3+y_4}{2} & y^* & = & \dfrac{y_3-y_4}{2} \\ x_1 & = & x_\perp e^{y_0}\cosh(y^*) & x_1x_2s & \simeq & \hat{s} = (2p_\perp\cosh(y^*))^2 \\ x_2 & = & x_\perp e^{-y_0}\cosh(y^*) & \cos\theta^* & = & \tanh(y^*) \\ & & x_\perp = \dfrac{2p_\perp}{\sqrt{\hat{s}}} & M_{jj}^2 & = & \hat{s} \end{array}$$

There y_0 is the laboratory rapidity or boost of the two parton system and y^* is the cms rapidity of either of the final state partons. The subprocess cms scattering angle Θ^* depends only on the difference of the rapidities of these partons.

[2]The small intrinsic transverse momentum of the incoming partons is neglected.

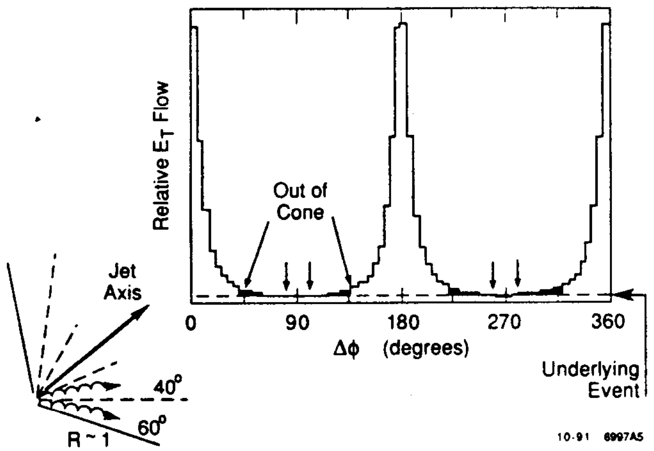

Figure 63: The transverse energy flow in two jet events as function of the distance ϕ from the jet axis. The energy 'out of cone' and the regions for measuring the amount of 'underlying event' are indicated.

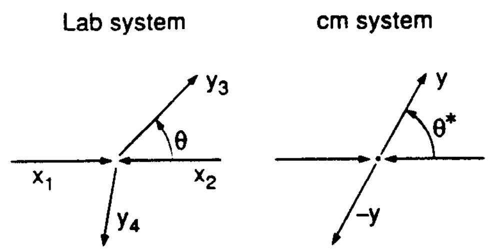

In practice the rapidity is replaced by the pseudo-rapidity $\eta = -\ln\tan\frac{\theta}{2}$, which coincides with the rapidity in the $m \to 0$ limit. $p_\perp$ is often replaced by the transverse energy $E_\perp$.

A commonly used definition of a jet is a cluster of transverse energy $E_\perp$ in a cone of size

$$R = \sqrt{(\Delta y)^2 + (\Delta\phi)^2}.$$

Typical values applied are $R = 0.7 \ldots 1$. Jets may be formed by combining calorimeter cells or charged tracks. The jet energy is the scalar sum of all energies within the cone; the rapidity (azimuth) of the jet axis is calculated as energy weighted sum of the rapidity (azimuth) of individual cells.

Fig. 63 shows the average transverse energy profile for jets as a function of the azimuth ϕ (30 GeV trigger threshold). For this plot the azimuth is measured relative to the axis of the higher $E_\perp$ jet. The jets have a well defined narrow cone, but the total energy of the jet is distributed over a broad angular range. There is also a background of uncorrelated energy flow. This 'underlying event' is understood as the result of multiple parton-parton interactions [96, 97]. The multiplicity per rapidity intervall of the underlying event is typically twice the multiplicty of a 'normal' event (= minimum bias event, no requirement on the $E_\perp$ trigger threshold). The experiments refine the jet energy measurement by subtracting the underlying event, correcting for the energy 'out of the cone' and/or optimizing the cone size. Fluctuations in the jet fragmentation and in the underlying event are the limiting factors in the jet energy resolution. For comparison with theory it should be noted that the smaller the cone size is chosen the more sensitive the measurements are to radiation of gluons, *i.e.*, higher order QCD terms.

4.3.2 Two jet cross section

The two jet cross section is the sum of parton cross sections due to incoming partons (i,j) and outgoing partons (k,l).

$$\begin{aligned} \frac{d^3\sigma}{dy_3 dy_4 dp_\perp^2} &= \frac{1}{16\pi s^2} \sum_{i,j}\sum_{k,l} \frac{f_i(x_1,Q^2)}{x_1}\frac{f_j(x_2,Q^2)}{x_2} \cdot \\ & \qquad \bar{\sum} \mid M(ij \to kl) \mid^2 \frac{1}{1+\delta_{kl}} \cdot \end{aligned} \quad (41)$$

y_3 and y_4 represent the laboratory rapidities of the outgoing partons. Given the parton densities from deep inelastic scattering this is now an absolute prediction with no free parameter. Expressions for the leading matrix element squared $\bar{\sum} \mid M \mid^2$ averaged over initial and final state spins and colours are given in Ref. [98]. The tree level diagrams are depicted in Fig. 64. The most important contributions are due to diagrams including the exchange of a gluon in the t-channel. The quantities that are useful to compare with theory are the inclusive jet cross section, the two-jet angular distribution and the two-jet mass distribution.

Inclusive jet cross section. Fig. 65a shows the inclusive jet $E_\perp$ distribution in $\bar{p}p$ collisions at $\sqrt{s} = 630$ GeV from the UA2 experiment [99]. The leading order $(\mathcal{O}(\alpha_s^2))$ QCD prediction using the EHLQ [100] structure functions are in excellent agreement with the data for central values of η. Note that the cross section at the low $p_\perp$ end is due to gluon-gluon interactions whereas the high end is due to $q\bar{q}$ scattering. These data constitute therefore a proof of the gluon self-coupling. In earlier data, see Fig. 61, the dominant experimental error was due to the jet energy resolution, which introduced typically an uncertainty of 50% on the steeply falling $p_\perp$ spectrum. A large effort has been made to keep calorimeter calibrations under control. For the most recent data by UA2 and

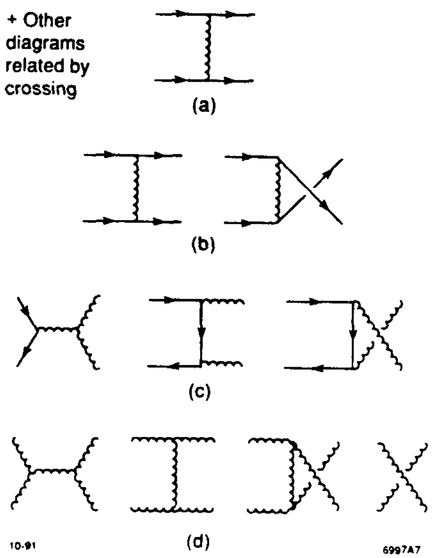

Figure 64: Tree-level diagrams for 2-jet production.

CDF jet energy errors are negligible compared to the error introduced by the underlying event ($\sim$ 10%, $p_\perp$-dependent) and the fluctuations in fragmentation ($\sim$ 30%, $p_\perp$-independent). Theoretical errors are roughly $p_\perp$-independent and are due to missing higher orders ($\sim$ 10%) and the scale uncertainty. The uncertainty due to different structure function sets is of the same order as the experimental error, Fig. 66a.

The agreement between data and theory becomes marginal at increasing values of η (Fig. 65b), reaching differences of almost a factor two in the forward bin $1.6 <| \eta |< 2.0$. No systematic effect has been identified in the data which could explain a possible underestimate of the cross section.

Search for compositeness. If light quarks are composite then the scattering amplitude includes a four-fermion point-like interaction [101], which would manifest itself well below the characteristic energy scale Λ_C describing the strength of the new interaction that binds the substructure in the quarks. Finite values of Λ_C produce an excess of events at large $p_\perp$ with respect to the standard QCD prediction, which corresponds to $\Lambda_C = \infty$. For the comparison of the data with the expected behaviour for various values of Λ_C (Fig. 66b) only the central η bin was used [99]. The calculations have been normalized in the low-$p_\perp$ range where pure QCD is expected to dominate. The 95% confidence lower limit on Λ_C corresponds to 845 GeV.

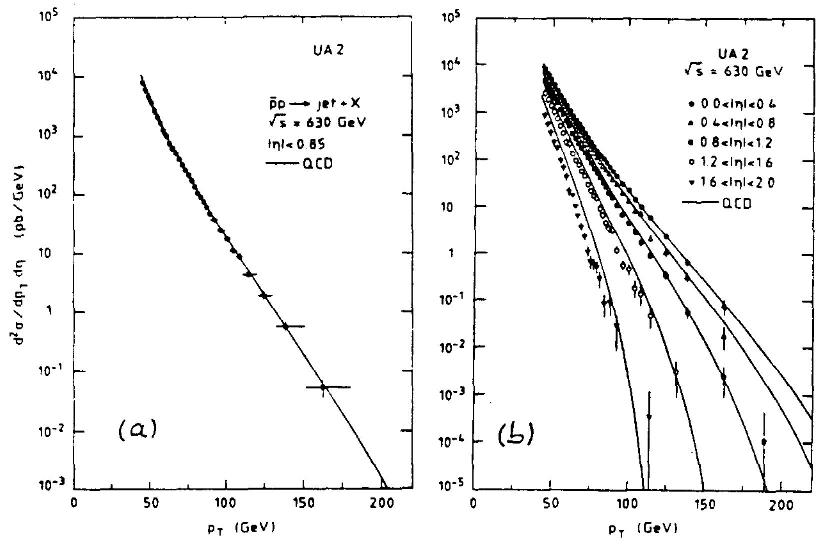

Figure 65: Inclusive jet cross section for the central region (left) and for different bins in rapidity η (right). The systematic error of the data of $\pm 32\%$ is not shown. The curves represent $\mathcal{O}(\alpha_s^2)$ QCD predictions with $Q^2 = (p_\perp/2)^2$ and EHLQ structure functions [99].

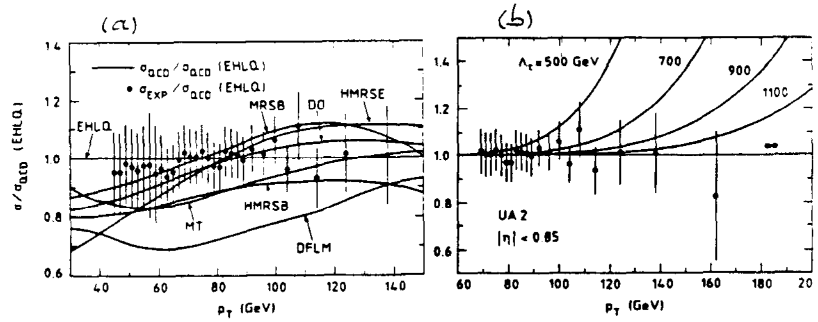

Figure 66: (a) The ratio between the inclusive jet cross section and a QCD calculation using EHLQ structure functions. The curves represent calculations for different structure function sets, relative to the EHLQ set. (b) Similar to (a) for the EHLQ set and including a contact term Λ_C. The behaviour for finit values of Λ_C, again relative to the QCD prediction, are shown as solid curves [99].

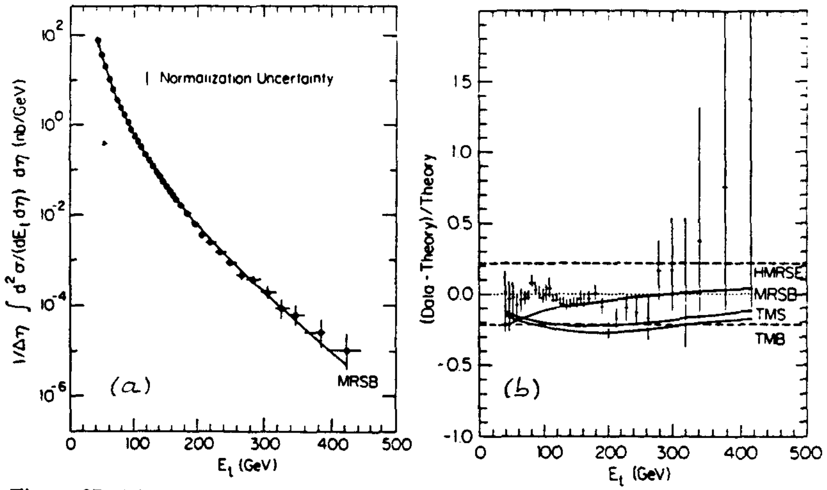

Figure 67: (a) Inclusive jet cross section (CDF) for the central region and for a cone size $R = 0.7$. The curves represent NLO QCD predictions [102]. The overall normalization error is also indicated. (b) The ratio between the inclusive jet cross section and a QCD calculation using MRSB structure functions. The curves represent calculations for different structure function sets, relative to the MRSB set. The horizontal dashed lines indicate the $E_\perp$ independent systematic uncertainty of the data [104].

Next-to-leading order calculations are available [102, 103], which allow a more precise treatment of effects due to the finite jet cone size. The CDF collaboration finds the best description of their $p_\perp$ spectrum for centrally produced jets for a cone of size R = 0.7. Fig. 67a shows the $E_\perp$ spectrum that extends up to $E_\perp \sim 400$ GeV due to the higher cms energy of $\sqrt{s} = 1.8$ TeV. The CDF collaboration studies the dependence of the inclusive jet cross section on the cone size for jet energies $E_\perp \sim 100$ GeV, Fig. 68. Data and theory show the same trend, namely an increase of jet rate with increasing cone size. These data may allow to discriminate between different scale choices, where the scale favoured by the data is $Q \sim E_\perp/4$.

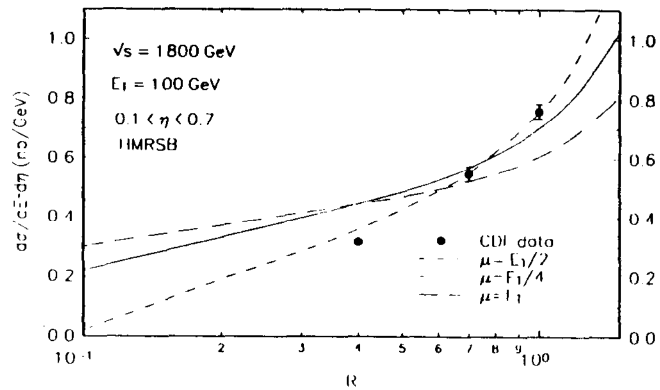

Figure 68: The variation of the jet cross section with the size of the jet cone R for jets of $E_\perp \sim 100$ GeV. The curves represent NLO QCD predictions for different choices of the renormalization scale μ [104].

4.3.3 Two-jet angular distribution

For sufficiently large angular acceptance the elastic subprocesses $gg \to gg$, $qg \to qg$ and $q\bar{q} \to q\bar{q}$ dominate. These processes proceed via single gluon exchange and show therefore very similar dependence on the cms scattering angle Θ^*, namely a $1/(1-\cos\Theta^*)^{-2}$ behaviour, characteristic for the exchange of a vector boson in the t-channel,

$$\frac{d\hat{\sigma}}{d\cos\Theta^*} \sim \frac{1}{(1-\cos\Theta^*)^2}.$$

Fig. 69 shows the $\cos\Theta^*$ dependence of the $qg \to qg$ and $q\bar{q} \to q\bar{q}$ subprocesses normalised to $gg \to gg$ [4]. These ratios are rather constant at the values determined by the colour factors, which allows useful simplifications in the theoretical treatment of two-jet cross sections [105].

It is convenient to plot the data in terms of the variable χ, which removes the $(1-\cos\Theta^*)$ singularity

$$\chi = \frac{1+\cos\Theta^*}{1-\cos\Theta^*}.$$

Fig. 70 shows the χ distribution for events with $\sqrt{\hat{s}} = m_{2jet} = 240\ldots300\ GeV$ [3]. The solid curve depicts the LO QCD prediction including both, scale breaking effects in the structure functions and the Q^2 dependence of α_s. The χ distribution would be flat if these effects would be neglected. The data rule out completely a scalar gluon which exhibits a much steeper dependence on χ.

The χ distribution is sensitive to a contact term and provides a test on compositeness which is independent of the test discussed in the previous section. The contact interaction leads to an excess at wide angle ($\chi \simeq 1$), relative to the QCD prediction, as shown by the broken curve. The data give $\Lambda_C > 415\ GeV$ at 95% CL [3].

4.3.4 Two-jet mass distribution

New mass states may be detected in the two-jet mass distribution. Fig. 71 shows the fractional contributions of the dominant subprocesses as a function of the two jet mass. At fixed two-jet mass the relative contributions are nearly independent of the cms scattering angle. Varying the two-jet mass from low values to high values changes the composition of the contributing subprocesses from gluon-gluon dominance to quark-antiquark dominance. CDF has tested the two-jet mass distribution for two different cone sizes. Fig. 72 shows the data overlayed with the LO theoretical predictions that are convoluted with the experimental calorimeter resolution. The two curves describe the band of theoretical uncertainty due to different sets of stucture functions and the (small) scale dependence for $0.5p_\perp^2 < Q^2 < 2p_\perp^2$. The data indicate a preference for cone size R = 1, whereas the inclusive jet $E_\perp$ distribution was best described with R = 0.7. Next-to-leading order predictions fit the data only slightly better when the normalization is left free [104].

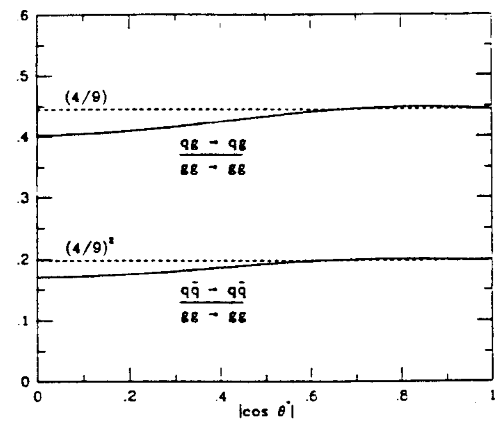

Figure 69: Quark-antiquark and quark-gluon angular distributions normalized to the distribution for $gg \to gg$ [4].

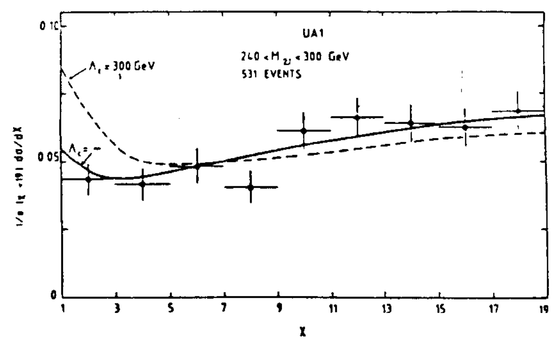

Figure 70: χ distribution for events with $240 < m_{jj} < 300\ GeV$ measured by UA1 compared with LO QCD predictions. The effect of a contact term is also indicated [3].

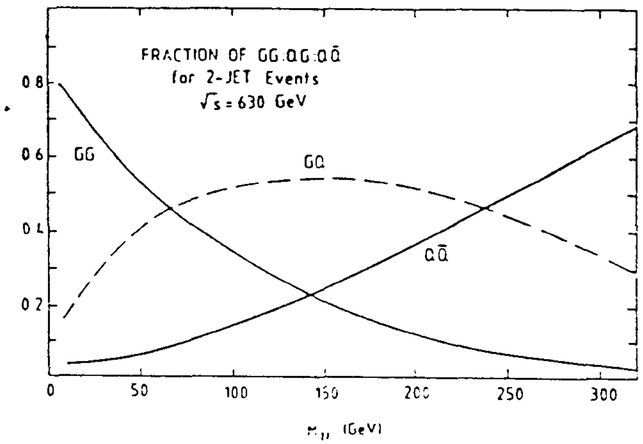

Figure 71: The fractional contribution of the various parton-parton subprocesses to the 2-jet cross section as a function of the 2-jet mass [3].

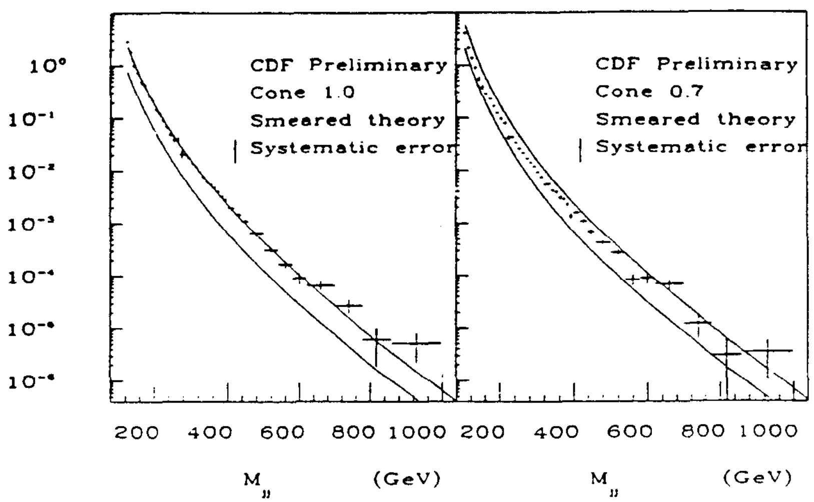

Figure 72: Dijet mass spectra in the central region $|\eta| < 0.7$ for two choices of cone size (R=0.7, 1.0). The band of curves represents the LO QCD calculations for different structure function sets and varying Q^2 in the range $0.5p_\perp^2 < Q^2 < 2p_\perp^2$ [104].

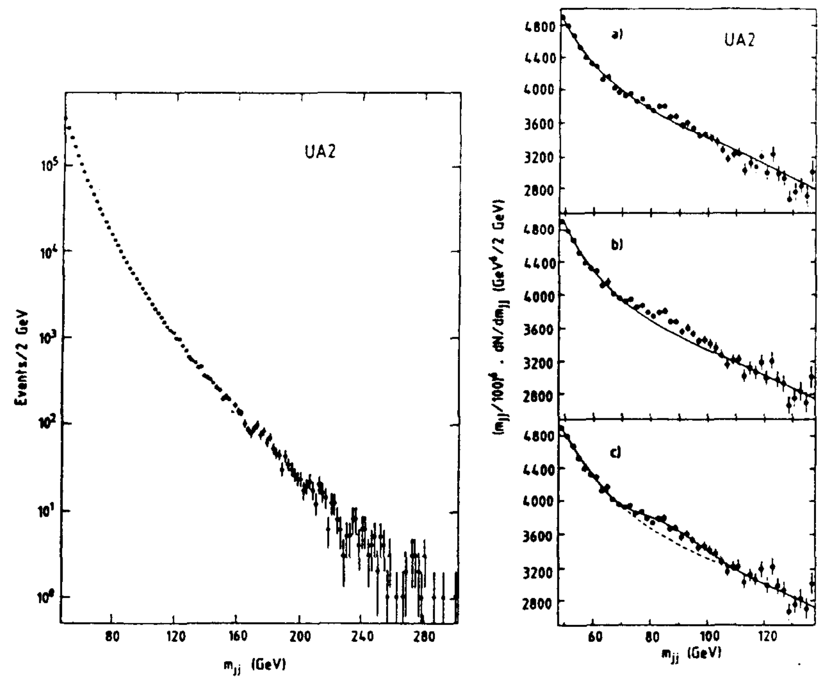

Figure 73: (A) The 2-jet mass spectrum for a jet cone size R=0.64 (left). (B) The 2-jet mass spectrum in the region around the expected W,Z° signal. Three different fits (a, b, c) have been overlayed on the data as explained in the text [106] (right).

Jet spectroscopy. It is interesting to assess the problems of finding a heavy mass state through its decay to jets by performing the search for the known states W and Z°. The W/Z mass peak has to be observed as a departure from the smooth two-jet mass spectrum of QCD processes. Fig. 73 shows the two-jet mass spectrum as measured by UA2 [106]. The cone size of $R = 0.64$ was optimized for best mass resolution ($\sim 10\%$) uniform over the full mass range. A smooth fit was performed over the mass range, 48...300 GeV. The bad quality of this fit (Fig. 73a), $\chi^2/NdF = 163/124$, is mainly due to points in the W/Z mass region. Excluding the mass range 70...100 GeV improves the fit to $\chi^2/NdF = 97.5/109$, (Fig. 73b). A significant result for the signal (4.2 s.d.) is found only when the mass ratio M_Z/M_W is set to the measured value of 1.13 and, most importantly, the mass resolution, which is known to better than 21.5%, is fixed to its value of 10 GeV (Fig. 73c).

A search for additional heavy vector bosons W' decaying to two jet final states was carried out. Despite the good mass resolution such a state was excluded only in the modest range of 101 $GeV < m_{jj} < 158$ GeV. The study demonstrates the feasibility of jet spectroscopy and also the limiting factors: the two-jet mass resolution, the precise knowledge of this resolution and the available statistics.

4.3.5 Three-jet cross section

At future hadron colliders multijet production will be dominant. There is therefore a strong motivation to understand jet production beyond two-jet production. For the case of three jet events theoretical calculations exist in leading order. At fixed cms energy $\sqrt{s}$ the final state parton configuration is specified by five independent variables exactly as in e^+e^- collisions (section 3.3),

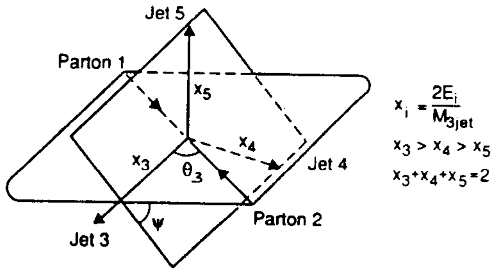

x_3, x_4	sharing of energy between the final state partons,
Θ_3, ψ	orientation of the three-jet system,
ϕ	overall orientation.

ψ is the angle between the plane containing jet-4 and jet-5 and the plane containing jet-3 and the beam axis.

The subprocess differential cross section may be written

$$\frac{d^4\hat{\sigma}}{dx_3 dx_4 d\cos\Theta_3 d\psi} = \frac{1}{(32\pi^2)^2}\bar{\sum} \mid M \mid^2,$$

where the subprocess matrix elements have been calculated in [107]. The three-jet Dalitz-plot x_3 versus x_4 measured by CDF is shown in Fig. 74. The selection criteria assure that the jets are well identified ($E_\perp > 15$ GeV, $\mid \eta_{jet} \mid < 3.5$, $\mid \cos\Theta_3 \mid < 0.6$) and well separated from each other ($\Delta R > 0.85$, $30° < \psi < 150°$). For these cuts the acceptance is flat over the Dalitz plot within 7%. The distribution is limited at small x_4 by the requirement of energy ordering $x_3 > x_4 > x_5$, and at large x_4 by energy conservation $x_3 + x_4 + x_5 = 2$. The enhancement at large x_3, large x_4 is due to the softness of the radiated jet-5. Fig. 75 shows the projections for the fastest (x_3) and second fastest jet (x_4) together with the expectation for phase space (flat distribution), for full QCD and for QCD where only the quarks in the incoming hadrons contribute. QCD makes the pure $\bar{q}q$ interactions more phasespace-like. The $cos\Theta_3$ distribution, Fig. 75d, exhibits the steep rise at $cos\Theta_3 \to 1$ expected from vector exchange in the t-channel. The distribution of the angle ψ, Fig. 75c, is peaked in forward and backward direction due to radiation from either of the scattered partons.

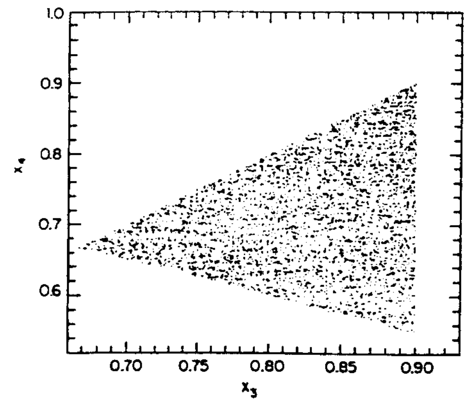

Figure 74: Dalitz plot of the scaled energies x_3, x_4 for 3-jet events (CDF).

In e^+e^- annihilation three jet events are the key to extract α_s. In hadron-hadron collisions a similar method could provide α_s at different parton center-of-mass energies $\sqrt{\hat{s}}$ ranging from 50 GeV to nearly 1 TeV. This would be an extremely interesting test for the running of α_s. Early attempts to determine α_s from the relative rate of 3-jet and two-jet production [3] were very frustrating due to the complete lack of theoretical knowledge of the next-to-leading order corrections to the three-jet rate. UA1 and UA2 used a K-factor ratio (K_3/K_2) to describe the unknown effect of higher orders. The average values of $\alpha_s(K_3/K_2)$ that were measured are 0.22 ± 0.05 (UA1) and 0.23 ± 0.04 (UA2). Since existing α_s measurements give values of $\alpha_s \sim 0.12$, higher order QCD corrections do have an important influence on the three-jet to two-jet ratio. With the better QCD calculations available nowadays, it may be interesting to attempt this analysis again.

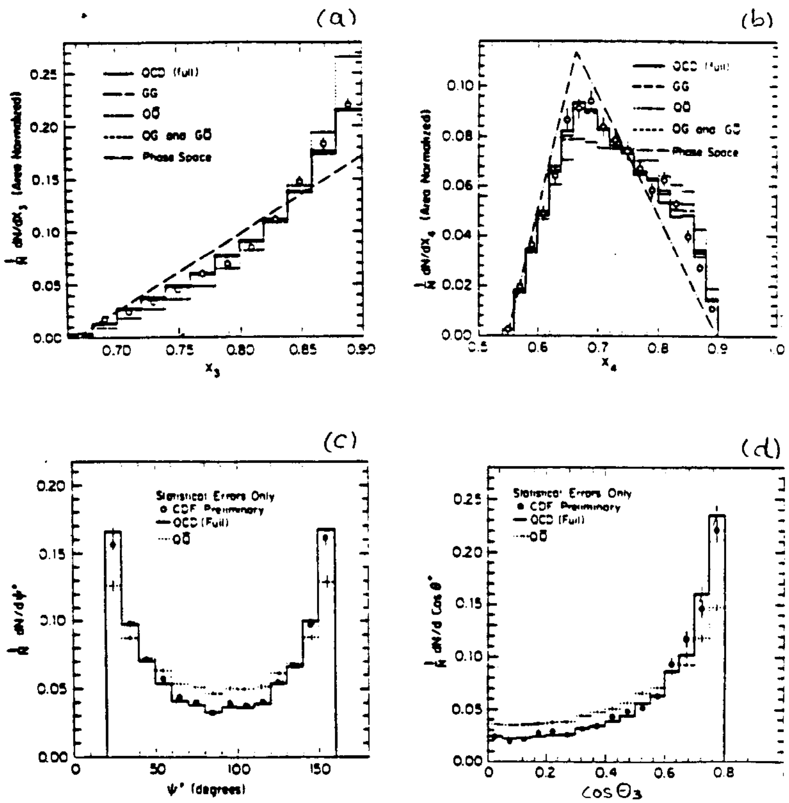

Figure 75: The distribution of the variables for 3-jet events: scaled energies x_3, x_4 and the angles ψ^* and $\cos\Theta^*$. Shown are also the expectation from LO QCD (solid line), from phase space (dashed line) and for $\bar{q}q$ initial states contributing only (dotted line) [104].

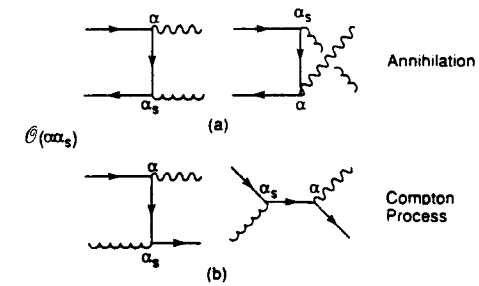

Figure 76: $\mathcal{O}(\alpha_s\alpha)$ diagrams of direct photon production.

4.4 Direct photon production

Production of high transverse momentum photons and jet production are closely related processes. The leading order subprocesses are shown in Fig. 76: Annihilation that dominates in $\bar{p}p$ collisions at high $p_\perp$, and the Compton process that dominates in pp collisions at medium $p_\perp$. Direct photon production has several advantages over jet production. There is only one QCD vertex at the tree level and therefore fewer diagrams to be calculated. Next-to-leading order calculations are available [108, 109]. Since photons do not fragment there is no uncertainty due to hadronization. The energy resolution of the electromagnetic calorimeter is much better for γ's than for hadrons and systematic uncertainties on the photon energy are smaller. The disadvantages are the low rate for production, see Fig. 61, $\sigma_\gamma/\sigma_{jet} \sim 10^{-4}$, and the high background from π^0's and η's produced in jets. To reduce this background the experiments require an isolated cluster of electromagnetic energy with no charged track pointing at it. Even then photon identification is possible only on a statistical basis either by using the conversion probability in the converter of a preshower detector [110] or the transverse shower profile measurement from a strip detector imbedded into the calorimeter [111].

The differential cross section in leading order is

$$\frac{d^3\sigma}{dy_\gamma\, dy_{jet}\, dp_\perp^2} = \frac{1}{16\pi s^2}\sum_{i,j}\sum_l \frac{f_i(x_1,Q^2)}{x_1}\cdot\frac{f_j(x_2,Q^2)}{x_2}\sum | M_{ij}\to\gamma l\,|^2 .$$

The matrix elements squared corresponding to the annihilation process and the Compton process are given *e.g.*, in Ref. [3]. As higher order corrections have been calculated, the scale dependence can be analysed. Aurenche et al. [108] find a very small optimized scale, $\mu_{PAC} = p_\perp^2/20$.

Fig. 77a shows the inclusive direct photon spectrum as measured by UA2 and compared to the $\mathcal{O}(\alpha_s^2\alpha)$ prediction. Fig. 77b shows the measurements by CDF. The agreement of data and theory is very good for $p_\perp > 20\ GeV$. At lower $p_\perp$ values the measured rates are above the predicted rate, possibly due to final state bremsstrahlung not yet included in the $\mathcal{O}(\alpha_s^2\alpha)$ predictions. More details of the

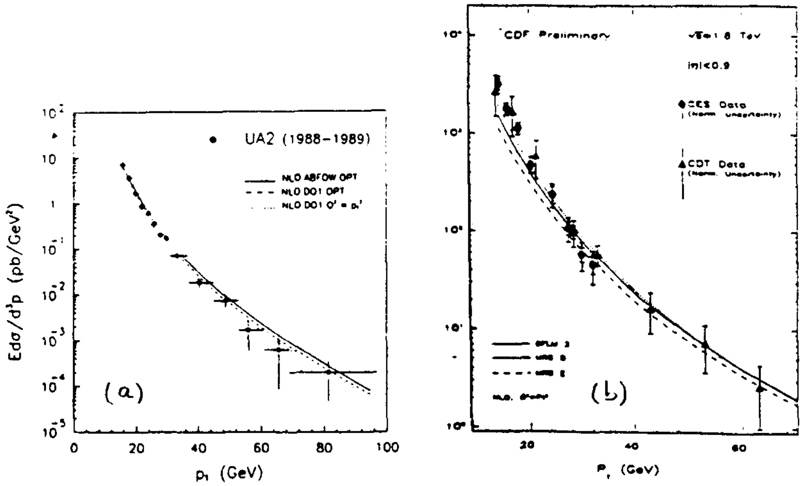

Figure 77: The invariant differential cross section for direct photon production measured by UA2 [110] (left) and CDF [111] (right) compared to NLO QCD predictions.

events could be studied. CDF has already shown the cms angular distribution [104]; other subjects of interest are the γ-jet mass distribution and the relative rate of one-and two-jet events associated with an isolated photon.

4.5 Transverse momentum distribution of the weak bosons W, Z°

The vectorbosons W, Z° produced in $\bar{p}p$ collisions are in about 15% of the events accompanied by an additional jet. The contributing tree level diagrams are shown in Fig. 78. At low values of $p_t^{W,Z}$ where multiple soft gluon emission is expected

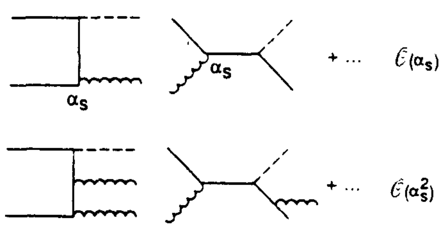

Figure 78: LO and NLO diagrams contributiong to W/Z° events and jets.

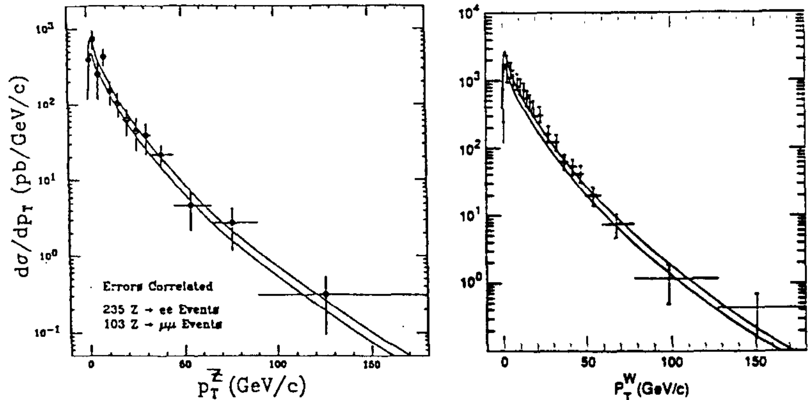

Figure 79: The differential cross section for Z° and W production measured by CDF. The NLO QCD prediction is shown as a band, where the width of the band represents the theoretical uncertainty.

to dominate, the W, Z° cross section is calculated using soft gluon resummation techniques [112]. In the high-$p_\perp$ regime, $p_t^{W,Z} > 20 GeV$, the cross section is expected to be well described by perturbative QCD and complete $\mathcal{O}(\alpha_s^2)$ calculations are available [113, 114]. The $p_\perp$ dependence of the W, Z° cross section provides a more sensitive test of QCD than the total cross section. Good understanding of the $p_t^{W,Z}$ measurement is needed at large $p_\perp$ wheredeviations from the theoretical prediction may indicate new physics. There the events are characterized by large missing energy or large $p_\perp$ leptons, both typical signs for new physics. Good understanding of the p_t^W measurement is also essential for the precise measurement of the W mass.

W and Z° are detected through their leptonic decay modes, $W \rightarrow l\nu$ and $Z^0 \rightarrow l^+l^-$, where the lepton is μ or electron. Fig. 79a shows the $p_\perp^Z$ distribution from CDF; 2% of the events have $p_\perp > 50\ GeV$. The experimental error on the $p_\perp$ scale is very small, $\sigma(p_\perp) = 1.5 \ldots 4\ GeV/c$. Statistical errors dominate the high $p_\perp$ part, $p_\perp > 20\ GeV/c$, which makes an α_s determination not yet interesting.

The measurement of the $p_\perp$ distribution of the W boson is more complicated than for the Z° due to the undetected neutrino and the underlying event. Fig. 80a shows the p_t^W distribution measured by UA2 [115]. Though the rate of events at $p_t^W \sim 4\ GeV$ is very sensitive to Λ_{QCD}, the same $p_\perp$ region is also mostly affected by the measurement uncertainties due to the calorimeter response and the underlying event. These uncertainties are much smaller for $p_t^W > 25\ GeV$ shown in Fig. 80b, which is also the $p_\perp$ range sensitive to W from the top decay $t \rightarrow Wb$, where t is produced in $\bar{p}p \rightarrow \bar{t}tX$. However for the statistics available to UA2, the predicted signal is well below the sensitivity of the data.

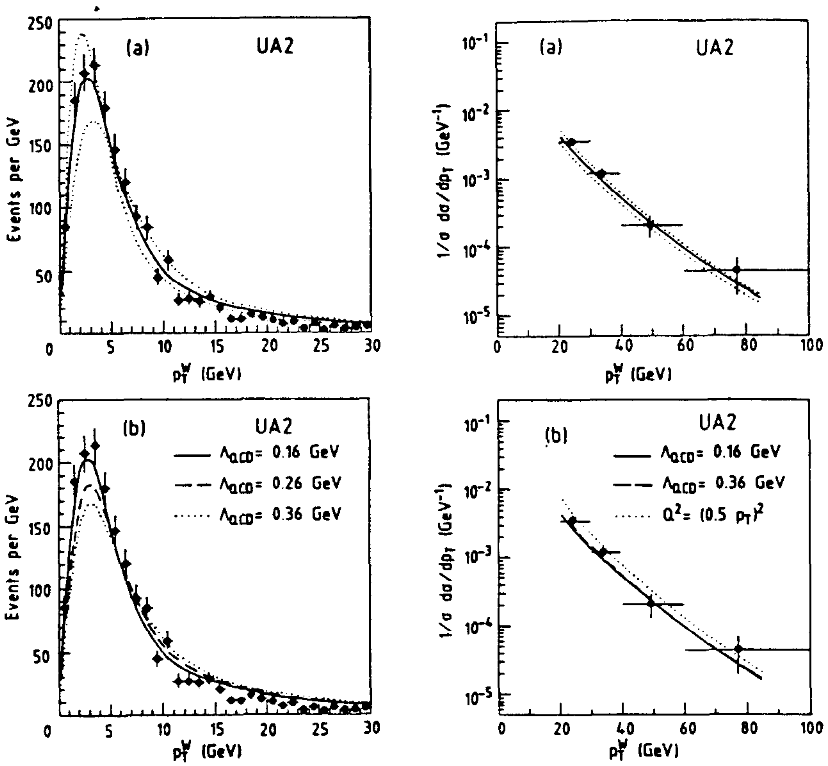

Figure 80: The observed $p_\perp^W$ distribution for $p_\perp < 30\ GeV$ (left) and $p_\perp > 25\ GeV$ (right). The curves show QCD predictions with (a) the allowed variations in detector response and (b) for different values of $\Lambda_{\overline{MS}}$ [115].

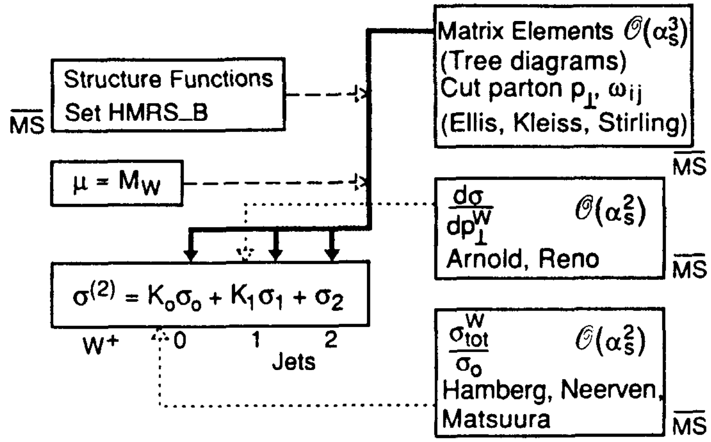

Figure 81: Schematic layout of the α_s determination from W and jets by UA2.

4.5.1 α_s from W and jets

UA2 used the high $p_\perp^W$ data to determine α_s [116]. This is the only measurement of α_s from $\bar{p}p$ collisions. Naïvely the ratio R_{exp},

$$R_{exp}(\alpha_s) = \frac{\text{number of W + 1-jet events}}{\text{number of W + 0-jet events}}$$

is equal to α_s. In practice this ratio is strongly modified due to higher order corrections, the $p_\perp^W$ cut and the cuts applied to select well identified jets ($E_\perp^{jet} > 20GeV$, $|\ \eta_{jet}\ | < 1.6$). The measured value is

$$R_{exp} = (3.91 \pm 0.40) \times 10^{-2}.$$

The method of determining α_s consists in comparing the measured R_{exp} and the value $R_{MC}(\alpha_s)$ determined from Monte Carlo and adjusting α_s such that $R_{exp} = R_{MC}$. We will describe this method because it combines the knowledge we accumulated in these three lectures and demonstrates that an experimentalist has not to give up when the matrix elements are not available to the required order.

The method is layed out in Fig. 81. The matrix elements at tree level up to $\mathcal{O}(\alpha_s^3)$ [117] are implemented in a Monte Carlo to generate W + 0,1,2 partons. Cutoffs are needed to avoid divergencies:

$$\begin{aligned} p_\perp^{parton} &> p_\perp^{min} \quad (= 12\ GeV), \\ \omega_{ij} &> \omega^{min} \quad (= 20^\circ, \text{ angle between parton i and j}). \end{aligned}$$

The size of the contributions missing due to these cutoffs is described by K-factors. The cross section at $\mathcal{O}(\alpha_s^2)$ is then

$$\sigma^{[2]} = K_0\sigma_0 + K_1\sigma_1 + \sigma_2,$$

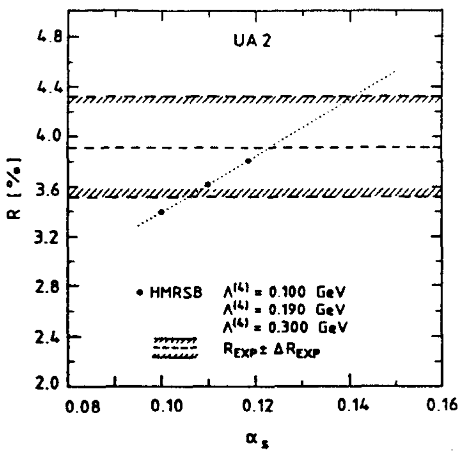

Figure 82: $R_{MC}(\alpha_s)$ compared to the experimental measurement R_{exp}. The QCD predictions R_{MC} were calculated using three different values of α_s with the corresponding HMRSB structure function parametrizations [116].

where σ_i is the cross section for W + i jets. The K-factors K_0 and K_1 are determined using two other theoretical calculations that are available to $\mathcal{O}(\alpha_s^2)$: the differential cross section $d\sigma/dp_\perp^W$ [113] and the total cross section σ_{tot}^W/σ_0 [118]. To compare the parton cross sections σ_i to the experimental cross sections, the cross sections σ_{ij} for generating i partons and measuring j jets have to be determined by simulating jet fragmentation and detector response. The measured ratio is then

$$R_{MC}(\alpha_s^{MC}) = \frac{\sigma_{01}K_0 + \sigma_{11}K_1 + \sigma_{21}}{\sigma_{00}K_0 + \sigma_{10}K_1 + \sigma_{20}}.$$

Input to the calculation of the cross sections σ_i are the structure functions and the renormalization scale. Note that with each change of the value of α_s the fit of the structure functions has to be redone. It has to be ensured that all calculations are done consistently within the same renormalization scheme $\overline{MS}$. Fig. 82 shows the three calculated points R_{MC} as function of α_s and the measured value R_{exp}. The result for α_s is

$$\alpha_s(M_W^2) = 0.123 \pm 0.018\,(stat) \pm 0.017\,(syst).$$

α_s changes by $\Delta\alpha_s = -0.010$ when the renormalization scale is changed from $\mu = M_W/2$ to $\mu = M_W$.

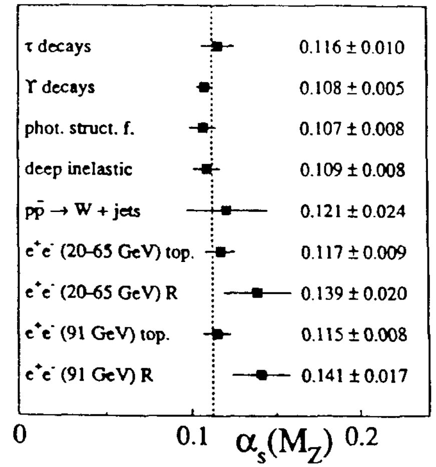

Figure 83: α_s values as measured in different reactions [54].

5 Summary and conclusions

A large number of tests of QCD have been performed in deep inelastic scattering, e^+e^- annihilation and hard hadron-hadron collisions. Discrepancies have been clarified in the last years by more precise measurements. The pieces of the QCD puzzle fit together and form a very consistent picture:

- Consistent values for the strong coupling α_s are found; they are summarized in Fig. 83. The running of α_s, as predicted by QCD is confirmed by the measured $\sqrt{s}$ dependence of the 3-jet fraction.
- Various distributions for 3-jet and 4-jet events in e^+e^- annihilation and 2-jet angular distributions in $\bar{p}p$ hard scattering processes rule out models with scalar gluons or models without gluon self interaction.
- The distributions at the hadron level are well reproduced by Monte Carlo programs that use string and cluster fragmentation or by analytical calculations.

There is no evidence for any 'failure' of QCD in reproducing the data. The precision with which α_s can be measured is at present limited by the theoretical uncertainty due to the renormalization scale dependence and the factorization scale dependence, both in e^+e^- annihilation and in deep inelastic scattering.

Acknowledgements

I warmly thank D. Leith and D. Burke for inviting me to give these lectures. Part of the lectures were prepared when I participated as a guest of the Max Planck Institut, München (Germany), in the work of the ALEPH group. The lectures were written down during a visitorship granted by CNRS-IN2P3 (France) at the University Paris 6. I am grateful to R. Settles and B. Grossetete for providing these visitorships and I thank the groups for their generous hospitality. The SLAC publications office has provided many of the figures; their careful work is very much appreciated.

It is a pleasure to thank H. Kühn and P. Zerwas for their clarifying discussions in preparing the lectures. I want to thank many of my colleagues for sharing their experience and ideas and for making their data available. Special thanks go to G. Cowan, T. Lohse, M. Schmelling (ALEPH); W. DeBoer, K. Hamacher (DELPHI); T. Hebbeker (L3); S. Bethke (OPAL); M. Virchaux, R. Voss (BCDMS); J. Huth, P. James (CDF); F. Pauss (UA1) and K. Jakobs (UA2).

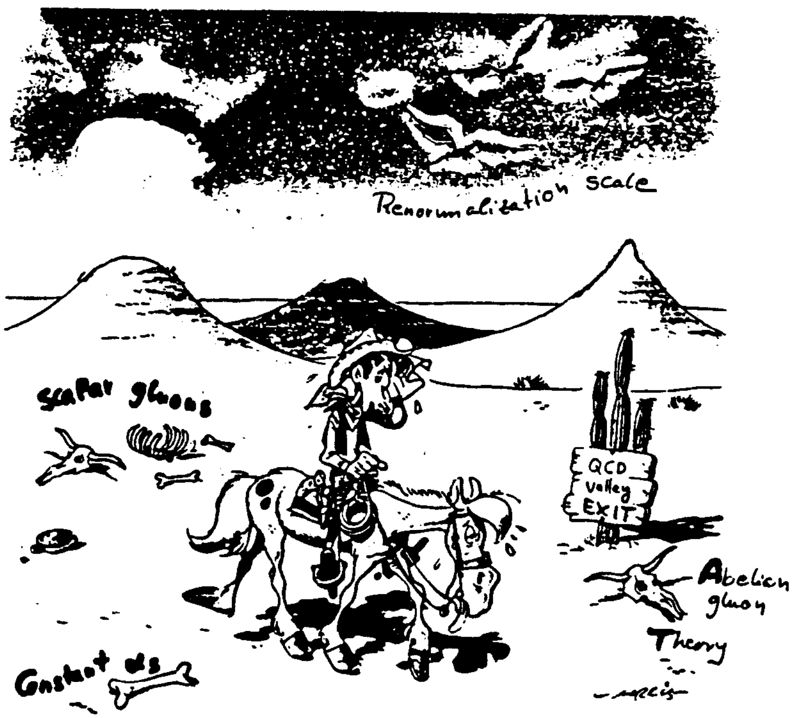

A Minimal subtraction renormalization schemes

Most calculations in fixed order QCD perturbation theory are performed in the 'modified minimal subtraction' scheme. In this approach, ultraviolet loop divergencies are regulated by reducing the space-time dimensions to $N < 4$,

$$\frac{d^4 k}{(2\pi)^4} \to \frac{d^{4-2\epsilon} k}{(2\pi)^{4-2\epsilon}} (\mu)^{2\epsilon}, \qquad \text{where} \quad \epsilon = 2 - \frac{N}{2}.$$

Note that the renormalization scale μ preserves the dimensions of the couplings and fields. The 'ln M' poles in loop integrals (see section 1.1) then lead to $1/\epsilon$ poles. The 'minimal substraction' renormalization prescription (MS [119]) is: When calculating beyond leading order, substract off the $1/\epsilon$ poles and replace the bare coupling by the renormalized coupling $\alpha_s(\mu^2)$. The poles always appear in the combination

$$\frac{2}{\epsilon} - \gamma_E + \ln 4\pi, \qquad \text{where} \quad \gamma_E \text{ is Euler's constant.}$$

In the 'modified minimal substraction' scheme $\overline{MS}$ [120] this combination is substracted off instead. The Λ's in the two schemes are related by

$$\Lambda^2_{\overline{MS}} = \Lambda^2_{MS} \exp(\ln 4\pi - \gamma_E).$$

B Angular ordering in parton showers

An effect similar to the angular ordering in parton showers occurs in QED in electromagnetic showers [121]. Assume a soft γ to be radiated off one of the pair produced electrons. The radiation time in the ($e\gamma$)-center-of-mass system is $t_{rad}^{cms} \sim 1/m_{e\gamma}$. The radiation time in the lab system is (boost $\beta\gamma \approx \frac{k_e + k_\gamma}{m_{e\gamma}} \approx \frac{k_e}{m_{e\gamma}}$)

$$t_{rad} \sim \frac{1}{m_{e\gamma}} \cdot \frac{k_e}{m_{e\gamma}} \sim \frac{1}{k_\gamma \Theta^2_{e\gamma}} \sim \frac{\lambda_\perp}{\Theta^2_{e\gamma}},$$

where $\lambda_\perp$ is the transverse wavelength of the γ. During the time t_{rad} the e^+e^- pair separates by an amount $\rho_\perp \sim \Theta_{ee} t_{rad} \sim \lambda_\perp \frac{\Theta_{ee}}{\Theta_{e\gamma}}$. To avoid destructive interference of the oppositely charged γ sources e^+ and e^-, the transverse separation $\rho_\perp$ must be larger than the transverse γ wavelength $\lambda_\perp$,

$$\rho_\perp \sim \Theta_{ee} t_{rad} \sim \lambda_\perp \frac{\Theta_{ee}}{\Theta_{e\gamma}}.$$

So the inequality $\Theta_{ee} > \Theta_{e\gamma}$ must be fullfilled. When for large angles $\Theta_{e\gamma}$ the separation of the e^+e^- pair is smaller than $\lambda_\perp$, the photon cannot resolve the e^+e^- pair and probes only the total charge which is zero, and soft γ emission is strongly suppressed.

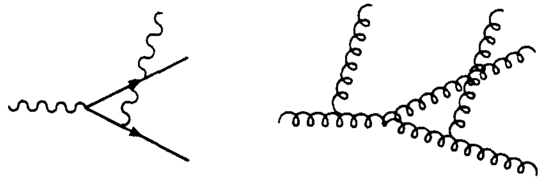

Figure 84: Radiation of a soft gamma or gluon.

Similar arguments hold for the radiation of soft gluons except that the coherent radiation by an unresolved pair of quarks or gluons is no longer zero, but the radiation acts as if it were emitted from the parent gluon. Therefore angular averaged observables are described correctly when subsequent emission angles are ordered.

References

[1] F. Halzen, A.D. Martin, 'Quarks & Leptons', John Wiley & Sons (1984).

[2] V.D. Barger, R.J.N. Phillips, 'Collider Physics', Frontiers in Physics, Addison-Wesley (1987).

[3] R.K. Ellis, W.G. Scott, in Proton-Antiproton Collider Physics, eds. G. Altarelli, L. DiLella, Advanced Series Directions in HEP, Vol.4, World Scientific, Singapore (1989).

[4] R.K. Ellis, W.J. Stirling, 'QCD and collider physics', FERMILAB-Conf-90/164-T (1990).

[5] R.D. Field, 'Applications of perturbative QCD', The Advanced Book Programm, Addison-Wesley (1989).

[6] Z. Kunszt, P. Nason in 'Z Physics at LEP1', eds. G. Altarelli, R. Kleiss, C. Verzegnassi, CERN Report CERN 89-08 (1989), Vol. 1, p.373.

[7] T. Sjöstrand in 'Z Physics at LEP1', eds. G. Altarelli, R. Kleiss, C. Verzegnassi, CERN Report CERN 89-08 (1989), Vol. 3, p.143.

[8] Proc. Workshop on 'Hadron structure functions and parton distributions', eds. D.F. Geesaman, J. Morfin, C. Sazama, W.K. Tung, FNAL, Batavia 1990, World Scientific, Singapore.

[9] B. Foster (ed.), 'Electron-Positron Annihilation Physics', Adam Hilger, Bristol, 1989.

[10] M. Aguilar-Benitez *et al.*, Phys. Lett. B239 (1990) IV.51.

[11] J.C. Collins, W.K. Tung, Nucl. Phys. B 278 (1986) 934.

[12] S. Drell, lectures presented in this Summer Institute.

[13] T. Sloan, G. Smadja, R. Voss, Phys. Rep. 162 (1988) 45.

[14] E665 collaboration, talk presented by H.E. Montgomery at this Summer Institute; E665 is the only experiment that has presented results on jet rates from DIS.

[15] CDHS Collaboration, H. Abramowicz *et al.*, Z. Phys. C15 (1982) 19.

[16] G. Altarelli, G. Parisi, Nucl. Phys. B 126 (1977) 298.

[17] G. Curci, W. Furmanski, R. Petronzio, Nucl. Phys. B 175 (1980) 27; W. Furmanski, R. Petronzio, Phys. Lett. B97 (1980) 437.

[18] R. Peccei, lectures presented at this Summer Institute.

[19] H. Plothow-Besch, 'Parton density functions', Proc. 3^{rd} Workshop on Detector and Event simulation in HEP, Amsterdam (1991), p.148.

[20] J.F. Gunion *et al.*, Phys. Rev. D29 (1984) 2491.

[21] J. Feltesse, lectures presented at this Summer Institute.

[22] F. Sciulli, lectures presented at this Summer Institute.

[23] L.W. Whitlow, Ph.D.Thesis, Stanford University, SLAC-Report 357 (1990).

[24] EM Collaboration, J.J. Aubert *et al.*, Nucl. Phys. B 259 (1985) 189.

[25] EM Collaboration, J.J. Aubert *et al.*, Nucl. Phys. B 293 (1987) 740.

[26] BCDMS Collaboration, A.C. Benvenuti *et al.*, Phys. Lett. B223 (1989) 485; Phys. Lett. B223 (1989) 490; Phys. Lett. B237 (1990) 592.

[27] A. Milsztajn, A. Staude, K.-M. Teichert, M. Virchaux, R. Voss, Z. Phys. C49 (1991) 527.

[28] NM Collaboration, D. Allasia *et al.*, Phys. Lett. B294 (1990) 366.

[29] M. Virchaux, A. Milsztajn, DPhPE 91-08 (1991), submitted to Phys. Lett. B.

[30] A.D. Martin, R.G. Roberts, W.J. Stirling, Phys. Rev. D43 (1991) 3648; Phys. Lett. B266 (1991) 273.

[31] CDHSW Collaboration, J.P. Berge *et al.*, Z. Phys. C49 (1990) 187.

[32] BCDMS Collaboration, A.C. Benvenuti *et al.*, Phys. Lett. B237 (1990) 599.

[33] K. Bazizi, S.J. Wimpenny, preprint UCR/DIS/91-03 (1991).

[34] S. Mishra, talk presented at this Summer Institute.

[35] M. Virchaux, private communication.

[36] A. Ali, F. Barreiro, 'Jets in e^+e^- Annihilation and QCD' in 'High energy Electron-Positron Physics', eds. A. Ali, P. Söding, World Scientific, Singapore 1988.

[37] S. Bethke, Talk given at the Workshop on Jet Physics at LEP and HERA, Durham (UK) 1990, CERN-PPE/91-36 (1991).

[38] MARKII Collaboration , Abrams *et al.*, Nucl. Instrum. Methods A281 (1989) 55;
ALEPH Collaboration, D. Decamp *et al.*, Nucl. Instrum. Methods A294 (1990) 121;
DELPHI Collaboration, P. Aarnio *et al.*, Nucl. Instrum. Methods A303 (1991) 233;
L3 Collaboration, B. Adeva *et al.*, Nucl. Instrum. Methods A289 (1990) 35;
OPAL Collaboration, K. Ahmet *et al.*, Nucl. Instrum. Methods A305 (1991) 275.

[39] G. Kramer, B. Lampe, Z. Phys. C34 (1987) 497.

[40] R.K. Ellis, D.A. Ross, A.E. Terrano, Nucl. Phys. B 178 (1981) 321.

[41] T. Sjöstrand, Comput.Phys.Comm. 39 (1986) 347;
T. Sjöstrand, M. Bengtsson, Comput.Phys.Comm. 43 (1987) 367.

[42] N. Magnussen, DESY Internal Report F22-89-01 (1989).

[43] G. Marchesini, B. Webber, Nucl. Phys. B 310 (1988) 461.

[44] U. Petterson, Lund Preprint LU TP 88-5;
L. Lönnblad, Lund Preprint LU TP 89-10.

[45] OPAL Collaboration, M.Z. Akrawy *et al.*, Z. Phys. C47 (1990) 505.

[46] ALEPH Collaboration, D. Decamp *et al.*, Phys. Lett. B234 (1990) 209.

[47] DELPHI Collaboration, P. Aarnio *et al.*, Phys. Lett. B240 (1990) 271.

[48] W. deBoer, H. Fürstenau, J.H. Köhne, IEKP-KA/90-4.

[49] R. Marshall, Z. Phys. C43 (1989) 595.

[50] L.R. Surguladze, M.A. Samuel, Phys. Rev. Lett. 66 (1991) 560.

[51] B.A. Kniehl, J.H. Kühn, Phys. Lett. B224 (1989) 229; A. Djouadi, J.H. Kühn, P.M.Zerwas, Z. Phys. C46 (1990) 547.

[52] T. Hebbeker, 'QCD corrections to Γ_{had}', PITHA 91/08 (1991);
'QCD at LEP/SLC', lectures given at 29th Int. Meeting on fundamental physics, Sant Feliu de Guixols (Spain), PITHA 91/11 (1991).

[53] F.A. Berends, G. Burgers, W.L. van Neerven, Nucl. Phys. B 297 (1988) 429.

[54] T. Hebbeker, Talk presented at Int.Lepton-Photon Symp. Geneva 1991, PITHA 91/17 (1991).

[55] G. Grunberg, Phys. Lett. B95 (1980) 70; Phys. Rev. D28 (1983) 228.

[56] P.M. Stevenson, Nucl. Phys. B 150 (1979) 357; Phys. Rev. D23 (1981) 2916; Nucl. Phys. B 203 (1982) 472; Nucl. Phys. B 231 (1984) 65.

[57] S.J. Brodsky, G.P. Lepage, P.B. Mackencie, Phys. Rev. D28 (1983) 228.

[58] G. Kramer, Nucl. Phys. B 16 (Proc. Suppl.) (1990) 254.

[59] W.J. Stirling, talk presented at Int. Europhysics Conf. on HEP, Madrid, Spain (1989), p.124.

[60] JADE Collaboration, W. Bartel *et al.*, Z. Phys. C33 (1986) 23; JADE Collaboration, S. Bethke *et al.*, Phys. Lett. B213 (1988) 235.

[61] OPAL Collaboration, M.Z. Akrawy *et al.*, Z. Phys. C49 (1991) 375.

[62] L3 Collaboration, B. Adeva *et al.*, Phys. Lett. B248 (1990) 464.

[63] MARKII Collaboration S. Komamiya *et al.*, Phys. Rev. Lett. 64 (1990) 387.

[64] OPAL Collaboration, M.Z. Akrawy *et al.*, Phys. Lett. B235 (1990) 389.

[65] OPAL Collaboration, M.Z. Akrawy *et al.*, Z. Phys. C49 (1991) 375.

[66] ALEPH Collaboration, D. Decamp *et al.*, Phys. Lett. B255 (1991) 623.

[67] C.L. Basham *et al.*, Phys. Rev. Lett. 41 (1978) 1585; Phys. Rev. D17 (1978) 2298.

[68] OPAL Collaboration, M.Z. Akrawy *et al.*, Phys. Lett. B252 (1990) 159.

[69] L3 Collaboration, B. Adeva *et al.*, Phys. Lett. B257 (1991) 469.

[70] A. Ali, F. Barreiro, Phys. Lett. B118 (1982) 155; Nucl. Phys. B 236 (1984) 269;
D.G. Richards, W.J. Stirling, S.D. Ellis, Phys. Lett. B119 (1982) 193; Nucl. Phys. B 229 (1983) 317;
N.K. Falck, G. Kramer, Z. Phys. C42 (1989) 459.

[71] ALEPH Collaboration, D. Decamp *et al.*, Phys. Lett. B257 (1990) 479.

[72] Program supplied by P. Nason.

[73] G. Kramer, B. Lampe, Fortschr. Phys. 37 (1989) 161; Z. Phys. C39 (1989) 101.

[74] M.A. Chmeissani (MARKII Collaboration), 'Determination of α_s using EEC and Jet-mass difference at Mark2/SLC, Ph.D.Thesis, Michigan (1991).

[75] N. Magnoli, P. Nason, R. Rattazi, Phys. Lett. B252 (1990) 271.

[76] E. Laermann, K.H. Streng, P.M. Zerwas, Z. Phys. C3 (1980) 289.

[77] J. Ellis, I. Karliner, Nucl. Phys. B 148 (1979) 141;
J. Ellis, I. Karliner, W.J. Stirling, Phys. Lett. B217 (1989) 363.

[78] L3 Collaboration, B. Adeva *et al.*, Phys. Lett. B263 (1991) 551.

[79] S. Bethke, A. Ricker, P.M. Zerwas, Z. Phys. C49 (1991) 59.

[80] P.M. Zerwas, Lectures given 18th Meeting on Fundamental Physics, Lekeitio (Viscaya), Spain 1989, PITHA 89/23 (1989), and references therein.

[81] K. Koller, K.H. Streng, T.F. Walsh, P.M. Zerwas, Nucl. Phys. B 206 (1982) 225.

[82] J.G. Körner, G. Schierholz, J. Willrodt, Nucl. Phys. B 185 (1981) 365;
O. Nachtmann, A. Reiter, Z. Phys. C16 (1982) 45;
M. Bengtsson, P.M. Zerwas, Phys. Lett. B208 (1988) 306.

[83] AMY Collaboration, I.H. Park *et al.*, Phys. Rev. Lett. 62 (1989) 1713;
OPAL Collaboration, M.Z. Akrawy *et al.*, Z. Phys. C49 (1991) 49;
L3 Collaboration, B. Adeva *et al.*, Phys. Lett. B248 (1990) 227.

[84] ALEPH Collaboration, D. Decamp *et al.*, ALEPH internal note 91-84.

[85] DELPHI Collaboration, P. Abreu *et al.*, Phys. Lett. B255(1990) 466; internal note DELPHI91-52 Phys 107.

[86] D. Amati, G. Veneziano, Phys. Lett. B83 (1979) 87.

[87] Y.I. Azimov, Y.L. Dokshitzer, V.A. Khoze, S.L. Troyan, Z. Phys. C27 (1985) 65; A.H. Mueller, Nucl. Phys. B 213 (1983) 85; Nucl. Phys. B 241 (1984) 141.

[88] OPAL Collaboration, M.Z. Akrawy *et al.*, Phys. Lett. B247 (1990) 617.

[89] TASSO Collaboration, W. Braunschweig *et al.*, Z. Phys. C47 (1990) 167.

[90] L3 Collaboration, B. Adeva *et al.*, Phys. Lett. B259 (1991) 199.

[91] OPAL Collaboration, M.Z. Akrawy *et al.*,CERN-PPE/91-86 (1991).

[92] UA1 Collaboration, C. Albajar *et al.*, Z. Phys. C44 (1989) 15; Phys. Lett. B253 (1991) 503;
UA2 Collaboration, J. Alitti *et al.*, Z. Phys. C47 (1990) 11;
CDF Collaboration, F. Abe *et al.*, Phys. Rev. D44 (1991) 29.

[93] P.N. Harriman, A.D. Martin, R.G. Roberts, W.J. Stirling, Phys. Rev. D30 (1990) 798; Phys. Lett. B243 (1990) 421.

[94] WA70 Collaboration, M. Bonesini *et al.*, Z. Phys. C38 (1988) 371.

[95] E605 Collaboration, C.N. Brown *et al.*, Phys. Rev. Lett. 63 (1989) 2637.

[96] E.M. Levin, M.G. Ryskin, Phys. Rep. 189 (1990) 267.

[97] T. Sjöstrand, CERN-TH.6275/91, and references therein.

[98] B.L. Combridge, J. Kripfganz, J. Ranft, Phys. Lett. B70 (1977) 234.

[99] UA2 Collaboration, J. Alitti *et al.*, Phys. Lett. B257 (1991) 232.

[100] E. Eichten *et al.*, Rev. Mod. Phys. 56 (1984) 579; erratum Rev. Mod. Phys. 58 (1986) 1065.

[101] E. Eichten *et al.*, Phys. Rev. Lett. 50 (1983) 811.

[102] S.D. Ellis, Z. Kunszt, D.E. Soper, Phys. Rev. Lett. 64 (1990) 2121.

[103] F. Aversa *et al.*, Nucl. Phys. B 327 (1989) 105; Phys. Rev. Lett. 65 (1990) 401; Z. Phys. C46 (1990) 253.

[104] J. Patrick, invited talk given at this conference.

[105] B. Combridge, C.J. Maxwell, Nucl. Phys. B 239 (1984) 429.

[106] UA2 Collaboration, J. Alitti *et al.*, Z. Phys. C49 (1991) 17.

[107] F.A. Berends, PLB 103 (1981) 124;
R.K. Ellis, G. Marchesini, B.R. Webber, Nucl. Phys. B 286 (1987) 643.

[108] P. Aurenche *et al.*, Phys. Lett. B140 (1984) 87; NPB 297 (1988) 661.

[109] P. Aurenche, R. Baier, M. Fontannaz, Phys. Rev. D42 (1990) 1440; H. Baer, J. Ohnemus, J.F. Owen, Phys. Lett. B234 (1990) 127.

[110] UA2 Collaboration, J. Alitti *et al.*, Phys. Lett. B263 (1991) 544.

[111] CDF Collaboration, J. Huth, talk presented at Particles and Fields 1991, Vancouver, Canada, Fermilab-Conf-91/223-E.

[112] G. Altarelli, R.K. Ellis, G. Martinelli, Z. Phys. C27 (1985) 617.

[113] P.B. Arnold, M.H. Reno, Nucl. Phys. B 319 (1989) 37.

[114] R.J. Gonsalves, J. Pawlowski, C-F. Wai, Phys. Rev. D40 (1989) 2245.

[115] UA2 Collaboration, J. Alitti *et al.*, Z. Phys. C47 (1990) 523.

[116] UA2 Collaboration, J. Alitti *et al.*, Phys. Lett. B263 (1991) 563.

[117] S.D. Ellis, R. Kleiss, W.J.Stirling, Phys. Lett. B154 (1985) 435.

[118] R. Hamberg, W.L. van Neerven, T. Matsuura, DESY 90-129 (1990).

[119] G.'t Hooft, Nucl. Phys. B 61 (1973) 455.

[120] W.A. Bardeen, A.J. Buras, D.W. Duke, T. Mata, Phys. Rev. D18 (1978) 3998.

[121] A.E. Chudakov, Isv.Akad.Nauk.SSSR, Ser.Fiz. 19 (1955) 650.